VALIDATION OF PRONGHORN PRESSURE DROP CORRELATIONS AGAINST PEBBLE BED EXPERIMENTS

A Dissertation

by

JIEUN LEE

Submitted to the Graduate and Professional School of
Texas A&M University
in partial fulfillment of the requirements for the degree of

DOCTOR OF PHILOSOPHY

Chair of Committee,	Yassin A. Hassan
Committee Members,	Duy Thien Nguyen
	Victor M. Ugaz
	Rodolfo Vaghetto
Head of Department,	Michael Nastasi

May 2022

Major Subject: Nuclear Engineering

ABSTRACT

The verification and validation of Pronghorn is imperative for predicting the fluid velocity, pressure, and temperature in advanced reactors, specifically high temperature gas-cooled reactors. Pronghorn is a coarse-mesh, intermediate-fidelity, multidimensional thermal-hydraulics code developed by Idaho National Laboratory. The Pronghorn compressible/incompressible Navier-Stokes equations are validated by using the pressure drop measurements and axial velocity averaged from the particle image velocimetry data obtained at the engineering-scale pebble bed facility at Texas A&M University. Additionally, the Pronghorn energy equations with the valid correlations for the solid-fluid convective heat transfer coefficient and effective thermal conductivities predict fluid and solid temperatures well in the SANA pebble bed region.

Pronghorn and STAR-CCM+ porous media models using the Handley, KTA, and Carman correlations comparably estimate the pressure drop better than other functions with a maximum 3.34% average relative difference compared to the experimental measurements. The precise average pebble bed porosity estimation has a large impact on the pressure drop. The implementation of the volume-averaged porosity in several sectors, with each sector's thickness larger than the representative elementary length, has the potential to improve pressure drop modeling or provide more detailed velocity profiles in nuclear reactors with high aspect ratios. In addition, the pressure gradients and volume- or surface-averaged axial velocities from the realizable two-layer $k - \varepsilon$ and shear stress transport $k - \omega$ models are in good agreement with the porous media simulations and particle image velocimetry data.

The bed porosity study concludes that the MATLAB and VGSTUDIO reconstruction methods provide the average bed porosities close to the reference with less than the 1.22% relative difference. The sensitivity study of the radial porosity values verifies the 1.1% average relative difference for 75% of the original reconstructed geometries' full bed height. At a minimum, the whole bed volume within the pebble diameter length in axial direction is necessary to bring the close radial locations of local porosity oscillations. Furthermore, the new oscillatory porosity function derived

based on the Martin porosity correlation or the Hunt and Tien exponential function can be utilized for approximating the radial porosity of pebble bed experiments.

DEDICATION

This dissertation is dedicated to my parents, Joungha Lee and Gyehyeong Ahn.

ACKNOWLEDGMENTS

I would like to give special thanks to my committee chair, Dr. Yassin Hassan, for his guidance and enduring support. His instruction has helped shape various novel ideas related to the pebble bed experiments.

I also want to thank my committee members, Dr. Duy Nguyen, Dr. Rodolfo Vaghetto, and Dr. Victor Ugaz for technical support and advice. The idea about volume-averaging approach of radial porosity in porous media simulations came from Dr. Duy Nguyen, and our initial attempt contributes to the improvement of pressure drop and averaged axial velocity in pebble bed experiments.

I would like to extend my sincere thanks to researchers at Idaho National Laboratory, Dr. Paolo Balestra, Dr. Sebastian Schunert, Dr. Richard Skifton, and Dr. Minseop Song, who have provided me regular feedback and shared their expertise on porous media modeling, pebble bed reconstruction, particle image velocimetry technology, and computational fluid dynamics modeling.

CONTRIBUTORS AND FUNDING SOURCES

Contributors

This work was supported by a dissertation committee consisting of Professors Yassin Hassan and Rodolfo Vaghetto of the Department of Nuclear Engineering, Senior R&D Staff Dr. Duy Nguyen at Oak Ridge National Laboratory, and Professor Victor Ugaz of the Department of Chemical Engineering.

Dr. Robert Muyshondt and Mr. Blake Maher provided the MATLAB pebble bed reconstruction algorithms, pressure drop measurements, and the axial velocity and turbulent kinetic energy profiles obtained by the particle image velocimetry technology. In addition, the pressure drop measurements at a different pebble bed facility were given by Mr. Stephen King. All other work conducted for the dissertation was completed by the student, under the advisement of her committee members, as well as Advanced Reactor Technologies - Gas-Cooled Reactor Methods Lead Dr. Paolo Balestra, R&D Scientist Dr. Richard Skifton, and Computational Physicist Dr. Sebastian Schunert at Idaho National Laboratory.

Funding Sources

This research was partially funded by the Office of Nuclear Energy of the U.S. Department of Energy, NEAMS project, under Contract No. DE-NE0008983. This research made use of the resources of the High Performance Computing Center at Idaho National Laboratory, which is supported by the Office of Nuclear Energy of the U.S. Department of Energy and the Nuclear Science User Facilities under Contract No. DE-AC07-05ID14517. This manuscript has been authored by Battelle Energy Alliance, LLC under Contract No. DE-AC07-05ID14517 with the U.S. Department of Energy. The United States Government retains and the publisher, by accepting the article for publication, acknowledges that the U.S. Government retains a nonexclusive, paid-up, irrevocable, world-wide license to publish or reproduce the published form of this manuscript, or allow others to do so, for U.S. Government purposes.

NOMENCLATURE

General

AVR	Arbeitsgemeinschaft versuchsreaktor (Germany)
BC	Boundary condition
Bi	Biot number
CAD	Computer-aided design
CDF	Cumulative distribution function
CFD	Computational fluid dynamics
CFL	Courant-Friedrichs-Lewy
Ec	Eckert number
Eu	Euler number
FE, FEM	Finite element, finite element method
FS	Factor of safety
FV, FVM	Finite volume, finite volume method
Fr	Froude number
GCI	Grid convergence index
Gr	Grashof number
HTGR	High temperature gas-cooled reactor
HTR-PM	High temperature gas-cooled reactor pebble bed module
HTR-10	High temperature gas-cooled reactor 10 (China)
INL	Idaho National Laboratory
LHS	Latin hypercube sampling
LOFC	Loss of forced circulation

MIR	Matched index of refraction
MOOSE	Multiphysics Object-Oriented Simulation Environment
Nu	Nusselt number
PBMR	Pebble bed modular reactor
PBR	Pebble bed reactor
PDF	Probability density function
PISO	Pressure-implicit with splitting of operators
PIV	Particle image velocimetry
Pe	Peclet number
Pr	Prandtl number
RE	Richardson extrapolation
REV	Representative elementary volume
RIMS	Refractive index matched scanning
RMSE	Root mean square error
RMSRE	Root mean square relative error
ROI	Region of interest
RRMSE	Relative root mean square error
Re	Reynolds number
Ri	Richardson number
SD	Standard deviation
SEM	Standard error of the mean
SST	Shear stress transport
SUPG-CFEM	Streamline upwind Petrov-Galerkin continuous finite element method
St	Strouhal number or Stanton number

TAMU	Texas A&M University
TH	Thermal-hydraulics
THTR	Thorium hochtemperatur reaktor (Germany)
TRISO	Tri-structural isotropic particle fuel
TR-PIV	Time-resolved particle image velocimetry
V&V	Verification and validation

Mathematical Symbols

$C_{p,f}$, $C_{p,s}$	Fluid isobaric specific heat, solid isobaric specific heat [J/(kg·K)]
d	Distance from the wall [m]
d_p	Pebble diameter [m]
D	Bed diameter [m]
D_h	Hydraulic diameter [m]
E_f	Fluid total energy per unit mass [J/kg]
E_s	Young's modulus [Pa]
$f^{'}$	Characteristic frequency [-]
F_s	Safety factor [-]
g	Gravitational acceleration vector [m/s^2]
g_y	Gravitational acceleration in the y direction [m/s^2]
h	Mesh size or specific bed length cut for the porosity study [m]
H	Total length of the porous medium [m]
H_f	Fluid total enthalpy per unit mass [J/kg]
$H(y)$	Height, where spheres rest in the y direction [m]
I	Turbulence intensity [-]

k	Turbulent kinetic energy [m^2/s^2] or k-dimensional space [-]
k_f, k_s	Fluid thermal conductivity, solid thermal conductivity [W/(m·K)]
K	Permeability [m^2]
l	Turbulent length scale [m]
l_ε	Wolfstein length scale, where ε is the turbulent dissipation rate [m]
L	Characteristic length scale [m]
n	Refractive index [-]
N	Total number of cells or number of measurements [-]
N_A	Number of spheres per unit area [-]
N_L	Number of spheres per unit length [-]
p	Order of accuracy or norm [-]
$\bar{p}$	Formal order of accuracy [-]
$\hat{p}$	Observed order of accuracy [-]
P	Pressure [Pa]
$\overline{P}$	Time-averaged pressure [Pa]
q_f''', q_s''', q_t'''	Fluid volumetric heat source, solid volumetric heat source, total volumetric heat source [W/m^3]
r	Refinement ratio [-], radial distance from the center of the pebble bed [m], or fit point distance [mm]
Re_d	Wall-distance Reynolds number, $\sqrt{k}d/\nu$ [-]
Re_h	Reynolds number based on hydraulic diameter, $\rho_f u D/\mu$ for free flow region, where ε = 1, or $2\rho_f u d_p \varepsilon/(3(1-\varepsilon)\mu)$ for porous bed [-]
Re_p	Particle Reynolds number, $\rho_f u_s d_p/\mu$ [-]
Re^*	Modified Reynolds number, $Re_p/(1-\varepsilon)$ [-]

S_F	Geometric packing factor [-]
S_{ij}	Mean strain-rate tensor, where i and j are the indices of vectors [1/s]
t	Time [s] or t-value [-]
T_b	Bulk temperature [K]
T_f, T_s	Fluid temperature, solid temperature [K]
T_{suf}	Surface temperature [K]
ΔT	Difference between the hot wall and reference temperatures, $T_{suf} - T_b$ [K]
u	Interstitial/physical velocity [m/s]
$\overline{u}$	Time-averaged velocity vector [m/s]
u_{ave}	Volume- or surface-averaged velocity [m/s]
u_s	Superficial velocity, εu [m/s]
u_τ	Friction velocity, $\sqrt{\tau_w/\rho_f}$ [m/s]
$u^{'}$	Fluctuating velocity [m/s]
$\overline{u_i^{'}u_j^{'}}$	Reynolds stress tensor, where i and j are the indices of vectors [m^2/s^2]
U	Characteristic velocity [m/s]
$V_{spheres}$	Total volume of spheres [m^3]
V_{total}	Total volume of the cylinder [m^3]
ΔV_i	Volume of the i-th cell [m^3]
W	Interphase friction factor [1/s]
W_{ij}	Mean rotation tensor, where i and j are the indices of vectors [1/s]
x	Coordinate vector [m]
Δx	Interval length between the cylindrical layers for porosity study [m]

α	Solid-fluid convective heat transfer coefficient [W/(m^3·K)]
β	Thermal expansion coefficient [1/K]
δ_{ij}	Kronecker delta, where i and j are the indices of vectors [-]
ε	Porosity [-] or turbulent dissipation rate [m^2/s^3]
$\bar{\varepsilon}$	Average bed porosity [-]
ε_{ijk}	Permutation tensor, where i, j, and k are the indices of vectors [-]
ε_{min}	Minimum porosity [-]
ε_r	Solid emissivity [-]
ε_∞	Average bed porosity at infinite column diameter [-]
κ_f, κ_s	Effective fluid thermal conductivity, Effective solid thermal conductivity [W/(m·K)]
μ	Dynamic viscosity [Pa·s]
μ_t	Turbulent eddy viscosity [Pa·s]
ν	Kinematic viscosity [m^2/s]
ν_p	Poisson's ratio [-]
ν_t	Turbulent kinematic viscosity, μ_t/ρ_f [m^2/s]
ρ_f, ρ_s	Fluid density, solid density [kg/m^3]
σ'	Stefan-Boltzmann constant [W/(m^2·K^4)]
τ	Tortuosity [-]
τ_w	Wall shear stress [Pa]
ω	Specific turbulent dissipation rate [1/s]
ω_k	Angular velocity [1/s]

TABLE OF CONTENTS

Page

LIST OF FIGURES

FIGURE Page

LIST OF TABLES

TABLE Page

1. INTRODUCTION

The verification and validation (V&V) of Pronghorn is critical for predicting the fluid velocity, pressure, and temperature in advanced reactors, specifically high temperature gas-cooled reactors (HTGRs). The HTGR is an advanced Generation IV reactor concept and offers advantages over commercial nuclear power reactors. Using the direct Brayton gas-turbine cycle, the high operating temperature allows for a thermal efficiency of about 40% to 50%, which is higher than typical light water reactors' efficiency of $\sim$30% [1–3]. HTGRs produce process heat for industrial applications, such as hydrogen production, along with electricity generation [1, 4]. They also bring inherent safety features, such as passive decay heat removal, and tri-structural isotropic (TRISO) particle fuels retain radioactive fission products inside the silicon carbide layer well [5, 6]. Lastly, the primary coolant of helium gas has a comparably high thermal conductivity and is inert to avoid undesirable reactions, such as nuclear fuel degradation [1]. Therefore, it is imperative to improve and benchmark Pronghorn for pebble bed reactor (PBR) analysis, not only during a loss of forced convection (both pressurized and depressurized) in the pebble bed and upper plenum but also during reactor operation.

Although the studies related to correlations (of porosity, pressure drop, effective thermal conductivities, and solid-fluid convective heat transfer coefficient) for porous beds have been performed in different engineering applications [7–10], the validation of correlations applicable for pebble bed experiments (furthermore, HTGRs) in Pronghorn is necessary. Given that the preliminary results [11] show an excellent agreement of Pronghorn porous media flow models with STAR-CCM+ for the fluid and solid temperatures in the SANA pebble bed experiments, the initial validation of the porosity and pressure drop correlations applicable for HTGRs in the Pronghorn porous media models is achieved in [12]. The experimental average bed porosity is calculated in lieu of applying the porosity correlations, and the porosity study from [13] is used for volume-averaging the oscillatory porosity in different sectors. The MATLAB and VGSTUDIO reconstructed geometries from [13] are also utilized to develop the explicit meshes for turbulence modeling.

Several pressure drop correlations implemented in Pronghorn are validated with Texas A&M University (TAMU) isothermal pressure drop measurements, and the Pronghorn simulation results are verified by STAR-CCM+. The studies related to the interaction of the near-wall and bulk flows in the PBRs are performed by considering the bed diameter in the pressure drop functions or volume-averaging the radial porosity in the annular cylinders, including the solid cylinder in the middle of the porous bed, with the formation of the Navier-Stokes/Darcy-Forchheimer model. Moreover, the 3D pebble bed meshes are used for the realizable two-layer $k - \varepsilon$ and shear stress transport (SST) $k - \omega$ models. The corresponding pressure drop and volume- or surface-averaged axial velocities are compared with the values from the Pronghorn porous media simulations and the particle image velocimetry (PIV) data.

2. LITERATURE REVIEW & THEORY*

2.1 Porous Media Modeling

The macro-scale modeling approach is established to predict the mass, momentum, and heat transfer phenomena in porous media [14]. Macro-scale variables are defined in the representative elementary volume (REV). The model is valid when the length scale of the REV is less than the characteristic length of the flow domain and greater than the pore-scale lengths [15]. The REV is the smallest sample volume, which simulations or experiments can provide the results indicative of the macroscopic property by homogenizing the micro-heterogeneity [16]. The continuum concept is applied by taking an average of properties within the REV [15]. Figure 2.1 describes the change of porosity (the property of interest) which depends on the sample volume size. For instance, when the medium is inhomogeneous and the porosity varies in space, the numerical simulations or experiments would represent the macroscopic properties by averaging them within the REV. However, the model still requires knowledge of the closures for estimating the effective properties based on the pore-scale characteristics.

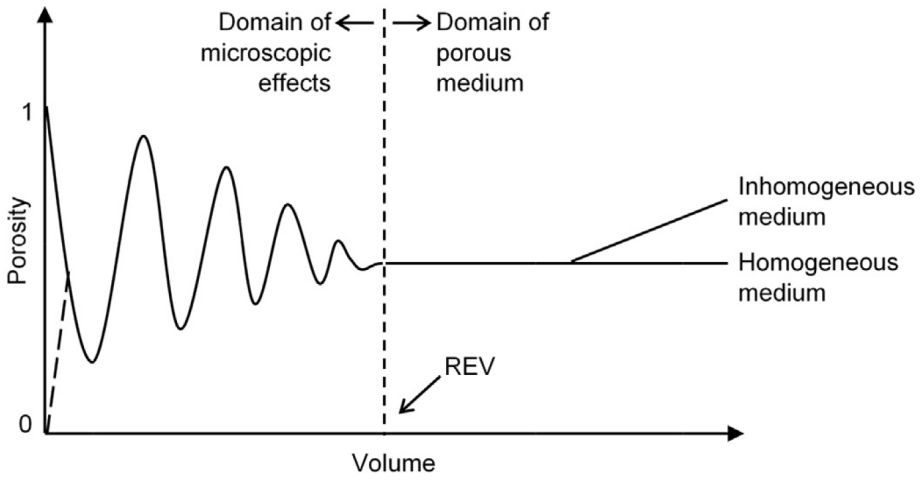

Figure 2.1. Porosity change depending on sample volume size. Reprinted from [15, 16].

*Parts of this chapter are adapted with permission from [11, 12].

Pronghorn uses the Darcy-Forchheimer model with the Navier-Stokes equations at the continuum scale [17]. The Darcy's law is applicable when the flow velocity has a linear relationship with the pressure gradient. In the low Re range, inertial forces are negligible in porous media. For the high Re fluid flows, the non-linear effect of the superficial velocity is expected. In the strong inertia regime, the inertial effect is estimated by a quadratic term of the superficial velocity [14]. Takhanov discusses that the pressure loss in the non-Darcy regime can be properly described by the Forchheimer equation [17], and it is also supported by Zimmerman [18]. Generally, the quadratic term in the Forchheimer model is derived from inertial effects in the laminar regime. Takhanov and Zimmerman conclude that the Forchheimer equation can adequately predict the pressure drop over the entire range of Reynolds number.

2.2 Pronghorn

Pronghorn is a coarse-mesh, intermediate-fidelity, multidimensional thermal-hydraulics (TH) code developed by Idaho National Laboratory (INL) [10, 19, 20]. It allows the modeling of multidimensional phenomena at higher fidelity than system analysis tools. It also reduces the computational cost by homogenizing small-scale features relative to conventional computational fluid dynamics (CFD) codes. Figure 2.2 shows the hierarchy of TH modeling and its characteristics. Pronghorn is flexible in coupling INL Multiphysics Object-Oriented Simulation Environment (MOOSE) based simulation tools, such as RELAP-7 for the system safety analysis, BISON for the fuel performance, and Griffin for the neutronics applications. Furthermore, the built-in equations of state in MOOSE can be used for determining the material properties of various compressible/incompressible fluids.

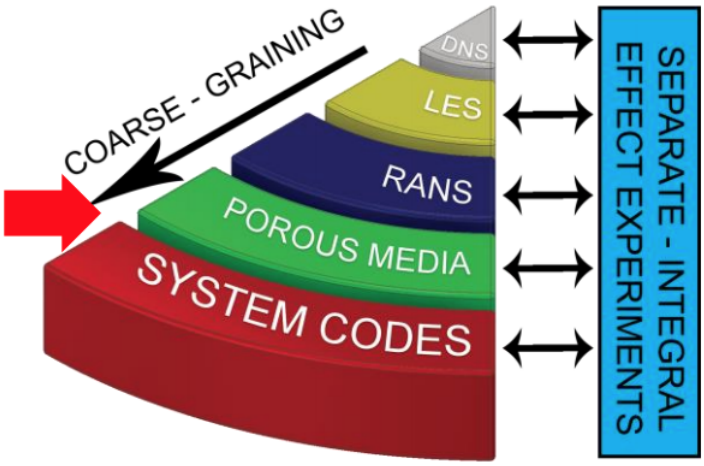

Figure 2.2. Hierarchy of TH modeling. Reprinted from [19].

2.3 Governing Equations for Porous Media Simulations

Modern Pronghorn utilizes the fully compressible Euler equations, which account for the conservation of fluid mass, momentum, energy, and solid energy [10,21]. The fluid continuity equation is given by:

$$\varepsilon \frac{\partial \rho_f}{\partial t} + \nabla \cdot (\varepsilon \rho_f u) = 0. \tag{2.1}$$

The conservation of momentum equation for fluid is:

$$\varepsilon \frac{\partial (\rho_f u)}{\partial t} + \nabla \cdot (\varepsilon \rho_f u u) + \varepsilon \nabla P - \varepsilon \rho_f g + W \rho_f u = 0. \tag{2.2}$$

The compressible Navier-Stokes model is formulated by adding the viscous force term to Equation 2.2 as:

$$\varepsilon \frac{\partial (\rho_f u)}{\partial t} + \nabla \cdot (\varepsilon \rho_f u u) + \varepsilon \nabla P - \varepsilon \rho_f g + W \rho_f u - \nabla \cdot (\varepsilon \mu \nabla u) = 0. \tag{2.3}$$

The fluid energy conservation equation is:

$$\varepsilon\frac{\partial(\rho_f E_f)}{\partial t} + \nabla\cdot(\varepsilon H_f\rho_f u) - \varepsilon\rho_f g\cdot u - \nabla\cdot(\kappa_f\nabla T_f) \\ +\alpha(T_f - T_s) - q_f^{'''} = 0, \text{ and} \tag{2.4}$$

the solid energy conservation equation is described as:

$$(1-\varepsilon)\rho_s C_{p,s}\frac{\partial T_s}{\partial t} - \nabla\cdot(\kappa_s\nabla T_s) + \alpha(T_s - T_f) - q_s^{'''} = 0. \tag{2.5}$$

Legacy Pronghorn uses a pseudo-steady momentum equation derived from Equation 2.2 by removing the unsteady and advection terms [21]. By substituting this derived equation into Equation 2.1, a pressure Poisson equation for mass conservation is shown as:

$$\varepsilon\frac{\partial\rho_f}{\partial t} + \nabla\cdot\left[\frac{\varepsilon^2}{W}(-\nabla P + \rho_f g)\right] = 0, \text{ and} \tag{2.6}$$

its fluid energy conservation is described by:

$$\varepsilon\rho_f C_{p,f}\frac{\partial T_f}{\partial t} + \varepsilon\rho_f C_{p,f} u\cdot\nabla T_f - \nabla\cdot(\kappa_f\nabla T_f) + \alpha(T_f - T_s) - q_f^{'''} = 0. \tag{2.7}$$

Specifically for the SANA experiments, the thermal non-equilibrium porous media model from the third-party CFD software, STAR-CCM+, is modified to use the formulation identical to the Pronghorn compressible Euler equations. Both legacy and modern Pronghorn equations are validated with the SANA experiments. Pronghorn compressible/incompressible Navier-Stokes equations are also verified by STAR-CCM+ thermal equilibrium porous media simulations and validated with the TAMU isothermal pressure drop measurements and PIV data.

2.4 Equations of State & Material Properties

The nitrogen dynamic viscosity and its thermal conductivity are calculated as functions of temperature and density based on [22]. The specific heat and molecular weight of nitrogen gas are obtained from [23]. The ideal gas law is used to correlate fluid density, temperature, and pressure. The electric graphite density, thermal conductivity, and isobaric specific heat from [24–26] are used for the pebble properties.

The TAMU isothermal pebble bed experiments are designed by having water, air, or p-Cymene going through the porous bed. The constant density model is applied in both Pronghorn and STAR-CCM+ for incompressible fluids, such as p-Cymene and water, while the ideal gas law is applied to determine the air density. The water and air properties are obtained from [27–29], and p-Cymene fluid properties are from [30].

For constructing the heated pebble bed experiments, which bring the similar fluid behavior and heat transfer of the prototype reactor, the initial scaling analysis is accomplished in Section 5.4. The equations of state for helium from [31] can be used for defining the fluid properties at the scaled-down high temperature gas-cooled reactor pebble bed module (HTR-PM) experimental facility. Acrylic spheres may be used in lieu of matrix graphite pebbles, and the physical properties of acrylic and matrix graphite are described in [10, 25, 32–36]. The matrix graphite properties used in the HTR-PM prototype reactor are obtained at the mean value of the primary coolant inlet and outlet temperatures. However, the current operating temperature range obtained by the scaling study exceeds the melting point of acrylic. Therefore, further studies related to finding compatible fluid and solid materials at the feasible operating temperature range would be necessary.

2.5 Porosity Correlations

The average bed porosity, $\bar{\varepsilon}$, of a randomly packed bed of pebbles is determined by dividing the fluid volume by the total volume of the porous bed. This value is calculated by hand and 3D pebble bed reconstructions using MATLAB algorithms and VGSTUDIO. These methods are more accurate in place of using the porosity functions derived by other researchers. Nevertheless, several average bed porosity correlations in Table 2.1 are studied for the validation purposes. The validity condition of the average bed porosity function is the specific range of aspect ratio, D/d_p. Table 2.1 also contains the experimental setups, such as the bed diameter, pebble diameter, materials, and the packing method, applied for determining correlations. The standard deviation (SD) of the average bed porosity is estimated by the error propagation, or the most conservative SD is chosen from the literature. The root mean square error (RMSE), absolute difference, or relative difference is obtained between the experiments and some correlations while other literature discuss the standard

error of the mean (SEM) of correlation rather than the SD. Lastly, Cheng uses several experiments performed by different authors to develop the average bed porosity function in Table 2.2.

The radial porosity profiles obtained from MATLAB and VGSTUDIO reconstructed geometries are compared with the oscillatory/exponential radial porosity correlations in Table 2.3 and Table 2.4, and consequently, the new oscillatory porosity function is developed in Equation 5.1. Table 2.5 contains the experimental data on which the correlations are developed based. Not all the particle shapes or materials used in the experiments are included, however, those similar to the TAMU pebble bed experiments' are listed in Table 2.5.

The average bed porosity functions in Table 2.1 are often used in porous media simulations to determine the macro-scale effects, such as pressure drop, whereas the functions in Table 2.3 and Table 2.4 show more details of radial porosity. The oscillatory/exponential porosity correlations provide the micro-heterogeneous information inside the REV. Therefore, the new oscillatory porosity function is applied directly and also after volume-averaging it in different numbers of sectors for comparing pressure drop and averaged axial velocities.

Table 2.1. Average bed porosity correlations.

Author	Validity condition	Correlation	Bed diameter (mm)	Pebble diameter (mm)	Material for spheres/ packing method	Material for the column
Mueller [37]	$\frac{D}{d_p} \geq 2.02$	$0.365 + 0.22\frac{d_p}{D} \pm 0.0055/D$ (SD propagated)	25.75, 50.50, 76.00, 101.88	12.751	Clear Lucite plexiglass/ random packing	Clear cast acrylic cylindrical container
Sato et al. [38]	$\frac{d_p}{D} < 0.4$	$0.3517 + 0.4657\frac{d_p}{D}$ ± 0.0076 (Max. SD of measurements)	65.8, 122	2.59, 12.2, 24.3	Glass spheres/ gently dumped	Acrylic tubes
Aerov [39]	$D/d_p > 10$	$0.39 + 0.07\frac{d_p}{D} + 0.54\left(\frac{d_p}{D}\right)^2$	← Inaccessible →			
Dixon [40]	$\frac{d_p}{D} \leq 0.5$	$0.4 + 0.05\frac{d_p}{D} + 0.412\left(\frac{d_p}{D}\right)^2$ ± 0.02 (Absolute difference)	15.875 $\sim$ 76.2	Different sizes of spheres $\left(0.1 \leq \frac{d_p}{D} \leq 1\right)$	-/fairly slow pouring of spheres by hand	-
de Klerk† [41]	$\frac{D}{d_p} > 2$	$\varepsilon_\infty + 0.35e^{-0.39\frac{D}{d_p}}$ $\pm 2\%$ (Relative difference)	4.9 $\sim$ 57.5	3	Glass beads/ pouring of beads with some tapping of the wall	Glass columns
Beavers et al. [42]	$15 < \frac{D}{d_p} < 45$	$0.368\left(1 + 2\frac{d_p}{D}\left(\frac{0.476}{0.368} - 1\right)\right)$ $\pm 2\%$ of $\bar{\varepsilon}$ (Max. SD of measurements)	Rectangular bed (Width = 114.3, length = 298.5)	3, 6, 14.3	Glass spheres/pouring a layer of spheres into the duct and then shaking	Aluminum & clear plexiglass

†The average bed porosity function is also validated with other experiments. More details are included in [41].

Table 2.1. Continued.

Author		Validity condition	Correlation	Bed diameter (mm)	Pebble diameter (mm)	Material for spheres/ packing method	Material for the column
Foumeny et al. [43]		$1+\frac{\sqrt{3}}{2} < \frac{D}{d_p}$	$0.383 + 0.25\,(D/d_p)^{-0.923}\,\frac{1}{\sqrt{0.723\frac{D}{d_p}-1}}$ 1.4% (RMSE)	50	$3 < \frac{D}{d_p} < 25$, d_p not specified separately	-/gentle vibration for packing spherical particles	Perspex tube
Fand and Thinakaran [44]		$\frac{D}{d_p} \geq 2.033$	$\frac{0.151}{\left(\frac{D}{d_p}-1\right)} + 0.36$ ±2.4% (Relative difference)	5.588 $\sim$ 86.6	2.067 $\sim$ 4.029	Glass spheres/ randomly dropping small batches of dry spheres	Stainless water tunnel
Zou and Yu [45]	Loose packing	$\frac{d_p}{D} \leq 0.256$	$0.4 + 0.01\left(e^{10.686\frac{d_p}{D}} - 1\right)$	35, 54, 62, 74, 90, 104, 127, 172, and 194	1, 2, ..., 12 (Glass beads) 15.8, 25.8, and 37.0 (Marble balls)	Glass beads and marble balls/ random packing	-
	Dense packing	$\frac{d_p}{D} \leq 0.253$	$0.372{+}0.002\left(e^{15.306\frac{d_p}{D}} - 1\right)$				
Jeschar [46]		$\frac{d_p}{D} \leq 0.16$	$0.375 + 0.34\frac{d_p}{D}$	508	10, 20, 30, and 80	Glass, stoneware balls/ random packing	Rubble column
Benyahia and O'Neill [47]		$1.5 \leq \frac{D}{d_p} \leq 50$	$0.39 + \frac{1.740}{(D/d_p{+}1.140)^2}$ ±0.015 (SEM)	-	$2 \sim 10$	-/gently pouring particles with gentle tapping	-

Table 2.1. Continued.

Author	Validity condition	Correlation
Cheng [48]	$1.1 < \frac{D}{d_p} < 50.5$	$\left(\left(0.8\left(\frac{D-d_p}{d_p}\right)^{0.27}\right)^{-3} + \left(0.38\left[1+\left(\frac{d_p}{D-d_p}\right)^{1.9}\right]\right)^{-3}\right)^{-1/3}$ ± 0.00039 from Fand and Thinakaran [44], ± 0.00103 from Fand et al. [49], ± 0.00097 from Raichura [50], or ± 0.00287 from Montillet et al. [51] (SEM for Fand and SD for others)

Table 2.2. Experimental setups for the average bed porosity function developed by Cheng.

Author	Bed diameter (mm)	Pebble diameter (mm)	Material for spheres/ packing method	Material for the column
Reichelt [52]	41.5, 79.8, 139	9.71, 14.9	Glass balls/ random packing	-
Fand et al.† [49]	5.588, 6.4516, 7.0104	3.994, 4.9997, 5.9901	Glass spheres/ randomly dropping small batches of dry spheres	Stainless steel circular cylinder
Raichura [50]	51	$3 \sim 10$	Near-spherical glass beads/ dropping a few pebbles at a time (Closest packing in every layer)	Stainless steel tube
Montillet et al. [51]	$22.23 \sim 99.905$	$5.82 \sim 9.95$	Glass particles/ random packing	-
Calis et al. [53]	$12.7 \sim 26$ (Length of the square)	9.5, 12.7	High-precision polyethylene spheres	Polymethyl methacrylate square channel
Cheng [54]	16.4 (Length of the square)	16	Glass beads/ close random packing	Square steel pipe

†Including the experiments from [49], Cheng uses other experiments from Fand and Thinakaran [44], and they are described in Table 2.1.

Table 2.3. Radial oscillatory porosity correlations.

Author	Validity condition	Correlation
Cohen and Metzner [55]	$7 \leq \frac{D}{d_p} \leq 60$	$\begin{cases} 4.5(\varepsilon_\infty - 1)\left[\frac{d}{d_p} - \frac{7}{9}\left(\frac{d}{d_p}\right)^2\right] + 1 & \text{if } \frac{d}{d_p} \leq 0.25 \\ 0.3463(1-\varepsilon_\infty)e^{\left(-0.4273\frac{d}{d_p}\right)} cos\left(2.4509\frac{d}{d_p} - 2.2011\right)\pi + \varepsilon_\infty & \text{if } 0.25 < \frac{d}{d_p} < 8 \\ \varepsilon_\infty & \text{if } \frac{d}{d_p} \geq 8 \end{cases}$ $\pm 0.5\%$ (Ave. relative difference)
de Klerk [41]	$\frac{D}{d_p} > 2$	$\begin{cases} 2.14\left(\frac{d}{d_p}\right)^2 - 2.53\frac{d}{d_p} + 1 & \text{if } \frac{d}{d_p} \leq 0.637 \\ \varepsilon_\infty + 0.29e^{-0.6\frac{d}{d_p}} cos\left[2.3\pi\left(\frac{d}{d_p} - 0.16\right)\right] + 0.15e^{-0.9\frac{d}{d_p}} & \text{if } \frac{d}{d_p} > 0.637 \end{cases}$ $\pm 11\%$ (Relative difference)
Martin [56, 57]	$\frac{D}{d_p} = \infty$, $\frac{D}{d_p} = 20.3$	$\begin{cases} \varepsilon_{min} + (1-\varepsilon_{min})\left(\frac{2d}{d_p} - 1\right)^2 & \text{if } -1 \leq \frac{2d}{d_p} - 1 \leq 0 \\ \varepsilon_\infty + (\varepsilon_{min} - \varepsilon_\infty) exp\left[-\frac{1}{4}\left(\frac{2d}{d_p} - 1\right)\right] cos\left[\frac{\pi}{C}\left(\frac{2d}{d_p} - 1\right)\right] & \text{if } \frac{2d}{d_p} - 1 > 0 \end{cases}$ $\varepsilon_{min} = 0.23$ or 0.245 [58] $C = \begin{cases} 0.816 & \text{for } \frac{D}{d_p} = \infty \\ 0.876 & \text{for } \frac{D}{d_p} = 20.3 \end{cases}$

Table 2.4. Radial exponential porosity correlations.

Author	Validity condition	Correlation
Vortmeyer and Schuster [59]	$\frac{D}{d_p} \geq 2.61$ from Benenati and Brosilow [60]	$\varepsilon_\infty \left[1 + \frac{1-\varepsilon_\infty}{\varepsilon_\infty exp(1)} \cdot exp\left(1 - 2\frac{d}{d_p}\right)\right]$
Cheng and Hsu [61]	$5.99 \leq \frac{D}{d_p} \leq 47.61$ from Yagi and Kunii [62]	$\varepsilon_\infty \left[1 + exp\left(-2\frac{d}{d_p}\right)\right]$
Hunt and Tien [58, 63]	$\frac{D}{d_p} = 11.14, 12.8$ from Valstar et al. [64]	$\varepsilon_\infty \left[1 + \left(\frac{1}{\varepsilon_\infty} - 1\right) exp\left(-6\frac{d}{d_p}\right)\right]$
White and Tien [65]	$\frac{D}{d_p} = 8.82, 13.7$ for spheres, $\frac{D}{d_p} = 6.7, 13.4$ for Berl saddles from Roblee et al. [66]	$\left(1 + \left[\frac{1-\varepsilon_\infty}{\varepsilon_\infty}\right] \cdot \left(1 - e^{-2\frac{d}{d_p}}\right)^{1/2}\right)^{-1}$ More applicable to irregular particles, such as Berl saddles

Table 2.5. Experimental setups for radial porosity correlations.

Author	Bed diameter (mm)	Pebble diameter (mm)	Material for spheres/ packing method	Material for the column	Correlation
Roblee et al. [66]	170.18	12.446, 19.304	Spheres made of composition cork/ random packing	Cardboard cylinder	Cohen and Metzner, de Klerk, White and Tien
Benenati and Brosilow [60]	41.25	2.032 $\sim$ 15.799	Spherical lead shots/ random packing	-	Cohen and Metzner, de Klerk, Martin, Vortmeyer and Schuster† (d_p = 4 mm), White and Tien
Ridgway and Tarbuck [67]	152.4	8, 9, 10, 12, and 20	Polythene spheres/ vibration by a motor	Horizontal cylinder of dura-lumin	de Klerk
Goodling et al. [68]	52.5 $\sim$ 101.9	3.175 $\sim$ 9.525	Polystyrene spheres/ random packing	Plastic pipe	de Klerk
Yagi and Kunii [62]	-	0.76$\sim$ 19.2	Glass beads, cement clinkers, celite balls, lead shots/ random packing	Steel	Cheng and Hsu
Valstar et al. [64]	41	3.19, 3.68	Glass and steel spheres/ random packing	Stainless steel	Hunt

†Vortmeyer and Schuster perform experiments with 4 mm glass spheres separate from Benenati and Brosilow's.

2.6 Pressure Drop Correlations

The pressure drop, ΔP, of the fluid due to pebbles in the reactor is estimated by using correlations in Table 2.6. Overall, the friction factor varies depending on the pebble diameter, porosity, and fluid properties (such as fluid density and dynamic viscosity). Some correlations use the aspect ratio, D/d_p, to consider the near-wall effects, and others use the tortuosity to introduce the transverse flow effect. Overall, the average bed porosity is utilized for quantifying the superficial velocity, modified Re, and the consequent pressure drop in porous bed. The experimental arrangements for the empirical pressure drop correlations in Table 2.7 are described in a similar manner compared to Table 2.5 except the column length, fluid material, and operating conditions are itemized additionally. Some pressure drop functions use the experiments from other literature in Table 2.8, Table 2.9, Table 2.10, and Table 2.11.

The Carman-type pressure drop correlation has the inertial resistance term inversely proportional to the modified Re raised to a certain power, and this exponent is between 0 and 0.5 for the strong entrance and/or mixing effects [69]. For instance, the exponents of 0.13, 0.1, 1/6, and 0.2 are used in the Jones and Krier [70], Carman [71], Tallmadge [72], and Hicks [73] pressure drop correlations, respectively. Liu et al. argue that generally the zero exponent is utilized when the flow is laminar, and the exponent is likely to be greater than zero for the turbulent flow. However, some other pressure drop functions still use the zero exponent for the turbulent flow regime in Table 2.6

Table 2.6. Pressure drop correlations.

Author	Correlation	Uncertainty or error	Validity condition		
			Porosity range	Aspect ratio range	Re^* or Re_p range
Ergun [74]	$\left[150\mu\frac{(1-\bar{\varepsilon})^2}{\bar{\varepsilon}^3}\frac{u_s}{d_p^2}+1.75\rho_f\frac{(1-\bar{\varepsilon})}{\bar{\varepsilon}^3}\frac{u_s^2}{d_p}\right]H$	-	$0.36<\bar{\varepsilon}<0.4$ [75,76] $0.4<\bar{\varepsilon}<0.65$ [70,77]	$\frac{D}{d_p}>10$ [9]	$1<Re^*<2,000$ [9] $1<Re^*<2,500$ [75] $0.67<Re^*<2,300$ [70,77]
Avontuur and Geldart [8,78]	$\left[141\mu\frac{(1-\bar{\varepsilon})^2}{\bar{\varepsilon}^3}\frac{u_s}{d_p^2}+1.52\rho_f\frac{(1-\bar{\varepsilon})}{\bar{\varepsilon}^3}\frac{u_s^2}{d_p}\right]H$	←	Inaccessible	→	$Re^*<10^4$
Handley [79]	$\left[368\mu\frac{(1-\bar{\varepsilon})^2}{\bar{\varepsilon}^3}\frac{u_s}{d_p^2}+1.24\rho_f\frac{(1-\bar{\varepsilon})}{\bar{\varepsilon}^3}\frac{u_s^2}{d_p}\right]H$	Standard error: $\pm\frac{229}{Re^*}$ of $f_{Handley}$†	$0.36\leq\bar{\varepsilon}\leq0.39$	$8\leq\frac{D}{d_p}\leq22$	$200<Re_p<13,000$
Özahi et al. [80]	$\left[160\mu\frac{(1-\bar{\varepsilon})^2}{\bar{\varepsilon}^3}\frac{u_s}{d_p^2}+1.61\rho_f\frac{(1-\bar{\varepsilon})}{\bar{\varepsilon}^3}\frac{u_s^2}{d_p}\right]H$	Max. relative difference: ±4% of f_{Ozahi}‡	$0.36\leq\bar{\varepsilon}\leq0.56$	$5.72\leq\frac{D}{d_p}\leq17.16$	$708.2\leq Re^*\leq7,772.73$
Foscolo et al. [81]	$\left[17.3\mu\frac{(1-\bar{\varepsilon})}{\bar{\varepsilon}^{4.8}}\frac{u_s}{d_p^2}+0.336\rho_f\frac{(1-\bar{\varepsilon})}{\bar{\varepsilon}^{4.8}}\frac{u_s^2}{d_p}\right]H$	-	$0.4\leq\bar{\varepsilon}\leq1$	-	Not provided, but the free falling Re is provided.
Leva [7]	$\left[200\mu\frac{(1-\bar{\varepsilon})^2}{\bar{\varepsilon}^3}\frac{u_s}{d_p^2}+7/4\rho_f\frac{(1-\bar{\varepsilon})}{\bar{\varepsilon}^3}\frac{u_s^2}{d_p}\right]H$	Inaccessible	$0.354\leq\bar{\varepsilon}\leq0.651$	$1.624\leq\frac{D}{d_p}\leq13.466$	$1<Re_p<17,635$
Yu et al. [82]	$\left[203\mu\frac{(1-\bar{\varepsilon})^2}{\bar{\varepsilon}^3}\frac{u_s}{d_p^2}+1.95\rho_f\frac{(1-\bar{\varepsilon})}{\bar{\varepsilon}^3}\frac{u_s^2}{d_p}\right]H$	-	$0.364\leq\bar{\varepsilon}\leq0.379$	$\frac{D}{d_p}=30$	$750\leq Re_p\leq2,500$

† $f_{Handley}=\frac{368}{Re^*}+1.24$.
‡ $f_{Ozahi}=\frac{160}{Re^*}+1.61$.

Table 2.6. Continued.

Author	Correlation	Uncertainty or error	Validity condition		
			Porosity range	Aspect ratio range	Re^* or Re_p range
Macdonald et al.† [83]	$\left[180\mu\frac{(1-\bar{\varepsilon})^2}{\bar{\varepsilon}^3}\frac{u_s}{d_p^2}+1.8\rho_f\frac{(1-\bar{\varepsilon})}{\bar{\varepsilon}^3}\frac{u_s^2}{d_p}\right]H$	Prediction band: $\pm 50\%$ of $f_{Macdonald}$‡	$0.366 \leq \bar{\varepsilon} \leq 0.64$ [84] $0.682 \leq \bar{\varepsilon} \leq 0.919$ [85] $0.367 \leq \bar{\varepsilon} \leq 0.515$ [86] $0.123 \leq \bar{\varepsilon} \leq 0.378$ [87]	-	$Re^* < 500$ [88]
Meyer and Smith [8]	$\left[90\mu\frac{(1-\bar{\varepsilon})^2}{\bar{\varepsilon}^{4.1}}\frac{u_s}{d_p^2}+0.462\rho_f\frac{(1-\bar{\varepsilon})}{\bar{\varepsilon}^{4.1}}\frac{u_s^2}{d_p}\right]H$	←	Inaccessible	→	$Re^* < 6,000$
Morcom [8]	$\left[784.8\mu\left(\frac{0.405}{\bar{\varepsilon}}\right)^3\frac{u_s}{d_p^2}+13.73\rho_f\left(\frac{0.405}{\bar{\varepsilon}}\right)^3\frac{u_s^2}{d_p}\right]H$	←	Inaccessible	→	$Re_p < 750$
Wu et al. [89]	$\left[72\mu\tau\frac{(1-\bar{\varepsilon})^2}{\bar{\varepsilon}^3}\frac{u_s}{d_p^2} +3\tau\left(\frac{3}{2}+\frac{1}{\beta'^4}-\frac{5}{2\beta'^2}\right)\rho_f\frac{(1-\bar{\varepsilon})}{4\bar{\varepsilon}^3}\frac{u_s^2}{d_p}\right]H,$ $\tau=\frac{1}{2}\left[1+\frac{1}{2}\sqrt{1-\bar{\varepsilon}} +\sqrt{1-\bar{\varepsilon}}\frac{\sqrt{\left(\frac{1}{\sqrt{1-\bar{\varepsilon}}}-1\right)^2+\frac{1}{4}}}{1-\sqrt{1-\bar{\varepsilon}}}\right]$ [90], $\beta'=\frac{1}{1-\sqrt{1-\bar{\varepsilon}}}$	-	$\bar{\varepsilon}=0.364, 0.42$	$\frac{D}{d_p}=10,30$ [82, 91]	$1,000 < Re^* < 4,000$

†Macdonald et al. use multiple experiments to develop the pressure drop function in Table 2.8. ‡$f_{Macdonald}=\frac{180}{Re^*}+1.8$.

Table 2.6. Continued.

Author	Correlation	Uncertainty or error	Validity condition		
			Porosity range	Aspect ratio range	Re^* or Re_p range
Hayes et al. [88]	$\left[\frac{1}{\tau}\left(850+\frac{11.6(3\tau-1)}{\tau(1-\bar{\varepsilon})(1-\tau)}Re_p\right)^{0.5}\mu\frac{(1-\bar{\varepsilon})^2}{\bar{\varepsilon}^4}\frac{u_s}{d_p^2}+\frac{1.3}{2}\left(\frac{\tau}{3\tau-1}\right)\rho_f\frac{(1-\bar{\varepsilon})}{\bar{\varepsilon}^3}\frac{u_s^2}{d_p}\right]H,$ $\bar{\varepsilon}=\frac{(3\tau-1)^2}{4\tau^3}$	Prediction band: $\pm 10\%$ of f_{Hayes}[†]	$0.385 \leq \bar{\varepsilon} \leq 0.427$ ($0.464 \leq \tau \leq 0.477$)	$\frac{D}{d_p} \geq 10$	$4 \leq Re_p \leq 450$
Cheng [48]	$\left[\left[185+17\frac{\bar{\varepsilon}}{1-\bar{\varepsilon}}\left(\frac{D}{D-d_p}\right)^2\right]\mu\frac{(1-\bar{\varepsilon})^2}{\bar{\varepsilon}^3}\frac{u_s}{d_p^2}+\left[1.3\left(\frac{1-\bar{\varepsilon}}{\bar{\varepsilon}}\right)^{\frac{1}{3}}+0.03\left(\frac{D}{D-d_p}\right)^2\right]\rho_f\frac{(1-\bar{\varepsilon})}{\bar{\varepsilon}^3}\frac{u_s^2}{d_p}\right]H$	-	$0.3571 \leq \bar{\varepsilon} \leq 0.6168$[‡] [44]	$1.1 \leq \frac{D}{d_p} \leq 50.5$	$0.62 \leq Re_p \leq 869$[‡] [44]
Eisfeld and Schnitzlein[§] [92]	$\left[154A_w^2\mu\frac{(1-\bar{\varepsilon})^2}{\bar{\varepsilon}^3}\frac{u_s}{d_p^2}+\frac{A_w}{B_w}\rho_f\frac{(1-\bar{\varepsilon})}{\bar{\varepsilon}^3}\frac{u_s^2}{d_p}\right]H,$ $A_w=1+\frac{2}{3(D/d_p)(1-\bar{\varepsilon})},$ $B_w=\left[1.15\left(\frac{d_p}{D}\right)^2+0.87\right]^2$	Root mean square relative error (RMSRE): $\pm 16.13\%$ of $f_{Eisfeld}$[**]	$0.33 \leq \bar{\varepsilon} \leq 0.882$	$1.624 \leq \frac{D}{d_p} \leq 250$	$0.01 \leq Re_p \leq 17,635$

[†] $f_{Hayes}=\left[\frac{1}{\tau}\left(850+\frac{11.6(3\tau-1)}{\tau(1-\bar{\varepsilon})(1-\tau)}Re_p\right)^{0.5}\frac{(1-\bar{\varepsilon})^2}{\bar{\varepsilon}^2}+\frac{1.3}{2}\left(\frac{\tau}{3\tau-1}\right)\frac{(1-\bar{\varepsilon})}{\bar{\varepsilon}}Re_p\right]\frac{\bar{\varepsilon}}{(1-\bar{\varepsilon})^2}$.

[‡] Fand and Thinakaran's porosity range and Re range are given for the Cheng pressure drop correlation.

[§] Eisfeld and Schnitzlein use the experiments in Table 2.9 to derive the pressure drop function.

[**] $f_{Eisfeld}=\frac{154A_w^2(1-\bar{\varepsilon})^2}{Re_p\bar{\varepsilon}^3}+\frac{A_w(1-\bar{\varepsilon})}{B_w\bar{\varepsilon}^3}$.

Table 2.6. Continued.

Author	Correlation	Uncertainty or error	Validity condition		
			Porosity range	Aspect ratio range	Re^* or Re_p range
Fand and Thinakaran [44]	$\left[AM^2\mu\frac{(1-\bar{\varepsilon})^2}{\bar{\varepsilon}^3}\frac{u_s}{d_p^2}+BM\rho_f\frac{(1-\bar{\varepsilon})}{\bar{\varepsilon}^3}\frac{u_s^2}{d_p}\right]H$, $A=173$ and $B=1.87$ for the Forchheimer flow, $A=214$ and $B=1.57$ for the turbulent flow, $M=1+\frac{2}{3}\frac{d_p}{D(1-\bar{\varepsilon})}$	Ave. relative difference: $\pm3.2\%$ of A and $\pm3.0\%$ of B for the Forchheimer flow, $\pm3.9\%$ of A and $\pm2.5\%$ of B for the turbulent flow	$0.3571\leq\bar{\varepsilon}\leq 0.6168$	$1.399\leq\frac{D}{d_p}\leq 41.28$	$Re_p>120$ for the turbulent flow
Mehta and Hawley [93]	$\left[150M^2\mu\frac{(1-\bar{\varepsilon})^2}{\bar{\varepsilon}^3}\frac{u_s}{d_p^2}+1.75M\rho_f\frac{(1-\bar{\varepsilon})}{\bar{\varepsilon}^3}\frac{u_s^2}{d_p}\right]H$	-	-	$7<\frac{D}{d_p}<91$	$0.18<Re^*<9.55$ [8]
Reichelt† [52]	$\left[150M^2\mu\frac{(1-\bar{\varepsilon})^2}{\bar{\varepsilon}^3}\frac{u_s}{d_p^2}+\left(\frac{1.5}{(D/d_p)^2}+0.88\right)^{-2}M\rho_f\frac{(1-\bar{\varepsilon})}{\bar{\varepsilon}^3}\frac{u_s^2}{d_p}\right]H$, $\left[150M^2\mu\frac{(1-\bar{\varepsilon})^2}{\bar{\varepsilon}^3}\frac{u_s}{d_p^2}+1.3M\rho_f\frac{(1-\bar{\varepsilon})}{\bar{\varepsilon}^3}\frac{u_s^2}{d_p}\right]H$ for spheres	-	$0.366\leq\bar{\varepsilon}\leq 0.681$	$1.7<\frac{D}{d_p}<91$, $\frac{D}{d_p}>10$ for spheres	$0.2<\frac{Re^*}{M}<30,000$
Hassan and Kang [7]	$\left[160\mu\frac{(1-\bar{\varepsilon})^2}{\bar{\varepsilon}^3}\frac{u_s}{d_p^2}+\frac{1}{0.2+3.6d_p/D}\rho_f\frac{(1-\bar{\varepsilon})}{\bar{\varepsilon}^3}\frac{u_s^2}{d_p}\right]H$	Uncertainty: $\pm5.5\%$ of f_{Hassan}‡	$\bar{\varepsilon}=0.465$	$\frac{D}{d_p}<5$ or $\frac{D}{d_p}=3.65$	$20,000<Re^*<29,936$

†Reichelt's experimental details are described in Table 2.2. ‡$f_{Hassan}=\frac{\Delta P d_p^2\bar{\varepsilon}^3}{H\mu u_s(1-\bar{\varepsilon})^2}$.

Table 2.6. Continued.

Author	Correlation	Uncertainty or error	Validity condition		
			Porosity range	Aspect ratio range	Re^* or Re_p range
O'Neill and Benyahia [8]	$\left[\left(521.26 - 22581.24\left(\frac{d_p}{D}\right)^2\right)\mu\frac{(1-\bar{\varepsilon})^2}{\bar{\varepsilon}^3}\frac{u_s}{d_p^2} + \left(1.12 + 4.2\frac{d_p}{D}\right)\rho_f\frac{(1-\bar{\varepsilon})}{\bar{\varepsilon}^3}\frac{u_s^2}{d_p}\right]H$	← Inaccessible →		$5 < \frac{D}{d_p} < 25$	-
Raichura† [50]	$\left[103\left(\frac{\bar{\varepsilon}}{1-\bar{\varepsilon}}\right)^2\left[6(1-\bar{\varepsilon}) + \frac{80d_p}{D}\right]\mu\frac{(1-\bar{\varepsilon})^2}{\bar{\varepsilon}^3}\frac{u_s}{d_p^2} + 2.8\frac{\bar{\varepsilon}}{1-\bar{\varepsilon}}\left(1 - \frac{1.82d_p}{D}\right)^2\rho_f\frac{(1-\bar{\varepsilon})}{\bar{\varepsilon}^3}\frac{u_s^2}{d_p}\right]H$	-	-	$5 < \frac{D}{d_p} < 50$	$30 < Re_p < 1,700$
Foumeny et al.‡ [43]	$\left[130\mu\frac{(1-\bar{\varepsilon})^2}{\bar{\varepsilon}^3}\frac{u_s}{d_p^2} + \frac{1}{0.335+2.28\frac{d_p}{D}}\rho_f\frac{(1-\bar{\varepsilon})}{\bar{\varepsilon}^3}\frac{u_s^2}{d_p}\right]H$	RMSE: ±0.23 of $\frac{1}{0.335+2.28\frac{d_p}{D}}$	-	$3 < \frac{D}{d_p} < 25$	$5 < Re^* < 8,500$
Paterson et al. [8]	$\left[150\left(1 + 1.22\frac{d_p}{D}\right)\mu\frac{(1-\bar{\varepsilon})^2}{\bar{\varepsilon}^3}\frac{u_s}{d_p^2} + 1.75e^{1.66\left(\left(1-\frac{d_p}{D}\right)^2-1\right)}\rho_f\frac{(1-\bar{\varepsilon})}{\bar{\varepsilon}^3}\frac{u_s^2}{d_p}\right]H$	← Inaccessible →		$3.5 < \frac{D}{d_p} < 22$	$25 < Re_p < 900$
Harrison et al.§ [94]	$\left[119.8\left(1 + \pi\frac{d_p}{6(1-\bar{\varepsilon})D}\right)^2\mu\frac{(1-\bar{\varepsilon})^2}{\bar{\varepsilon}^3}\frac{u_s}{d_p^2} + \frac{4.63}{Re^{*1/6}}\left[1 - \frac{\pi^2 d_p}{24D}\left(1 - \frac{0.5d_p}{D}\right)\right]\rho_f\frac{(1-\bar{\varepsilon})}{\bar{\varepsilon}^3}\frac{u_s^2}{d_p}\right]H$	Ave. relative difference: ±13.4% of $\Delta P/H$	$0.33 < \bar{\varepsilon} < 0.88$	$8.3 < \frac{D}{d_p} < 50$	$0.32 < Re_p < 7,700$

†Raichura's experiments are given in Table 2.2 except the packing method is changed to pouring the particles and gently shaking the cylinder.
‡Foumeny's experiments are provided in Table 2.1.
§Harrison et al. use Burke and Plummer's, Ergun and Orning's, and Wentz Jr and Thodos's experiments in Table 2.9.

Table 2.6. Continued.

Author	Correlation	Uncertainty or error	Validity condition		
			Porosity range	Aspect ratio range	Re^* or Re_p range
Liu et al. [69]	$\left[85.2\left(1+\pi\frac{d_p}{6(1-\bar{\varepsilon})D}\right)^2\mu\frac{(1-\bar{\varepsilon})^2}{\bar{\varepsilon}^{11/3}}\frac{u_s}{d_p^2} + \frac{0.69Re_m^3}{16^2+Re_m^2}\left[1-\frac{\pi^2 d_p}{24D}\left(1-\frac{0.5d_p}{D}\right)\right]\mu\frac{(1-\bar{\varepsilon})^2}{\bar{\varepsilon}^{11/3}}\frac{u_s}{d_p^2}\right]H,$ $Re_m = \frac{1+(1-\bar{\varepsilon}^{1/2})^{1/2}}{(1-\bar{\varepsilon})\bar{\varepsilon}^{1/6}}Re_p$	Max. relative difference: $\pm$15.08% of $f_{Liu}{}^{\dagger}$	$\bar{\varepsilon}$ = 0.36, 0.5916 [44, 95] $\bar{\varepsilon}$ = 0.4529, 0.6007	$\frac{d_p}{D} < 0.75$	$Re_m < 1,600$ (When $Re_m \sim 1,900$, the transition to turbulent flow is expected.)
KTA [96]	$\left[160\mu\frac{(1-\bar{\varepsilon})^2}{\bar{\varepsilon}^3}\frac{u_s}{d_p^2} + 3\left(\frac{1-\bar{\varepsilon}}{Re_p}\right)^{0.1}\rho_f\frac{(1-\bar{\varepsilon})}{\bar{\varepsilon}^3}\frac{u_s^2}{d_p}\right]H$	Uncertainty: $\pm$15% of $f_{KTA}{}^{\ddagger}$	$0.36 < \bar{\varepsilon} < 0.42$	$\frac{D}{d_p}$ above the limiting curve in [96], $H > 5d_p$	$1 < Re^* < 10^5$
Çarpinlioğlu and Özahi [97]	$139.57\left[\frac{1}{Re^*\bar{\varepsilon}^7}\frac{H}{d_p}\right]^{0.4733}\frac{\rho_f u_s^2}{2}$	Max. relative difference: $\pm$17% of ΔP	$0.36 \leq \bar{\varepsilon} \leq 0.56$	$\frac{D}{d_p} = 5.72 \sim 17.16$	$675 \leq Re^* \leq 7,772$
Carman [71]	$\left[180\mu\frac{(1-\bar{\varepsilon})^2}{\bar{\varepsilon}^3}\frac{u_s}{d_p^2} + 2.871\left(\frac{1-\bar{\varepsilon}}{Re_p}\right)^{0.1}\rho_f\frac{(1-\bar{\varepsilon})}{\bar{\varepsilon}^3}\frac{u_s^2}{d_p}\right]H$	-	$0.303 \leq \bar{\varepsilon} \leq 0.9$ from Table 2.10	$\frac{D}{d_p} > 10$	$0.06 < Re^* < 60,000$
Tallmadge[§] [72]	$\left[150\mu\frac{(1-\bar{\varepsilon})^2}{\bar{\varepsilon}^3}\frac{u_s}{d_p^2} + 4.2\left(\frac{1-\bar{\varepsilon}}{Re_p}\right)^{1/6}\rho_f\frac{(1-\bar{\varepsilon})}{\bar{\varepsilon}^3}\frac{u_s^2}{d_p}\right]H$	-	$0.354 \leq \bar{\varepsilon} \leq 0.882$ [98]	$\frac{D}{d_p} = 11.4$ [98]	$0.1 < Re^* < 10^5$

$^{\dagger} f_{Liu} = 85.2\left(1+\pi\frac{d_p}{6(1-\bar{\varepsilon})D}\right)^2 + \frac{0.69Re_m^3}{16^2+Re_m^2}\left[1-\frac{\pi^2 d_p}{24D}\left(1-\frac{0.5d_p}{D}\right)\right]$. $^{\ddagger} f_{KTA} = \frac{320}{Re^*} + \frac{6}{Re^{*0.1}}$.

[§]Tallmadge uses Wentz Jr and Thodos's experiments in Table 2.9.

Table 2.6. Continued.

Author	Correlation	Uncertainty or error	Validity condition		
			Porosity range	Aspect ratio range	Re^* or Re_p range
Brauer† [46]	$\left[160\mu\frac{(1-\bar{\varepsilon})^2}{\bar{\varepsilon}^3}\frac{u_s}{d_p^2}+3.1\left(\frac{1-\bar{\varepsilon}}{Re_p}\right)^{0.1}\rho_f\frac{(1-\bar{\varepsilon})}{\bar{\varepsilon}^3}\frac{u_s^2}{d_p}\right]H$	-	$0.375\leq\bar{\varepsilon}\leq 0.421$	$0.0195\leq\frac{d_p}{D}\leq 0.1585$	$2<Re^*<20,000$
Jones and Krier [70]	$\left[150\mu\frac{(1-\bar{\varepsilon})^2}{\bar{\varepsilon}^3}\frac{u_s}{d_p^2}+3.89\left(\frac{1-\bar{\varepsilon}}{Re_p}\right)^{0.13}\rho_f\frac{(1-\bar{\varepsilon})}{\bar{\varepsilon}^3}\frac{u_s^2}{d_p}\right]H$	Uncertainty: $\pm 6\%$ of f_{Jones}‡	$0.38\leq\bar{\varepsilon}\leq 0.44$	$8.5\leq\frac{D}{d_p}\leq 50$	$440<Re_p<76,000$
Kuo and Nydegger [77]	$\left[276.23\mu\frac{(1-\bar{\varepsilon})^2}{\bar{\varepsilon}^3}\frac{u_s}{d_p^2}+5.05\left(\frac{1-\bar{\varepsilon}}{Re_p}\right)^{0.13}\rho_f\frac{(1-\bar{\varepsilon})}{\bar{\varepsilon}^3}\frac{u_s^2}{d_p}\right]H$	-	$0.38\leq\bar{\varepsilon}\leq 0.39$ [70]	$\frac{D}{d_p}=9.4$ [99]	$460<Re_p<14,600$ [8]
Wirth [100, 101]	$\left[317\left(\frac{0.4}{\bar{\varepsilon}}\right)^{0.78}\mu\frac{(1-\bar{\varepsilon})^2}{\bar{\varepsilon}^3}\frac{u_s}{d_p^2}+6.17\left(\frac{1-\bar{\varepsilon}}{Re_p}\right)^{0.1}\rho_f\frac{(1-\bar{\varepsilon})}{\bar{\varepsilon}^3}\frac{u_s^2}{d_p}\right]\frac{H}{2}$	←	Inaccessible	→	$Re^*\leq 50,000$
Wentz Jr and Thodos [98]	$\left[\frac{0.351}{Re^{*0.05}-1.2}\rho_f\frac{(1-\bar{\varepsilon})}{\bar{\varepsilon}^3}\frac{u_s^2}{d_p}\right]H$ by eliminating the entrance and exit effects, $\left[\frac{0.396}{Re^{*0.05}-1.2}\rho_f\frac{(1-\bar{\varepsilon})}{\bar{\varepsilon}^3}\frac{u_s^2}{d_p}\right]H$ by including the entrance and exit effects	-	$0.354\leq\bar{\varepsilon}\leq 0.882$	$\frac{D}{d_p}=11.4$	$2,550<Re^*<64,900$

†Jeschar confirms the Brauer pressure drop correlation. The experimental setup is shown in Table 2.1. The validity conditions are also from Jeschar's experiments.
‡$f_{Jones}=150+3.89(Re^*)^{0.87}$.

Table 2.6. Continued.

Author	Correlation	Uncertainty or error	Validity condition		
			Porosity range	Aspect ratio range	Re^* or Re_p range
Erben [76]	$\left[\frac{3.3615}{Re^{*0.11}}\rho_f\frac{(1-\bar{\varepsilon})}{\bar{\varepsilon}^3}\frac{u_s^2}{d_p}\right]H$, cubic packing	Inaccessible	$\bar{\varepsilon} = 0.26, 0.476$	Inaccessible	$15,000 < Re^* < 80,000$
Hicks† [73]	$\left[\frac{6.8}{Re^{*0.2}}\rho_f\frac{(1-\bar{\varepsilon})}{\bar{\varepsilon}^3}\frac{u_s^2}{d_p}\right]H$	-	$0.354 \leq \bar{\varepsilon} \leq 0.728$ [79,98]	$8.47 \leq \frac{D}{d_p} \leq 25.4$ [79,98]	$300 < Re^* < 60,000$
Fahien and Schriver [8]	$\left[qf_{1L}\mu\frac{(1-\bar{\varepsilon})^2}{\bar{\varepsilon}^3}\frac{u_s}{d_p^2} + (1-q)\left(f_2+\frac{f_{1T}}{Re^*}\right)\rho_f\frac{(1-\bar{\varepsilon})}{\bar{\varepsilon}^3}\frac{u_s^2}{d_p}\right]H$, $q = exp\left(-\frac{\bar{\varepsilon}^2(1-\bar{\varepsilon})}{12.6}Re^*\right)$, $f_{1L} = \frac{136}{(1-\bar{\varepsilon})^{0.38}}$, $f_{1T} = \frac{29}{(1-\bar{\varepsilon})^{1.45}\bar{\varepsilon}^2}$, $f_2 = \frac{1.87\bar{\varepsilon}^{0.75}}{(1-\bar{\varepsilon})^{0.26}}$	←	Inaccessible		→
Lee and Ogawa‡ [102]	$\frac{1}{2}\left[\frac{12.5}{\bar{\varepsilon}^3}(1-\bar{\varepsilon})^2\right]\left[29.32Re_p^{-1} + 1.56Re_p^{-n} + 0.1\right]\rho_f\frac{u_s^2}{d_p}H$, $n = 0.352 + 0.1\bar{\varepsilon} + 0.275\bar{\varepsilon}^2$	Ave. relative error: ±20% of ΔP for the low Re range, ±40% of ΔP for the high Re range	$0.303 \leq \bar{\varepsilon} \leq 0.421$ [103]	$5.38 \leq \frac{D}{d_p} \leq 35.47$ [103]	$1 \leq Re_p \leq 10^3$, $10^3 \leq Re_p \leq 10^6$

†Hicks uses Handley's in Table 2.7 and Wentz Jr and Thodos's in Table 2.9.

‡Lee and Ogawa use Burke and Plummer's experiments in Table 2.9. Leva's experiments [104] are accounted for calculating the relative error between the experimental data and correlation for the high Re regime.

Table 2.6. Continued.

Author	Correlation	Uncertainty or error	Validity condition		
			Porosity range	Aspect ratio range	Re^* or Re_p range
Montillet et al.[†] [51]	$a\left(\frac{D}{d_p}\right)^{0.2}\left[\frac{1000}{Re_p}+60Re_p^{-0.5}+12\right]$ $\rho_f\frac{(1-\bar{\varepsilon})}{\bar{\varepsilon}^3}\frac{u_s^2}{d_p}H$, $a=0.061$ for dense packing, $a=0.05$ for loose packing	Max. average relative difference: $\pm$10.4% of α'[‡]	$0.36\leq\bar{\varepsilon}\leq 0.39$, $\bar{\varepsilon}=0.419$ for $\frac{D}{d_p}=3.8$	$3.8\leq\frac{D}{d_p}\leq 50$	$10<Re_p<2,500$
Montillet [105]	$0.066\left(\frac{D}{d_p}\right)^{0.17}\left[\frac{1000}{Re_p}+60Re_p^{-0.5}+12\right]$ $\rho_f\frac{(1-\bar{\varepsilon})}{\bar{\varepsilon}^3}\frac{u_s^2}{d_p}H$	Ave. relative difference: $\pm$1.6% of $f_{Montillet}$[§]	$\bar{\varepsilon}=0.367$	$\frac{D}{d_p}=12.2$	$30\leq Re_p\leq 1,500$
Rose [106]	$\left[\frac{1000}{Re_p}+60Re_p^{-0.5}+12\right]\rho_f\frac{u_s^2}{d_p}H$	Max. relative difference: $\pm$35% of f_{Rose}[**]	$0.325\leq\bar{\varepsilon}\leq 0.84$	-	$0.01<Re_p<10,000$
Rose and Rizk [107]	$\left[\frac{1000}{Re_p}+125Re_p^{-0.5}+14\right]\rho_f\frac{u_s^2}{d_p}H$	Max. relative difference: $\pm$20% of $f_{Rose\ and\ Rizk}$[††]	$0.3\leq\bar{\varepsilon}\leq 0.9$	$\frac{D}{d_p}=3.7, 10.25$ for spheres	$1,000<Re_p<6,000$
Kurten et al. [51]	$\left[\frac{25}{4\bar{\varepsilon}^3}(1-\bar{\varepsilon})^2\right]\left[\frac{21}{Re_p}+6Re_p^{-0.5}+0.28\right]\rho_f\frac{u_s^2}{d_p}H$	$\leftarrow$	Inaccessible	$\rightarrow$	$0.1<Re_p<4,000$

[†]Montillet's experiments are listed in Table 2.2.

[‡]$\alpha'=0.061\left(\frac{1-\bar{\varepsilon}}{\bar{\varepsilon}^3}\right)\left(\frac{D}{d_p}\right)^{0.2}\left[\frac{1000}{Re_p}+60Re_p^{-0.5}+12\right]$. [§]$f_{Montillet}=0.066\left(\frac{D}{d_p}\right)^{0.17}\left(\frac{1-\bar{\varepsilon}}{\bar{\varepsilon}^3}\right)\left[\frac{1000}{Re_p}+60Re_p^{-0.5}+12\right]$. [**]$f_{Rose}=\frac{1000}{Re_p}+\frac{200}{\sqrt{Re_p}}+12$.

[††]$f_{Rose\ and\ Rizk}=\frac{1000}{Re_p}+\frac{125}{\sqrt{Re_p}}+14$.

Table 2.7. Experimental setups for pressure drop correlations.

Author	Bed diameter (mm)	Pebble diameter (mm)	Material for spheres/packing method	Material for the column/column height (mm)	Material for the fluid/operating condition
Ergun [74]	15.2	-	Glass spheres/random packing with vibration	-	Nitrogen/fluid mass flow rate from 0.1086 g/s to 0.362 g/s, exit at 21^{o}C and 0.95 atm
Handley [79]	76.2	3, 6, 9	Glass spheres/pouring particles into the bed with continuous tamping	-/101.6, 152.4, 203.2	Air/heat transfer
Özahi et al. [80], Çarpinlioğlu and Özahi [97]	103	16	Glass beads/ random loose packing	Polyvinyl chloride pipe/ 25, 40, 60, 150	Air/ mean exit fluid superficial velocity from 1.08 m/s to 2.85 m/s, isothermal condition
Yu et al. [82]	360, 480, 600	12, 16, 20	Aluminous refractory spheres/random packing	-/100 $\sim$ 500	Blast furnace gas, blended gas, natural gas/ heated experiments
Hayes et al. [88]	25.3	2.5 $\sim$ 6.01	No material, but smooth uniform spheres/-	Plexiglass tubing/305 mm test section	Water/-
Fand et al. [95]	86.6	2.098 $\sim$ 4.029	Same as [44] and described in Table 2.1		
Mehta and Hawley [93]	12.7	-	Uniform spherical glass beads/no specific packing method	Glass column/ 457.2	Water/isothermal condition

Table 2.7. Continued.

Author	Bed diameter (mm)	Pebble diameter (mm)	Material for spheres/packing method	Material for the column/column height (mm)	Material for the fluid/operating condition
Hassan and Kang [7]	120.65	33.02	Polymethyl methacrylate/random packing	Same material as spheres/ 1,524 (Multiple pressure measurements throughout the column)	Water/no heat
Liu et al.† [69]	4.47	1.917, 3.184	Glass beads/wet packing with gentle tapping	Polyethylene tubing, circular with elliptical deforma- tion/400 mm total (30 mm and 100 mm pressure taps)	Water for high flow rates and hydraulic oil for low flow rates/21^{o}C
Jones and Krier [70]	50.8	$0.96 \sim 6$	Glass beads/-	-/200	Air/physical velocity at 10 m/s at the room temperature with the 1 mm pebble diameter
Rose and Rizk‡ [107]	115	11.2, 31	Porcelain spheres/random packing	-/762	Air/-

†Liu et al. use Fand and Thinakaran's experiments in Table 2.1 with $d_p = 3.04$ mm and $D = 5.588$ mm. In addition, Liu et al. consider Fand's experiments in this table with $d_p = 3.072$ mm [44, 95].
‡Rose and Rizk also use Burke and Plummer's experiments in Table 2.9, Bakhmeteff and Feodoroff's experiments, and Mavis and Wilsey's experiments in Table 2.11.

Table 2.8. Experimental setups for the pressure drop correlations derived by Macdonald et al. and Wu et al.

Author	Bed diameter (mm)	Pebble diameter (mm)	Material for spheres/packing method	Material for the column/column height (mm)	Material for the fluid/operating condition
Rumpf and Gupte [84]	100	0.408 $\sim$ 0.677	Polystyrene balls/uniformly random packed	Metal cylinder/-	Air flow/20^{o}C
Kyan et al. [85]	44.45	0.008 $\sim$ 0.028 (Fiber diameter)	Glass, nylon, Dacron fibrous bed/randomly packed	Plexiglass test section/ pressure drop measured within the 76.2 mm bed	Water and aqueous glycerol/ viscosity varying from 0.001 Pa·s to 0.022 Pa·s
Dudgeon [86]	571.5	16, 24.9, 29	Glass marbles/ random packing	-/1,219.2	Water/superficial velocity from 0.00024 m/s to 0.34 m/s, flow direction: top to bottom
Fancher and Lewis [87]	19.05, 25.4	0.375 $\sim$ 1 (Ave. grain size)	Lead shots, Ottawa sand, flint sand (Unconsolidated)/shaken	-/335 $\sim$ 15,480	Bradford crude oil, air, tap water/superficial velocity of water up to 0.024 m/s or oil up to 0.0036 m/s
Wang et al.† [91]	100	10	Glass balls/cyclones	Acrylic Perspex glass column/100 mm interval	Air/superficial velocity up to 0.6 m/s at the ambient condition

†Wang's experiments are for the Wu pressure drop function, and others are for the Macdonald pressure drop correlation. Wu et al. also use Yu's experiments in Table 2.7.

Table 2.9. Experimental setups for the pressure drop correlation derived by Eisfeld and Schnitzlein[†].

Author	Bed diameter (mm)	Pebble diameter (mm)	Material for spheres/packing method	Material for the column/column height (mm)	Material for the fluid/operating condition
Andersson [108]	75.545	5.21	Glass beads/ inaccessible	Inaccessible	Water/ inaccessible
Burke and Plummer [103]	17.94, 34.1, 52.5, 78.1	1.48, 3.08, 6.34	Lead shots/ random pouring or hammering the column	Glass, galvanized iron pipe/-	Air saturated with water vapor/ superficial velocity from 0.033 m/s to 0.621 m/s at 27^oC
Ergun and Orning [109]	25.4	0.227 $\sim$ 0.57	Glass beads/random packing	Glass tube/762	Hydrogen, nitrogen, carbon dioxide/superficial velocity up to 1 m/s, isothermal condition
Leva [110]	20.93 $\sim$ 77.93	2.25 $\sim$ 18.54	Glass spheres/ dumping the packing material randomly	Standard pipe/ 276.23 $\sim$ 946.15 (Air), 298.45 (N_2)	Air, nitrogen/ mass flow rate: 0.51 g/s $\sim$ 13.2 g/s (Air), 0.6 g/s $\sim$ 2.86 g/s (N_2), average temperature: 18.9^{o}C $\sim$ 30^{o}C (Air), 21.4^{o}C $\sim$ 25.3^{o}C (N_2)
Wentz Jr and Thodos [98]	355.6	31.242	Smooth plastic phenolic spheres/cubic, body-centered cubic, and face-centered cubic orientations	Cylindrical wind tunnel/38.608 $\sim$ 251.46	Air/superficial velocity from 0.76 m/s to 4.1 m/s

[†]Eisfeld and Schnitzlein furthermore use Jeschar's and Reichelt's in Table 2.1 and Table 2.2, respectively.

Table 2.10. Experimental setups for the pressure drop correlation derived by Carman† [71].

Author	Bed diameter (mm)	Pebble diameter (mm)	Material for spheres/packing method	Material for the column/column height (mm)	Material for the fluid/operating condition
Schriever [111]	50	0.252 ∼ 1.025	Glass spheres/loose to tight packing	-/100, 220	Oil (Nujol)/98.5^{o}C ∼ 99.4^{o}C
Green and Ampt [112]	30.05, 21.31	0.25 ∼ 0.938	Glass beads/different compactness	Glass capillary tube/ 121.3, 236	Water and air/ air at 8.5^{o}C ∼ 10.5^{o}C
Muskat and Botset [113]	31.7	0.632	Glass beads/ random packing without shaking	Steel tube/920	Air at the isothermal condition
Chalmers et al. [114]	38.1 ∼ 76.2	1.27 ∼ 4.06	Lead shots/ pounding with hammers until the stabilization	Brass tubing/ 203.2 mm for pressure measurements	Natural gas/ superficial velocity from 0.0015 m/s to 0.063 m/s, initial temperature of 21.1^{o}C
Furnas [115]	46, 52	1.38 ∼ 9.05	Lead shots/ vibrating the container for packing	Iron pipe/762	Air/1 m/s at 25^{o}C to 1,000^{o}C

†Burke and Plummer's experiments in Table 2.9 are also accounted for developing the Carman pressure drop function.

Table 2.11. Experimental setups for the pressure drop correlation derived by Rose† [106].

Author	Bed diameter (mm)	Pebble diameter (mm)	Material for spheres/packing method	Material for the column/column height (mm)	Material for the fluid/operating condition
Bakhmeteff and Feodoroff [116]	76.2	0.96 $\sim$ 9.17	Lead shots/ uniform packing	Brass pipe/ 609.6, 1,524	Water/reduced superficial velocity ($u_s/\varepsilon^{2/3}$) from 0.00018 m/s to 0.46 m/s
Mavis and Wilsey [117]	152.4	0.16 $\sim$ 1.8, 0.68 $\sim$ 0.93	Iowa river sand, nearly uniform-sized Ottawa sand/ grains collected upon shaking	Cast iron pipe/ 914.4	Water/superficial velocity from 1.23×10^{-5} m/s to 0.00071 m/s at 15.6^{o}C
Traxler and Baum [118]	27.8, 22.3	0.001066, 0.00108 (Pore diameter)	Silica dust/ uniform packing by hand or machine tapping	Glass tube/ 50, 100	Air/superficial velocity from 4.4×10^{-5} m/s to 5.7×10^{-5} m/s at 25^{o}C
Chilton and Colburn [119]	76.2	3.175 $\sim$ 25.4	Zinc balls, porcelain balls, granules, pebbles/-	-/1,155.19	Air/heat transfer, mass velocity from 1.17 kg/(m^2·s) to 7.76 kg/(m^2·s)

†Fancher and Lewis's in Table 2.8, Burke and Plummer's in Table 2.9, Green and Ampt's, and Muskat and Botset's experiments in Table 2.10 are used for the Rose pressure drop function.

2.7 Solid-Fluid Convective Heat Transfer Coefficient

The solid-fluid convective heat transfer coefficient, α, is calculated by multiplying the convective heat transfer coefficient at the pebble surfaces by the interaction area density [10].

$$\alpha = \frac{6(1-\varepsilon)}{d_p}\frac{Nuk_f}{d_p}. \tag{2.8}$$

For the SANA experiments, the Nu is estimated by the Petrovic and Thodos correlated mass transfer data [120]:

$$Nu = 0.357 \frac{Pr^{1/3}}{\varepsilon} Re_p^{0.641}, \tag{2.9}$$

where $Pr = \frac{C_{p,f}\mu}{k_f}$. This correlation properly evaluates the Nu for $3 \leq Re_p \leq 230$. For the low Reynolds SANA system, the Petrovic and Thodos model would more accurately predict the Nu relative to the KTA, Gnielinski, and Gunn correlations by applying thermal dispersion corrections [10].

The Nu is calculated by the KTA correlation for the scaling study [121]:

$$Nu = 1.27 \frac{Pr^{1/3} Re_p^{0.36}}{\varepsilon^{1.18}} + 0.033 \frac{Pr^{0.5} Re_p^{0.86}}{\varepsilon^{1.07}}, \tag{2.10}$$

where the dynamic viscosity and thermal conductivity of the gas are determined at the average temperature of the fluid and solid. The KTA correlation for the Nu is valid, where $100 < Re_p < 10^5$, $0.36 < \varepsilon < 0.42$, $D/d_p > 20$, and $H > 4d_p$. The aspect ratio of the HTR-PM model is less than 20 but still higher than 15. Therefore, it is assumed that the near-wall effects do not have much impact to change the Nu significantly. In addition, the Gunn correlation (valid for $0.35 \leq \varepsilon \leq 1$ and $Re_p \leq 10^5$) provides another scaling ratio of the solid-fluid convective heat transfer coefficient [122]:

$$\begin{aligned} Nu = &\left(7 - 10\varepsilon + 5\varepsilon^2\right)\left(1 + 0.7 Re_p^{0.2} Pr^{1/3}\right) \\ &+ \left(1.33 - 2.4\varepsilon + 1.2\varepsilon^2\right) Re_p^{0.7} Pr^{1/3}. \end{aligned} \tag{2.11}$$

2.8 Effective Fluid & Solid Thermal Conductivities

Thermal dispersion increases the heat transfer in the fluid due to additional mixing and diffusive effects caused by tortuous flow paths around the pebbles. It is accounted for the SANA experiments by computing the effective fluid thermal conductivity, κ_f, as:

$$\kappa_f = \varepsilon k_f + C_o Pe k_f, \tag{2.12}$$

where C_o is a proportionality constant equal to 0.11 [123]. However, the effective fluid thermal

conductivity can also be estimated by Equation 2.13 for high Reynolds numbers since thermal dispersion is neglected for most of the PBR porous media models [10, 124, 125].

$$\kappa_f = \varepsilon k_f. \tag{2.13}$$

The effective solid thermal conductivity, κ_s, accounts for three parallel heat transfer paths shown in Figure 2.3 [10]: 1) conduction in a pebble (represented by the blue lines) and radiation between pebbles (represented by red lines), 2) conduction both in a pebble and in the fluid between pebbles (represented by green lines), and 3) conduction in a pebble and conduction between pebbles through the contact areas (represented by pink lines). Therefore, the effective solid thermal conductivity is calculated by:

$$\kappa_s = \kappa_{radiation} + \kappa_{fluid\ conduction} + \kappa_{solid\ conduction}. \tag{2.14}$$

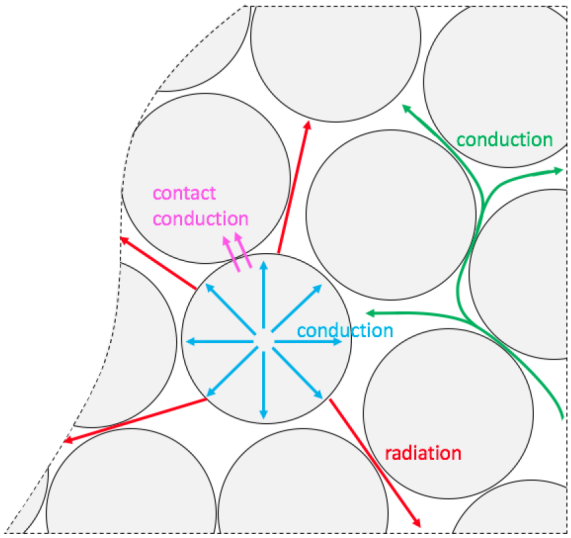

Figure 2.3. Different heat transfer paths in the pebble bed. Reprinted from [10].

First, the Breitbach and Barthels correlation considers the radiative heat transfer in the fluid and conduction in spheres [126]. It is developed based on the Zehner and Schlünder cell model:

$$\kappa_{radiation} = \left[\left(1 - \sqrt{1-\varepsilon}\right) \varepsilon + \frac{\sqrt{1-\varepsilon}}{2/\varepsilon_r - 1} \frac{B'+1}{B'} \frac{1}{1 + \frac{1}{(2/\varepsilon_r - 1)\Lambda}} \right] 4\sigma' T_s^3 d_p, \tag{2.15}$$

where $B' = 1.25\left(\frac{1-\varepsilon}{\varepsilon}\right)^{10/9}$, and $\Lambda = \frac{k_s}{4\sigma' T_s^3 d_p}$. The effective solid thermal conductivity goes to infinity when the porosity becomes one at the walls. Therefore, the Tsotsas modified model for the radiation component is used within the $d_p/2$ distance from the walls [127, 128]:

$$\kappa_{radiation} = \left(1 - \sqrt{1-\varepsilon}\right) \frac{k_s}{\Lambda k_f (2/\varepsilon_r - 1)} + \sqrt{1-\varepsilon} \frac{k_s/k_f}{\Lambda(2/\varepsilon_r - 1) + 1}. \tag{2.16}$$

The Zehner and Schlünder model is used for the solid conduction and fluid conduction [126, 129, 130]:

$$\begin{aligned} \kappa_{fluid\ conduction} &= k_f \left(1 - \sqrt{1-\varepsilon}\right) + k_f \frac{2\sqrt{1-\varepsilon}}{1-\lambda B'} \\ &\times \left[\frac{(1-\lambda)B'}{(1-\lambda B')^2} ln\left(\frac{1}{\lambda B'}\right) - \frac{B'+1}{2} - \frac{B'-1}{1-\lambda B'} \right], \end{aligned} \tag{2.17}$$

where $\lambda = \frac{k_f}{k_s}$. At last, the Chan and Tien model is built to estimate the effective thermal conductivity of the contact conduction [10, 131].

$$\kappa_{solid\ conduction} = \frac{1}{2 \cdot 0.53} \frac{N_A}{N_L} \left[\frac{3}{4} \frac{1-\nu_p^2}{E_s} \frac{4F}{d_p^2} \right]^{1/3} d_p k_s. \tag{2.18}$$

$F = S_F \frac{p}{N_A}$ where p is the pressure exerted by the weight of pebbles. It is calculated by:

$$p = (1 - \varepsilon_\infty) \rho_s H(y) |g_y|. \tag{2.19}$$

The values of N_A, N_L, and S_F for the simple, body-centered, and face-centered cubic packings are provided in [131].

2.9 Turbulence Modeling with Explicit Meshing

Turbulence modeling with explicit meshing of the fluid flow region around pebbles can provide more details of the flow effects in the PBRs compared to the macro-scale approach. The following two-equation turbulence models are applied to estimate the pressure drop within specific bed heights and the fluid axial velocities averaged in the porous bed volumes or the PIV window. Less computational effort is expected relative to the Reynolds stress transport turbulence model, large

eddy simulations, or direct numerical simulations.

2.9.1 Realizable Two-Layer $k-\varepsilon$ Model

The realizable two-layer $k-\varepsilon$ model explicitly specifies the turbulent dissipation rate, ε, and turbulent eddy viscosity, μ_t, in the layer near the wall [132]. The governing equations of the standard $k-\varepsilon$ model follow as [133]:

$$\frac{\partial \overline{u}_i}{\partial x_i} = 0. \tag{2.20}$$

$$\frac{\partial \overline{u}_i}{\partial t} + \frac{\partial \overline{u}_j \overline{u}_i}{\partial x_j} = -\frac{1}{\rho_f}\frac{\partial \overline{P}}{\partial x_i} + \frac{\partial}{\partial x_j}\left(\nu\left(\frac{\partial \overline{u}_i}{\partial x_j} + \frac{\partial \overline{u}_j}{\partial x_i}\right) - \overline{u_i' u_j'}\right). \tag{2.21}$$

$$\frac{\partial k}{\partial t} + \frac{\partial \overline{u}_j k}{\partial x_j} = \frac{\partial}{\partial x_j}\left(\left(\nu + \frac{\nu_t}{\sigma_k}\right)\frac{\partial k}{\partial x_j}\right) - \overline{u_i' u_j'}\frac{\partial \overline{u}_i}{\partial x_j} - \varepsilon. \tag{2.22}$$

$$\frac{\partial \varepsilon}{\partial t} + \frac{\partial \overline{u}_j \varepsilon}{\partial x_j} = \frac{\partial}{\partial x_j}\left(\left(\nu + \frac{\nu_t}{\sigma_\varepsilon}\right)\frac{\partial \varepsilon}{\partial x_j}\right) + \left(-C_{\varepsilon 1}\overline{u_i' u_j'}\frac{\partial \overline{u}_i}{\partial x_j} - C_{\varepsilon 2}\varepsilon\right)\frac{\varepsilon}{k}. \tag{2.23}$$

The model coefficients of σ_k, σ_ε, $C_{\varepsilon 1}$, and $C_{\varepsilon 2}$ are provided in Table 2.12 [132]. However, the realizable two-layer $k-\varepsilon$ model requires a new formation of the turbulent dissipation rate transport equation, as shown in Equation 2.24 [134], and a damping function, f_μ, which satisfies the realizability of the Reynolds stresses.

Table 2.12. Model coefficients of the $k-\varepsilon$ models. Adapted from [132].

Model	σ_k	σ_ε	$C_{\varepsilon 1}$	$C_{\varepsilon 2}$	C_μ
Standard $k-\varepsilon$ [132]	1	1.3	1.44	1.92	0.09
Realizable two-layer $k-\varepsilon$ [134]	1	1.2	$\max\left(0.43, \frac{\eta}{5+\eta}\right)$ where $\eta = \frac{Sk}{\varepsilon}$†	1.9	0.09

†$S = \sqrt{2S_{ij}S_{ij}}$, $S_{ij} = \frac{1}{2}\left(\frac{\partial \overline{u}_i}{\partial x_j} + \frac{\partial \overline{u}_j}{\partial x_i}\right)$.

$$\frac{\partial \varepsilon}{\partial t} + \frac{\partial \overline{u}_j \varepsilon}{\partial x_j} = \frac{\partial}{\partial x_j}\left(\left(\nu + \frac{\nu_t}{\sigma_\varepsilon}\right)\frac{\partial \varepsilon}{\partial x_j}\right) + C_{\varepsilon 1} S\varepsilon - C_{\varepsilon 2}\frac{\varepsilon^2}{k + \sqrt{\nu\varepsilon}}. \tag{2.24}$$

The Boussinesq hypothesis describes the momentum transfer due to turbulent eddies modeled by applying the turbulent eddy viscosity [135]. The Reynolds stress tensor is modeled by [136]:

$$-\overline{u_i' u_j'} = \nu_t \left(\frac{\partial \overline{u}_i}{\partial x_j} + \frac{\partial \overline{u}_j}{\partial x_i} \right) - \frac{2}{3} k \delta_{ij}, \tag{2.25}$$

given the incompressible flow. The turbulent kinetic energy, k, is defined by:

$$k = \frac{1}{2} \overline{u_i' u_i'}. \tag{2.26}$$

The turbulent eddy viscosity, μ_t, is calculated as [132]:

$$\mu_t = \rho_f \frac{C_\mu f_\mu k^2}{\varepsilon}, \tag{2.27}$$

where f_μ is 1 for the standard $k - \varepsilon$ model while the realizable two-layer $k - \varepsilon$ model uses f_μ as [134, 137]:

$$f_\mu = \frac{1}{C_\mu \left[4 + \sqrt{6} cos \left(\frac{1}{3} cos^{-1} \left(\sqrt{6} \frac{S_{ij} S_{jk} S_{ki}}{(S_{ij} S_{ij})^{3/2}} \right) \right) \frac{k}{\varepsilon} \sqrt{S_{ij} S_{ij} + \tilde{W}_{ij} \tilde{W}_{ij}} \right]}. \tag{2.28}$$

S_{ij} is defined in the footnote of Table 2.12, and W_{ij} is calculated as:

$$W_{ij} = \frac{1}{2} \left(\frac{\partial \overline{u}_i}{\partial x_j} - \frac{\partial \overline{u}_j}{\partial x_i} \right). \tag{2.29}$$

$$\tilde{W}_{ij} = W_{ij} - 2 \varepsilon_{ijk} \omega_k. \tag{2.30}$$

Due to the complex near-wall phenomena, the two-layer approach is formulated with the Wolfstein shear-driven flow. The dissipation rate near the wall is defined as:

$$\varepsilon = \frac{k^{3/2}}{l_\varepsilon}, \tag{2.31}$$

where l_ε is the Wolfstein length scale function defined by [135, 138]:

$$l_\varepsilon = 0.42 (C_\mu)^{-3/4} d \left[1 - exp \left(- \frac{Re_d}{0.84 (C_\mu)^{-3/4}} \right) \right]. \tag{2.32}$$

The two-layer turbulent viscosity value is determined by:

$$\left(\frac{\mu_t}{\mu} \right)_{Two\ layer} = 0.42 Re_d (C_\mu)^{1/4} \left[1 - exp \left(- \frac{Re_d}{70} \right) \right]. \tag{2.33}$$

Consequently, the turbulent viscosity from the $k - \varepsilon$ model gets blended with the empirically prescribed value in the near-wall regions by applying the wall-proximity indicator [132]. Although the two-layer model is more expensive than wall functions, it is beneficial in capturing the near-wall phenomena [135]. In

addition, the all-y^+ wall treatment uses the blended wall function proposed by Reichardt [139] to calculate the velocity. Fine meshes with $y^+ < 5$ are used to resolve the viscosity-affected region of the tortuous fluid flow between pebbles, and y^+ is defined by:

$$y^+ = \frac{du_\tau}{\nu}. \tag{2.34}$$

2.9.2 SST $k-\omega$ Model

The SST $k-\omega$ method models the near-wall effects more adequately than the $k-\varepsilon$ models. The approach utilizes a $k-\varepsilon$ model in the free stream with a $k-\omega$ model near the wall [132]. The governing equations of the SST $k-\omega$ model are [140, 141]:

$$\frac{\partial k}{\partial t} + \frac{\partial \overline{u}_j k}{\partial x_j} = \frac{\partial}{\partial x_j}\left(\left(\nu + \nu_t \sigma_k\right)\frac{\partial k}{\partial x_j}\right) - \overline{u_i' u_j'}\frac{\partial \overline{u}_i}{\partial x_j} - \beta^* f_{\beta^*} k\omega. \tag{2.35}$$

$$\begin{aligned}\frac{\partial \omega}{\partial t} + \frac{\partial \overline{u}_j \omega}{\partial x_j} = \frac{\partial}{\partial x_j}\left(\left(\nu + \nu_t \sigma_\omega\right)\frac{\partial \omega}{\partial x_j}\right) + \gamma S^2 - \beta f_\beta \omega^2 \\ +2(1-F_1)\sigma_{\omega 2}\frac{1}{\omega}\frac{\partial k}{\partial x_j}\frac{\partial \omega}{\partial x_j}.\end{aligned} \tag{2.36}$$

The blending function, F_1, is

$$\tanh\left(\left[\min\left(\max\left(\frac{\sqrt{k}}{0.09\omega d}, \frac{500\nu}{d^2\omega}\right), \frac{2k}{d^2 CD_{k\omega}}\right)\right]^4\right), \tag{2.37}$$

where $CD_{k\omega}$ is the cross-diffusion coefficient calculated by:

$$CD_{k\omega} = \max\left(\frac{1}{\omega}\frac{\partial k}{\partial x_j}\frac{\partial \omega}{\partial x_j}, 10^{-20}\right). \tag{2.38}$$

The model coefficients, ϕ, are calculated as:

$$\phi = F_1\phi_1 + (1-F_1)\phi_2, \text{ and} \tag{2.39}$$

Table 2.13 provides the new sets of coefficients for the SST $k-\omega$ model [132]. In addition, γ is calculated the same way as Equation 2.39, with γ_1 and γ_2 defined as:

$$\gamma_1 = \frac{\beta_1}{\beta_1^*} - \sigma_{\omega 1}\kappa^2/\sqrt{\beta_1^*}, \text{ and} \tag{2.40}$$

$$\gamma_2 = \frac{\beta_2}{\beta_2^*} - \sigma_{\omega 2}\kappa^2/\sqrt{\beta_2^*}, \tag{2.41}$$

where κ = 0.41. The turbulent viscosity is calculated by:

$$\mu_t = \rho_f k \min\left(\frac{\alpha^*}{\omega}, \frac{0.31}{SF_2}\right), \tag{2.42}$$

where $\alpha^* = 1$, and

$$F_2 = \tanh\left(\left(\max\left(\frac{2\sqrt{k}}{\beta^*\omega d}, \frac{500\nu}{d^2\omega}\right)\right)^2\right). \tag{2.43}$$

Lastly, the free-shear modification factor, f_{β^*}, and the vortex-stretching modification factor, f_β, are:

$$f_\beta^* = \begin{cases} 1 & \text{for } \chi_k \leq 0 \\ \dfrac{1+680\chi_k^2}{1+400\chi_k^2} & \text{for } \chi_k > 0, \end{cases} \tag{2.44}$$

where $\chi_k = \frac{1}{\omega^3}\frac{\partial k}{\partial x_j}\frac{\partial \omega}{\partial x_j}$ and

$$f_\beta = \frac{1+70\chi_\omega}{1+80\chi_\omega}, \tag{2.45}$$

where $\chi_\omega = \frac{W_{ij}W_{jk}S_{ki}}{(\beta^*\omega)^3}$.

Table 2.13. Model coefficients of the SST $k-\omega$ model. Adapted from [132].

Model	σ_{k1}	σ_{k2}	$\sigma_{\omega1}$	$\sigma_{\omega2}$	β_1	β_2	β_1^*	β_2^*
SST $k-\omega$	0.85	1	0.5	0.856	0.075	0.0828	0.09	0.09

2.10 Simulation Uncertainty Quantification

The simulation uncertainty results from three different sources: numerical, input, and model uncertainties [142]. The numerical uncertainty, u_{num}, arises from discretization error, assuming that double precision round-off error is negligible, and an iterative convergence tolerance set to 10^{-6} sufficiently converges the solutions [143]. The input uncertainty, u_{input}, comes from uncertain input parameters, such as the porosity and fluid flow rate. The model formulation based on specific assumptions causes the model uncertainty, u_{model}, which is considered as a *completely* epistemic uncertainty due to lack of the inferable knowledge in the model [144]. Assuming all the errors are independent, the overall simulation uncertainty, u_P, is

determined to be [145]:

$$u_P = \sqrt{u_{num}^2 + u_{input}^2 + u_{model}^2}. \tag{2.46}$$

2.10.1 Mesh Convergence Study & Numerical Uncertainty Quantification

The mesh convergence study estimates the discretization error in CFD simulations [144,146,147]. When numerical coarse, medium, and fine mesh solutions are in the asymptotic range and the observed order of accuracy, $\hat{p}$, is close to the formal order of accuracy, $\bar{p}$, of the discretization scheme, the Richardson extrapolation (RE) can be used to predict the quantity for a mesh with an infinite number of elements [144]. First, given a constant mesh refinement ratio, the observed order of accuracy or observed convergence rate is determined by [144, 146, 147]:

$$\hat{p} = \frac{ln\left(\frac{f_3 - f_2}{f_2 - f_1}\right)}{ln(r)}, \tag{2.47}$$

where f is the quantity of interest and the subscripts 1, 2, and 3 represent the fine, medium, and coarse mesh, respectively. The uniform refinement ratio can be calculated by:

$$r = \frac{h_2}{h_1} = \frac{h_3}{h_2} > 1. \tag{2.48}$$

For three-dimensional calculations, the mesh size is calculated by [148]:

$$h = \left[\frac{1}{N}\sum_{i=1}^{N}(\Delta V_i)\right]^{1/3}. \tag{2.49}$$

The Richardson extrapolated value of the exact solution is:

$$f_{(h=0)} \simeq f_1 + \frac{f_1 - f_2}{r^{\hat{p}} - 1}. \tag{2.50}$$

For practical simulations, the observed order of accuracy is often greater than or equal to 0.5, and it is less than or equal to the formal order of accuracy [144].

The grid convergence index (GCI) describes the discretization error compared to the asymptotic numerical value in a percentage or without the normalization to ensure a 95% confidence level for the computed value [144, 147]. The two GCIs are computed by Equation 2.51, provided that the refinement ratio for three different mesh refinement levels is constant.

$$GCI_{21} = F_s\frac{|e_{21}|}{r^p - 1}, \text{ and } GCI_{32} = F_s\frac{|e_{32}|}{r^p - 1}, \tag{2.51}$$

where e_{21} and e_{32} are the relative errors defined by:

$$e_{21} = \frac{f_2 - f_1}{f_1}, \text{ and } e_{32} = \frac{f_3 - f_2}{f_2}. \tag{2.52}$$

In Equation 2.51, the value of p is selected by Table 2.14. When the observed order of accuracy, $\hat{p}$, matches the formal order of accuracy within 10%, the formal order of accuracy can be used for the GCI method [144]. The implementation of min(max(0.5, $\hat{p}$), $\bar{p}$) is applied if the discrepancy is above 10%. Furthermore, recent GCI implementations neglect the normalization, and an uncertainty estimate is provided in the same unit of the fine mesh solution.

$$GCI_{21} = F_s \frac{|f_2 - f_1|}{r^p - 1}. \tag{2.53}$$

The solutions from all three mesh refinement levels are in the asymptotic range of convergence by satisfying Equation 2.54 [146].

$$GCI_{32} = r^p GCI_{21}. \tag{2.54}$$

Table 2.14. Implementation of the GCI method. Adapted from [144].

Condition	p	F_s
$\left\|\frac{\hat{p}-\bar{p}}{\bar{p}}\right\| \leq 0.1$	$\bar{p}$	1.25
$\left\|\frac{\hat{p}-\bar{p}}{\bar{p}}\right\| > 0.1$	min(max(0.5, $\hat{p}$), $\bar{p}$)	3.0

The valid assumptions for the applicability of the RE or GCI method are still questionable; however, the RE is applied with non-uniform meshes [149], the solutions with the oscillatory convergence are used to calculate the GCI [148, 149], and the RE is used for the unstructured meshes [148, 150].

2.10.2 Input Uncertainty Quantification

Latin hypercube sampling (LHS) is used to estimate the input uncertainty propagation of CFD simulations. It selects one sample from each sub-domain with an equal probability content [151]. It is more computationally efficient than a simple random sampling (Monte Carlo) method. The uncertainties for the material properties are trivial due to the small uncertainties from temperature ($\sim 1^o$C) and pressure measurements. Therefore, the input parameters of the average bed porosity and inlet physical velocity, which notably

influence the pressure drop, are considered for the LHS method, specifically for porous media simulations. The geometric uncertainty of 0.794 mm is also accounted for.

2.10.3 Model Uncertainty Quantification

The American Society of Mechanical Engineers V&V standard [152] is followed to determine the model uncertainty. With a 95% confidence interval, the uncertainty is twice the SEM of the sampling distribution [145, 151, 153]. Here, the error is the length between a predicted or measured quantity and its true value. Given the numerical uncertainty is calculated by the GCI method and the input uncertainty is estimated by LHS, the upper and lower bounds for an asymmetric model uncertainty interval are defined as [145]:

$$\begin{aligned} u_{model}^{upper} &= E - \sqrt{u_{num}^2 + u_{input}^2 + u_D^2}. \\ u_{model}^{lower} &= E + \sqrt{u_{num}^2 + u_{input}^2 + u_D^2}, \end{aligned} \tag{2.55}$$

where u_D is the experimental uncertainty, with its quantification method shown in Section 2.11. Here, $E = P - D$, where P is the simulation result and D is the experimental data. Consequently, the upper and lower bounds of the overall simulation uncertainty would be:

$$\begin{aligned} u_P^{upper} &= \sqrt{u_{num}^2 + u_{input}^2 + \left(u_{model}^{upper}\right)^2}. \\ u_P^{lower} &= \sqrt{u_{num}^2 + u_{input}^2 + \left(u_{model}^{lower}\right)^2}. \end{aligned} \tag{2.56}$$

2.11 Experimental Uncertainty Quantification

The experimental uncertainty comes from systematic and random sources [154]. The calibration error can be used as the systematic error, δ_{sys}, while the random error, δ_{ran}, of the sampled average is calculated by using N multiple measurements as [155]:

$$\delta_{ran} = \sqrt{\frac{\sum_{i=1}^{N}(f_i - \bar{f})^2}{N-1}}/\sqrt{N}, \tag{2.57}$$

where f_i is the i-th measurement and $\bar{f}$ is the average of N measurements. By using the root sum squared method, the experimental uncertainty is calculated by:

$$u_D = \sqrt{\delta_{sys}^2 + (t\delta_{ran})^2}, \tag{2.58}$$

where a t-value is obtained at the specific degrees of freedom, $N - 1$.

2.12 Validation Metrics

The deterministic validation metric, such as the RMSE or Minkowski distance, treats the experimental and simulation data as point values without uncertainties [156]. The RMSE is calculated by:

$$d_{RMSE} = \sqrt{\frac{1}{N}\sum_{i}^{N}(P_i - D_i)^2}. \tag{2.59}$$

Similarly, the RMSRE or relative root mean square error (RRMSE) is calculated by [157–160]:

$$d_{RMSRE} = \sqrt{\frac{1}{N}\sum_{i}^{N}\left(\frac{P_i - D_i}{D_i}\right)^2}. \tag{2.60}$$

$$d_{RRMSE} = \frac{\sqrt{\frac{1}{N}\sum_{i}^{N}(P_i - D_i)^2}}{\bar{D}} \times 100\ (\%). \tag{2.61}$$

The Minkowski distance is determined to be [161]:

$$l_p = \left(\sum_{i=1}^{N}|P_i - D_i|^p\right)^{1/p}. \tag{2.62}$$

With $p = 1$, the average relative difference between the experimental and simulation data would be:

$$\bar{l}_1 = \frac{1}{N}\sum_{i=1}^{N}\frac{|P_i - D_i|}{|D_i|}. \tag{2.63}$$

In addition, with $p = 2$, an averaged Euclidean distance, l_2/N, can be another deterministic metric.

If uncertainties are provided for either experimental or simulation data, the probabilistic metric, such as the average of the total normalized Euclidean distance, $\bar{d}_{NE}$, can be utilized given that the other data is observed as point values [156]:

$$\bar{d}_{NE} = \sqrt{\sum_{i=1}^{N}\frac{(P_i - D_i)^2}{\sigma_i^2}}\ /N, \tag{2.64}$$

where σ_i is the SD of the i-th data with available uncertainty. The metric tolerance is recommended as $\bar{d}_{NE} \leq 2$.

When both the independent experimental and simulation data have uncertainties, the average of the Kullback-Leibler divergence metric, $\bar{D}_{KL}$, can describe the average of the information lost per point when the simulation data estimates the experimental measurements, provided that they both are normal distribution functions [156].

$$\bar{D}_{KL} = \left(\sum_{i}^{N} D_{KL}(D_i||P_i) \right) /N, \tag{2.65}$$

where

$$D_{KL}(D_i||P_i) = \frac{1}{2} \left[\left(\frac{\sigma_{D,i}}{\sigma_{P,i}} \right)^2 + \left(\frac{P_i - D_i}{\sigma_{P,i}} \right)^2 - 1 + 2\, ln \left(\frac{\sigma_{P,i}}{\sigma_{D,i}} \right) \right]. \tag{2.66}$$

Moreover, the average of the symmetrized Kullback-Leibler divergence metric, $\bar{S}_{KL}$, can be calculated by:

$$\bar{S}_{KL} = \left(\sum_{i}^{N} D_{KL}(D_i||P_i) + \sum_{i}^{N} D_{KL}(P_i||D_i) \right) /N, \tag{2.67}$$

where the reliable validation tolerance is $\bar{S}_{KL} < 1$. The average Hellinger metric, H_{ave}, also estimates the difference between two probability distributions [162].

$$H_{ave} = \sqrt{1 - \frac{1}{N} \sum_{i=1}^{N} h_i}, \tag{2.68}$$

where $h_i = \sqrt{\frac{2\sigma_{P,i}\sigma_{D,i}}{\sigma_{P,i}^2 + \sigma_{D,i}^2}}\ \exp\left(-\frac{1}{4} \frac{(P_i - D_i)^2}{\sigma_{P,i}^2 + \sigma_{D,i}^2} \right)$. Alternatively, the average Kolmogorov-Smirnov distance metric, $\bar{d}_{KS}$, calculates the difference between two cumulative distributions [163].

$$\bar{d}_{KS} = \frac{1}{N} \sum_{i=1}^{N} \left[\sup_{-\infty<x<\infty} \frac{1}{2} \left| erf\left(\frac{x - P_i}{\sqrt{2}\sigma_{P,i}} \right) - erf\left(\frac{x - D_i}{\sqrt{2}\sigma_{D,i}} \right) \right| \right], \tag{2.69}$$

where erf is the error function. Finally, the average normalized area metric, $\bar{d}_{area}$, proposed by [164] accounts for both horizontal and vertical differences between cumulative distributions.

$$\bar{d}_{area} = \frac{1}{N} \sum_{i=1}^{N} \left[\int_{-\infty}^{\infty} \frac{1}{2} |erf\left(\frac{x - P_i}{\sqrt{2}\sigma_{P,i}} \right) - erf\left(\frac{x - D_i}{\sqrt{2}\sigma_{D,i}} \right) |dx\ /D_i \right]. \tag{2.70}$$

Table 2.15 summarizes the corresponding validation metrics, tolerance ranges, and data types.

2.13 Pebble Bed Reconstruction

The reconstruction of the pebble bed facility is essential to create the geometry and corresponding mesh to run numerical simulations. Lin et al. reconstruct the 3D thorium-based molten salt reactor with graphite-matrix coated pebbles by utilizing the refractive index matched scanning (RIMS) technique [165]. Pieritz et al. use the x-ray microtomography, which allows the 3D helium-cooled pebble bed reconstruction with high spatial resolution [166]. Dijksman et al. also apply the RIMS tool to detect soft particles, hydrogels [167].

Similar to [168], the PIV images are used to reconstruct the TAMU isothermal pebble bed experiments,

Table 2.15. Summary of validation metrics. Adapted from [156].

Validation metric	Tolerance	Data type
RMSE/RMSRE/RRMSE	-	Deterministic
Minkowski distance (Average relative difference & average Euclidean distance)	-	Deterministic
Average of the total normalized Euclidean distance	$\bar{d}_{NE} \leq 2$	Deterministic & probabilistic
Average Kullback-Leibler divergence	$\bar{D}_{KL} < 0.5$	Probabilistic
Average of the symmetrized Kullback-Leibler divergence	$\bar{S}_{KL} < 1$	Probabilistic
Average Hellinger metric	-	Probabilistic
Average Kolmogorov-Smirnov	-	Probabilistic
Average normalized area metric	-	Probabilistic

which are designed to predict the pressure drop and velocity profiles in the pebble bed region. Pre-processing of the PIV images with the high-pass filter retains the particle image intensity by removing the noises from impurities in the fluid or the undesired laser light reflections. This is for accurately predicting the velocity profiles in the PIV window. However, for pebble bed reconstruction, a slight index mismatch at pebble boundaries (causing the refraction) allows to detect the edges of pebbles [167].

First, the pebble bed experiments are reconstructed with the time-resolved particle image velocimetry (TR-PIV) technology by MATLAB R2021a and VGSTUDIO MAX 3.4. The average bed porosities of the reconstructed pebble bed geometries are suitably estimated in lieu of applying the porosity correlations. The sensitivity analysis of the radial porosity with respect to the porous bed volume is described, including the development of a new radial porosity correlation.

2.14 Non-Dimensionalization of Navier-Stokes Equations

Identifying the dimensionless numbers is necessary to carry out the similarity-based scaling method. The incompressible Navier-Stokes equations including the Darcy (linear) and Forchheimer (non-linear) drag terms are shown as [169, 170]:

$$\rho_f \left[\frac{\partial u}{\partial t} + \nabla(u \cdot u)\right] = -\nabla P + \mu\nabla^2 u + \rho_f g - \frac{\mu}{K}u_s - \frac{c_F \rho_f}{K^{1/2}}|u_s|u_s, \tag{2.71}$$

where c_F is a dimensionless form-drag constant defined as:

$$c_F = BA^{-1/2}\varepsilon^{-3/2}, \text{ and} \tag{2.72}$$

A and B are the shape factors determined empirically. They are utilized to calculate the pressure drop across the porous media:

$$\frac{\Delta P}{H} = \frac{A\mu(1-\varepsilon)^2}{d_p^2\varepsilon^3}u_s + \frac{B\rho_f(1-\varepsilon)}{d_p\varepsilon^3}u_s^2. \tag{2.73}$$

Based on Equation 2.73, the permeability, K, in Equation 2.71 is:

$$K = \frac{d_p^2\varepsilon^3}{A(1-\varepsilon)^2}. \tag{2.74}$$

Under natural convection, the fluid motion is driven by the buoyancy force. The non-dimensionalization of Equation 2.75 results in Equation 2.76.

$$\rho_f \nabla(u \cdot u) = \mu\nabla^2 u + \rho_f g\beta(T_f - T_b) - \frac{\mu}{K}u_s - \frac{c_F\rho_f}{K^{1/2}}|u_s|u_s, \text{ and} \tag{2.75}$$

$$\begin{aligned}\nabla^*(u^* \cdot u^*) \; = & \left[\frac{\mu}{\rho_f u_s d_p}\right]\nabla^{*2}u^* + \left[\frac{g\beta(T_{suf} - T_b)d_p^3}{\nu^2}\right]\frac{T_f^*}{Re_p^2} \\ & - \left[\frac{\mu d_p}{u_s\rho_f K}\right]u_s^* - \left[\frac{c_F d_p}{K^{1/2}}\right]|u_s^*|u_s^*,\end{aligned} \tag{2.76}$$

where $u^* = u/u_s$, $\nabla^* = d_p\nabla$, $u_s^* = u_s/u_s$, and $T_f^* = (T_f - T_b)/(T_{suf} - T_b)$. The inverse of the particle Re, Gr, and the modified Darcy and Forchheimer resistance coefficients are shown in Equation 2.76.

For forced convection, the non-dimensionalized Navier-Stokes equations are described as [171]:

$$\begin{aligned}\left[\frac{f' d_p}{u_s}\right]\frac{\partial u^*}{\partial t^*} + \nabla^*(u^* \cdot u^*) \; = & -\nabla^* P^* + \left[\frac{\mu}{\rho_f u_s d_p}\right]\nabla^{*2}u^* + \left[\frac{g d_p}{u_s^2}\right]g^* \\ & - \left[\frac{\mu d_p}{u_s\rho_f K}\right]u_s^* - \left[\frac{c_F d_p}{K^{1/2}}\right]|u_s^*|u_s^*,\end{aligned} \tag{2.77}$$

where $t^* = t/(d_p/u_s)$, $P^* = P/\rho_f u_s^2$, $g^* = g/g$, and $f' = u_s/d_p$. Equation 2.77 shows the St, inverse of particle Re, inverse of the squared Fr, and the modified Darcy/Forchheimer resistance coefficients in order. The St is neglected at the steady state.

2.15 Non-Dimensionalization of Energy Equations

The non-dimensionalization of energy equations derives the dimensionless groups, and the fluid energy conservation equation becomes:

$$\begin{aligned}\varepsilon u^* \cdot \nabla^* T_f^* - \varepsilon \frac{g d_p}{C_{p,f}(T_{suf} - T_b)} g^* u^* - \frac{\kappa_f}{\mu C_{p,f}} \frac{\mu}{\rho_f u_s d_p} \nabla^{*2} T_f^* \\ + \frac{\alpha d_p}{\rho_f C_{p,f} u_s}(T_f^* - T_s^*) - \frac{q_t^{'''} d_p}{\rho_f C_{p,f} u_s (T_{suf} - T_b)} q_f^{*'''} = 0,\end{aligned} \tag{2.78}$$

where $q_f^{*'''} = q_f^{'''}/q_t^{'''}$, and $T_s^* = (T_s - T_b)/(T_{suf} - T_b)$. The Ec/Fr^2, inverse of the Pe, St, and the dimensionless group for the heat production are present in Equation 2.78. The solid energy equation at the steady state is described as follows:

$$-\nabla^{*2} T_s^* + \frac{\alpha d_p^2}{\kappa_s}(T_s^* - T_f^*) - \frac{d_p^2 q_t^{'''}}{\kappa_s (T_{suf} - T_b)} q_s^{*'''} = 0, \tag{2.79}$$

where $q_s^{*'''} = q_s^{'''}/q_t^{'''}$. The modified Bi and dimensionless group for the heat production are shown in Equation 2.79.

2.16 Dimensionless Similarity-Based Scaling Method

The dimensionless similarity-based scaling method from [171–173] is applied for building the heated pebble bed test facility, and similar approaches are adopted for other experimental facilities from [174–178]. The dynamic similarity of the fluid flow behavior between the full-scale PBR and scaled-down experimental facility is achieved by maintaining the ratio of the dimensionless numbers to be unity in Equation 2.80 [172].

$$\Psi_R = \frac{\Psi_m}{\Psi_p} = 1, \tag{2.80}$$

where Ψ is the dimensionless number, and the subscripts R, m, and p represent the ratio, model, and prototype, respectively.

The scaling study is conducted to describe the temperature change, fluid motion, and pressure drop in the PBR core. Specifically, for the loss of forced circulation (LOFC) accident scenarios, the Gr and Ri are observed in Equation 2.81 and Equation 2.82 [172]:

$$Gr_R = \frac{Gr_m}{Gr_p} = \left(\frac{g\beta\Delta T L^3}{\nu^2}\right)_m \left(\frac{g\beta\Delta T L^3}{\nu^2}\right)_p^{-1} = \frac{(\beta\Delta T)_m}{(\beta\Delta T)_p} \frac{\left(gL^3/\nu^2\right)_m}{\left(gL^3/\nu^2\right)_p}, \text{ and} \tag{2.81}$$

$$Ri_R = \frac{Ri_m}{Ri_p} = \left(\frac{g\beta\Delta T L}{U^2}\right)_m \left(\frac{g\beta\Delta T L}{U^2}\right)_p^{-1} = \frac{(\beta\Delta T)_m}{(\beta\Delta T)_p} \frac{\left(gL/U^2\right)_m}{\left(gL/U^2\right)_p}. \tag{2.82}$$

By having the first part of Gr_R or Ri_R to be unity and satisfying the ideal gas law $\left(\beta = T_f^{-1}\right)$, Equation 2.83 is obtained as:

$$\frac{\beta_m}{\beta_p} = \frac{\Delta T_p}{\Delta T_m} = \frac{(T_f)_p}{(T_f)_m}. \tag{2.83}$$

By setting the second part of the Gr similarity condition equal to one, Equation 2.84 is described as:

$$\left(\frac{L_m}{L_p}\right)^{3/2} = \frac{\nu_m}{\nu_p}. \tag{2.84}$$

The viscosity and density equations (Equation 2.85 and Equation 2.86) for the ideal gas are substituted into Equation 2.84 to observe the pressure relation between the prototype and model in Equation 2.87 [172].

$$\mu = \mu_o \left(\frac{T_f}{T_{f,o}}\right)^{0.5}, \text{ and} \tag{2.85}$$

$$\rho_f = \rho_{f,o} \frac{P}{P_o} \frac{T_{f,o}}{T_f}, \tag{2.86}$$

where the subscript o describes the reference quantity. Assuming that helium is used for cooling the pebble bed experiments, and the reference fluid material property, reference pressure, and reference temperature are the same for both the prototype and model,

$$\frac{P_m}{P_p} = \left(\frac{(T_f)_m}{(T_f)_p}\right)^{3/2} \left(\frac{L_p}{L_m}\right)^{3/2}, \text{ and} \tag{2.87}$$

$$\frac{(T_f)_m}{(T_f)_p} = \frac{\Delta T_m}{\Delta T_p} = \left[\frac{P_m}{P_p}\left(\frac{L_m}{L_p}\right)^{3/2}\right]^{2/3} = \left(\frac{P_m}{P_p}\right)^{2/3} L_R. \tag{2.88}$$

Next, the Ri similarity relationship is obtained by:

$$\frac{U_m}{U_p} = \sqrt{\frac{L_m}{L_p}} = \sqrt{L_R}. \tag{2.89}$$

The Fr similarity condition brings the similar influence of the gravity on fluid motion, and it is satisfied by having the Ri similarity [173, 176]:

$$Fr_R = \frac{Fr_m}{Fr_p} = \frac{U_R^2}{L_R} = 1. \tag{2.90}$$

The modified Darcy resistance coefficient similarity also concludes Equation 2.84 by applying $\frac{K_m}{K_p} = L_R^2$ from the modified Forchheimer resistance coefficient similarity and $\frac{U_m}{U_p} = \sqrt{\frac{L_m}{L_p}}$ from the Ri or Fr similarity.

$$\frac{L_m \nu_m}{U_m K_m} / \frac{L_p \nu_p}{U_p K_p} = 1, \text{ and} \tag{2.91}$$

$$\frac{\nu_m}{\nu_p} = \frac{L_p}{L_m} \frac{K_m}{K_p} \frac{U_m}{U_p} = L_R^{3/2}. \tag{2.92}$$

During normal reactor operation, the temperature rise in the PBR model core is calculated by Equation 2.88. By having similar Reynolds numbers given the ideal gas properties [172], the characteristic velocity scaling ratio would vary depending on the geometric, temperature, and pressure scaling ratios.

$$\frac{U_m L_m}{U_p L_p} = \frac{\nu_m}{\nu_p}, \text{ and} \tag{2.93}$$

$$\frac{U_m}{U_p} = \frac{L_p}{L_m} \left(\frac{(T_f)_m}{(T_f)_p} \right)^{3/2} \frac{P_p}{P_m} = \frac{1}{L_R} \left(\frac{(T_f)_m}{(T_f)_p} \right)^{3/2} \frac{P_p}{P_m}. \tag{2.94}$$

2.16.1 Pressure Drop Scaling Ratio

The pressure drop scaling ratio is determined by considering a few pressure drop correlations developed for porous media. The following pressure drop functions are valid for the relatively high Re regime, which the prototype HTR-PM fluid occurs at ($Re^* \simeq$ 5.2E4); the KTA [96], Jones and Krier [70], Carman [71], Tallmadge [72], Hicks [73], Wentz Jr and Thodos [98], and Lee and Ogawa [102] expect the same pressure drop scaling ratio of 1:27.51. The pressure drop correlations developed by accounting for the near-wall effects or tortuosity are valid only for lower Re ranges compared to the Re given for the prototype.

$$\text{KTA: } \Delta P_R = \left[\frac{160}{Re^*} + \frac{3}{(Re^*)^{0.1}} \right]_R \left[\frac{(1-\varepsilon)}{\varepsilon^3 d_p} \rho_f u_s^2 H \right]_R. \tag{2.95}$$

$$\text{Jones and Krier: } \Delta P_R = \left[\frac{150}{Re^*} + \frac{3.89}{(Re^*)^{0.13}} \right]_R \left[\frac{(1-\varepsilon)}{\varepsilon^3 d_p} \rho_f u_s^2 H \right]_R. \tag{2.96}$$

$$\text{Carman: } \Delta P_R = \left[\frac{180}{Re^*} + \frac{2.871}{(Re^*)^{0.1}} \right]_R \left[\frac{(1-\varepsilon)}{\varepsilon^3 d_p} \rho_f u_s^2 H \right]_R. \tag{2.97}$$

$$\text{Tallmadge: } \Delta P_R = \left[\frac{150}{Re^*} + \frac{4.2}{(Re^*)^{1/6}} \right]_R \left[\frac{(1-\varepsilon)}{\varepsilon^3 d_p} \rho_f u_s^2 H \right]_R. \tag{2.98}$$

$$\text{Hicks: } \Delta P_R = \left[\frac{6.8}{Re^{*0.2}} \right]_R \left[\frac{(1-\varepsilon)}{\varepsilon^3 d_p} \rho_f u_s^2 H \right]_R. \tag{2.99}$$

$$\text{Wentz Jr and Thodos: } \Delta P_R = \left[\frac{0.351}{(Re^*)^{0.05}-1.2}\right]_R \left[\frac{(1-\varepsilon)}{\varepsilon^3 d_p}\rho_f u_s^2 H\right]_R. \tag{2.100}$$

$$\begin{aligned}\text{Lee and Ogawa: } \Delta P_R = &\left[\frac{29.32}{Re_p}+1.56Re_p^{-n'}+0.1\right]_R \\ &\times\left[\frac{12.5}{2}\frac{(1-\varepsilon)^2}{\varepsilon^3 d_p}\rho_f u_s^2 H\right]_R.\end{aligned} \tag{2.101}$$

where $n' = 0.352 + 0.1\varepsilon + 0.275\varepsilon^2$.

2.16.2 Radial Heat Transfer

Understanding how the heat would be transferred radially through the PBR core is critical to preventing fuel failure [171]. By overheating, the reactor core temperature may exceed the safety limit and cause a nuclear core meltdown. These events can possibly release fission products into the coolant and potentially to outside the reactor housing at which point the public can be exposed.

For both the LOFC accidents and normal operation, the scaling ratio of the fluid specific heat varies depending on the pressure scaling ratio given the Ec similarity is satisfied. However, the SD of the specific heat for helium is less than 1% of 5,195 J/(kg·K) at the operating conditions for both the prototype and model [31]. Therefore, the specific heat scaling ratio is assumed as one, and different pressure operating conditions are proposed for the prototype and model accordingly. The scaling ratio of the effective fluid thermal conductivity depends on the fluid dynamic viscosity by using the Pr similarity.

$$\frac{(\kappa_f)_m}{(\kappa_f)_p} = \frac{\mu_m}{\mu_p}. \tag{2.102}$$

The St similarity relation describes the solid-fluid convective heat transfer coefficient scaling ratio as:

$$\frac{\alpha_m}{\alpha_p} = \frac{1}{\sqrt{L_R}}\frac{(\rho_f)_m}{(\rho_f)_p}. \tag{2.103}$$

Moreover, the dimensionless group for the heat production (derived from the fluid energy equation) gives:

$$\frac{(q_t^{'''})_m}{(q_t^{'''})_p} = \frac{1}{\sqrt{L_R}}\frac{(\rho_f)_m}{(\rho_f)_p}\frac{\Delta T_m}{\Delta T_p} = \sqrt{L_R}\frac{(\rho_f)_m}{(\rho_f)_p}\left(\frac{P_m}{P_p}\right)^{2/3}. \tag{2.104}$$

The modified Bi from Equation 2.79 provides the relation as:

$$\frac{\alpha_m}{\alpha_p}\frac{(\kappa_s)_p}{(\kappa_s)_m} = \frac{1}{L_R^2}. \tag{2.105}$$

The dimensionless group for the heat production (derived from the solid energy equation) provides:

$$\frac{(q_t''')_m}{(q_t''')_p}\frac{(\kappa_s)_p}{(\kappa_s)_m} = \frac{1}{L_R^2}\frac{\Delta T_m}{\Delta T_p} = \frac{1}{L_R}\left(\frac{P_m}{P_p}\right)^{2/3}. \tag{2.106}$$

3. GEOMETRY/MESH SETUP WITH BOUNDARY CONDITIONS

3.1 SANA Experiments*

Modern Pronghorn equations are validated by modeling the natural convection in the SANA experiments. These experiments are engineering-scale tests for observing the thermal behaviors and heat removal characteristics of pebble bed HTGRs [26]. Among the SANA experiments, for this study, a test case with a short heating element and 0.06 m graphite pebbles is used. This experiment is performed to estimate the behavior of the gas flow in the upper plenum of HTGRs under air ingress conditions. Nitrogen is selected as the coolant instead of air to avoid graphite oxidation. The total power transferred into the system through the inner cylindrical wall is 5 kW. The 0.33 m tall plenum is located above the 0.66 m tall pebble bed, and the 0.5 m heating rod is located at the center of the bed.

For overall STAR-CCM+ test sets, multiple insulation layers with different thermal conductivities are provided for the bottom insulation. One relatively thicker insulation layer is added on the top, and the whole set is enclosed in a steel vessel, as shown in Figure 3.1. Table 3.1 describes the detailed geometry configuration of the SANA facility and specifies the experimental conditions.

The mesh specifications are different for STAR-CCM+, modern Pronghorn, and legacy Pronghorn. The mesh for the insulation and steel layers is explicitly defined in STAR-CCM+ while thermal resistance boundary conditions (BCs) are applied in Pronghorn models. A uniform structured quadrilateral mesh is used for Pronghorn models in Figure 3.2 (right). To have a smooth transition between the mesh size of the bed and the finer mesh of the steel layer (and help the convergence), a bias on the right side of the bed mesh is applied as shown in Figure 3.2 (left). The modern Pronghorn mesh is refined in a similar fashion to the STAR-CCM+ mesh by having comparable numbers of mesh elements in the porous bed region. The legacy Pronghorn uses a coarser mesh than the other two models because finer meshes can result in convergence issues.

*Adapted with permission from [11].

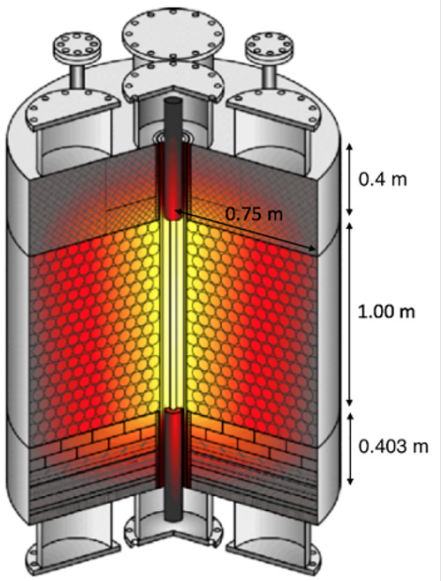

Figure 3.1. Schematic of the SANA facility. Reprinted from [26].

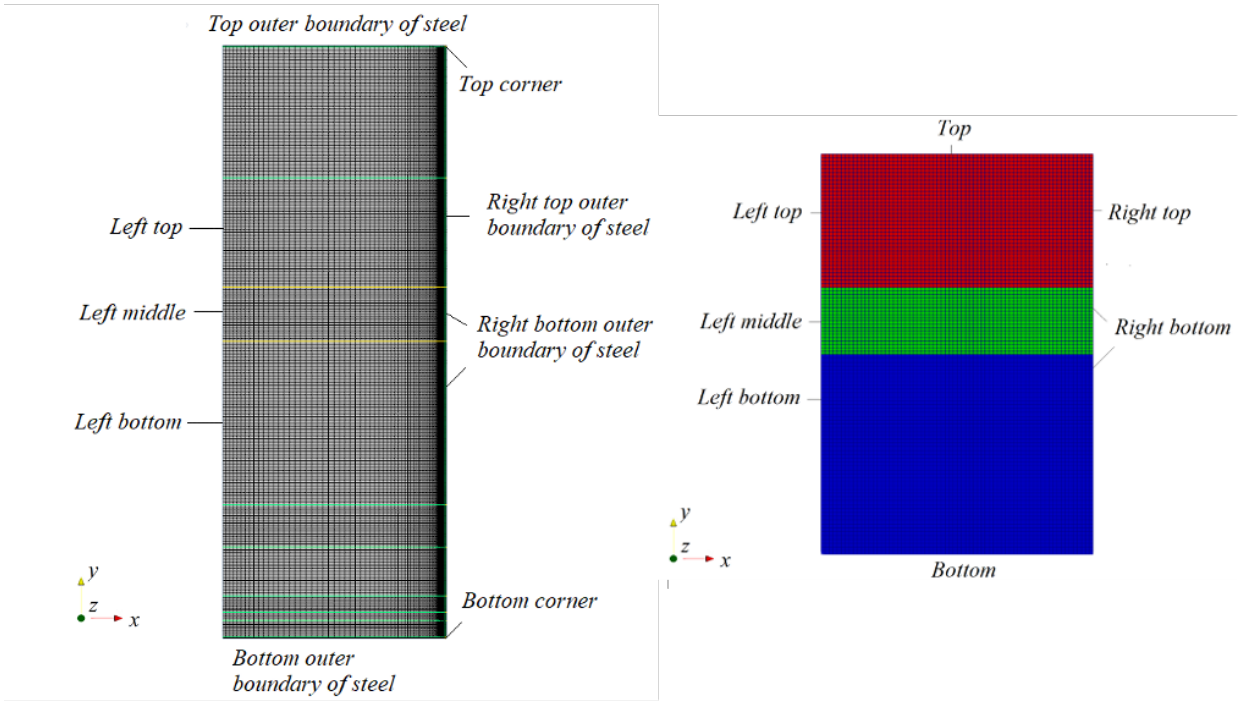

Figure 3.2. STAR-CCM+ (left) and modern Pronghorn (right) fine meshes. Adapted with permission from [11].

Table 3.1. Geometric configuration of the SANA facility and its experimental conditions. Adapted with permission from [11].

Geometric configuration/experimental condition	
Heating power (kW)	5
Height of the packed pebbles (m)	2/3
Length of the heating element (m)	0.5
Height of the top insulation (m)	0.4
Height of the pebble bed (m)	1
Height of the total bottom insulation layers (m)	0.403
Bottom insulation layer thickness (m)	0.128 (Fire light brick RI 30 B) 0.150 (CERAFORM 100, 1000) 0.050 (THERMOSIL 1100) 0.025 (THERMOSIL 1000) 0.050 (GOSSLEROC GMP 150)
Bottom insulation thermal conductivity (W/mK)	0.397 (Fire light brick RI 30 B) 0.074 (CERAFORM 100, 1000) 0.080 (THERMOSIL 1100) 0.041 (THERMOSIL 1000) 0.058 (GOSSLEROC GMP 150)
Inner radius of the pebble bed (m)	0.0705 (radius of the heating rod)
Outer radius of the pebble bed (m)	0.75
Pebble diameter (m)	0.06
Steel vessel thickness (m)	0.005
Steel thermal conductivity (W/mK)	17.0

The BCs used for Pronghorn models are summarized in Table 3.2. The heat flux, $\tilde{q}_{total}$, is imposed on the left bottom boundary (see Figure 3.2). It is split proportionally by the effective thermal conductivity and added into the fluid and solid energy equations:

$$\tilde{q}_f = \frac{\kappa_f}{\kappa_f + \kappa_s} \left(\tilde{q}_{total} \right), \text{ and} \tag{3.1}$$

$$\tilde{q}_s = \left(1 - \frac{\kappa_f}{\kappa_f + \kappa_s} \right) \left(\tilde{q}_{total} \right). \tag{3.2}$$

Thermal resistance BCs for the insulation and steel layers are utilized for Pronghorn models. They use nested, inner iterations to compute the fluid or solid temperature at the outer boundaries, which considers the conduction through the insulation or steel layers and the convective and radiative heat transfers to the environment. The convective heat transfer coefficient is 15 W/(m^2·K), and the steel emissivity is 0.8. The ambient temperature is different for each test run, and the detailed information is given in [26]. The corresponding thermal resistance boundaries are applied to the fluid temperatures on the top and right top boundaries of the bed, whereas the solid temperatures are used for the bottom and right bottom boundaries. Free slip BCs are applied to the fluid velocities on all boundaries.

STAR-CCM+ uses different BCs compared to Pronghorn (see Table 3.3). Thermal resistance BCs are not available in STAR-CCM+ such that the explicit meshing of insulation and steel layers is required. The phase-averaged temperature from the porous region is used for the conduction physics in outer layers. Then, the outer steel boundaries exposed to the environment account for the convective and radiative heat transfers, except for top and bottom corners (see Figure 3.2). The boundaries of top and bottom corners are set to be adiabatic. The heat flux through them is expected to be much smaller than the heat flux going through the outer radial boundary. Therefore, adiabatic BCs are expected to be adequate for comparison with Pronghorn. The fluid velocity BCs and the heat flux BC imposed on the left bottom boundary are identical to Pronghorn.

3.2 TAMU Isothermal Pebble Bed Experiments I*

The TAMU pebble bed test facility design is shown in Figure 3.3. The experiments estimate the behavior of the gas flow in the pebble bed, although they assume an isothermal condition. Two different pebble sizes provide the aspect ratios of 11 and 7.33 to observe the near-wall effects of PBRs. One compressible fluid (air) and one incompressible fluid (water) are used to measure the pressure drop within the designated porous bed heights. Table 3.4 describes the detailed geometric configuration of the TAMU pebble bed test facility and specifies the experimental conditions. Note that the same size of the pebble bed, a bed diameter of 0.1397 m, is used for both the compressible and incompressible cases. The experiments cover the flow range from the

*Adapted with permission from [12].

Table 3.2. Boundary conditions for Pronghorn models. Adapted with permission from [11].

Boundary condition	
Left bottom	Heat flux BC on T_f, T_s (split by the effective thermal conductivity), no penetration, weak boundary based on pressure
Left middle/left top	No penetration, weak boundary based on pressure
Right bottom/bottom	Thermal resistance BC on T_s, no penetration, weak boundary based on pressure
Right top/top	Thermal resistance BC on T_f, no penetration, weak boundary based on pressure

Table 3.3. Boundary conditions for STAR-CCM+. Adapted with permission from [11].

Boundary condition	
Left bottom	Heat flux BC on T_f, T_s (split by the effective thermal conductivity)
Left middle/left top/ outer boundaries of top and bottom corners	Adiabatic
Right bottom outer boundary of steel/ right top outer boundary of steel/ top outer boundary of steel/ bottom outer boundary of steel	Convection & radiation BC on T_{steel}[†]
Inner wall boundaries contacting the nitrogen gas	Slip condition

[†]T_{steel} is the temperature of the outer steel layer.

laminar to turbulent regime for validating the correlations. In other words, the particle Reynolds number varies from 55 to 678.

In Figure 3.4, for the axisymmetric model, the uniform mesh with 1,024 cells is used for the free flow region where only the pure fluid is provided, and 12,800 and 14,080 elements are used in the porous region

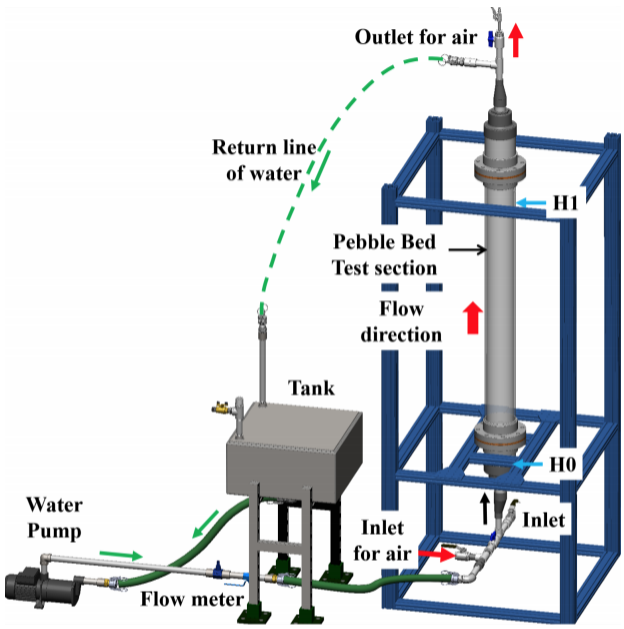

Figure 3.3. Schematic of the pebble bed test facility. Reprinted from [179].

Table 3.4. Geometric configuration of the TAMU pebble bed test facility and its experimental conditions. Reprinted with permission from [12].

Experimental Condition	
Working fluid	Air, water
Working fluid temperature (^{o}C)	21, 25
Material for the pebbles and cylindrical bed	Acrylic
Bed diameter (m)	0.1397
Pebble diameter (m)	0.0127, 0.01905
Bed height (m)	1.219, 1.2954
Aspect ratio (bed diameter/pebble diameter)	11, 7.33

with air and water. For the Pronghorn finite element (FE) cases, the Dirichlet boundary conditions are used for the inlet velocities. The implicit boundary condition (i.e., a boundary condition that uses the correct velocity specified for the momentum equation) for the advective term in the mass equation is also specified at both the inlet and outlet in FE simulations. In addition, the implicit boundary for the advection term in the momentum equation is determined at the outlet, and the outlet pressure is weakly imposed for the pressure term in the momentum equation. For the STAR-CCM+ and Pronghorn finite volume (FV) cases, the BCs

are the inlet velocity, outlet pressure, and free slip conditions on the walls. The initial conditions are the ambient temperature and pressure.

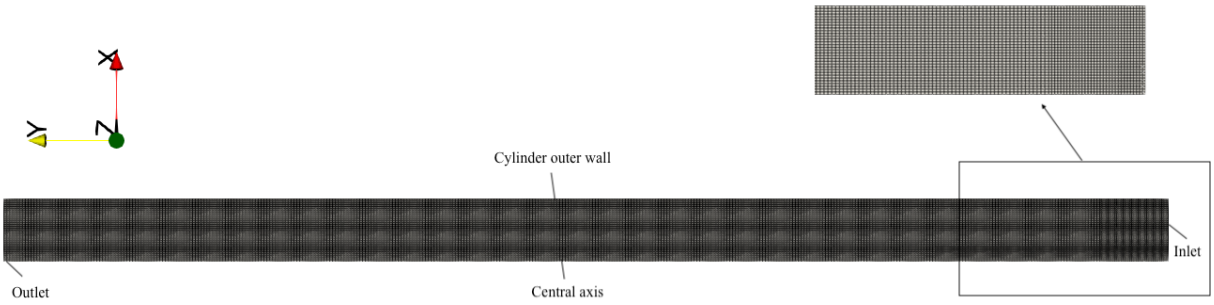

Figure 3.4. Geometry and fine mesh of the Pronghorn and STAR-CCM+ models (axisymmetric modeling). Adapted with permission from [12].

3.3 TAMU Isothermal Pebble Bed Experiments II

The recent isothermal pebble bed experiments are performed to estimate the pressure drop and velocity profiles in the pebble bed region. The schematics of the new pebble bed test facility are shown in Figure 3.5. Figure 3.5 (a) and (b) describe the main flow loop and matched index of refraction (MIR) test section with acrylic spheres [180]. The same bed diameter size and one pebble diameter, 0.01905 m, are obtained from Section 3.2. Consequently, the aspect ratio, D/d_p, is 7.33. A total of 1,350 spheres fill the bed to a height of 0.5461 m. The pressure drop measurements are made within 0.5334 m of the bed, and the average bed porosity of 0.4162 is calculated by:

$$\bar{\varepsilon} = \frac{V_{total} - V_{spheres}}{V_{total}}. \tag{3.3}$$

The experiments cover the turbulent flow regime by increasing the particle Reynolds number from 324 to 1,036. The working fluid is p-Cymene with $n = 1.49$. Figure 3.5 (c) shows a radial cross section of the experimental facility and the layout of the PIV measurement locations [180]. Figure 3.5 (d) represents the MIR test section partially filled with p-Cymene.

For the Pronghorn and STAR-CCM+ axisymmetric porous media models, a uniform mesh with 5,632 cells is used for the inlet flow region (pure fluid region), and 7,680 cells are used for the porous region in

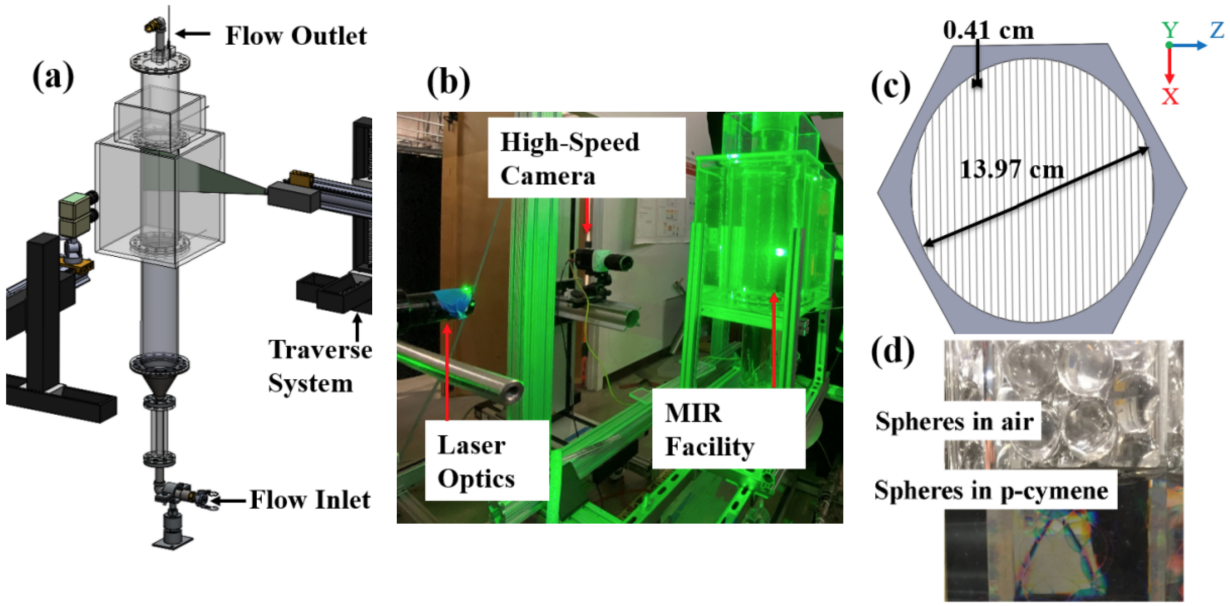

Figure 3.5. Overview of the MIR experimental facility. (a) Computer-aided design (CAD) rendering of the experimental facility during PIV measurements, (b) main flow loop, (c) facility radial cross section with PIV measurement locations, and (d) visualization of the MIR principle. Reprinted from [180].

Figure 3.6. Additionally, some STAR-CCM+ simulations include the turbulence quantities specified for the pebble bed region, and the SST $k-\omega$ model with all-y^+ wall treatment is applied for the inlet flow region with no slip condition. This ensures that the specification of the turbulence quantities does not add much of a discrepancy in the pressure drop and axial velocity in porous bed. Figure 3.7 describes the fine mesh of the 2D axisymmetric porous media models constructed with more refined mesh near walls for $y^+ < 1$. The 2.3E4 and 3E4 mesh cells are used for the inlet flow and porous regions, respectively. Given the Carman pressure drop correlation, the 3D porous media models are also verified to bring results similar to those from the 2D axisymmetric porous media models. Figure 3.8 indicates the geometry and fine mesh of the 3D porous media models. The 9E5 and 1.2E6 mesh cells are used for the inlet free flow region and pebble bed region, respectively. The structured patch mesh is generated at the pebble bed outlet, and it is extruded through the pebble bed and fluid regions. Similar to the 2D models, more refined mesh is also given near the walls for $y^+ < 1$.

The explicit meshing of the random packed beds generated by MATLAB and VGSTUDIO is performed for turbulence modeling. Figure 3.9 describes the axial cross sections of meshes of the VGSTUDIO random

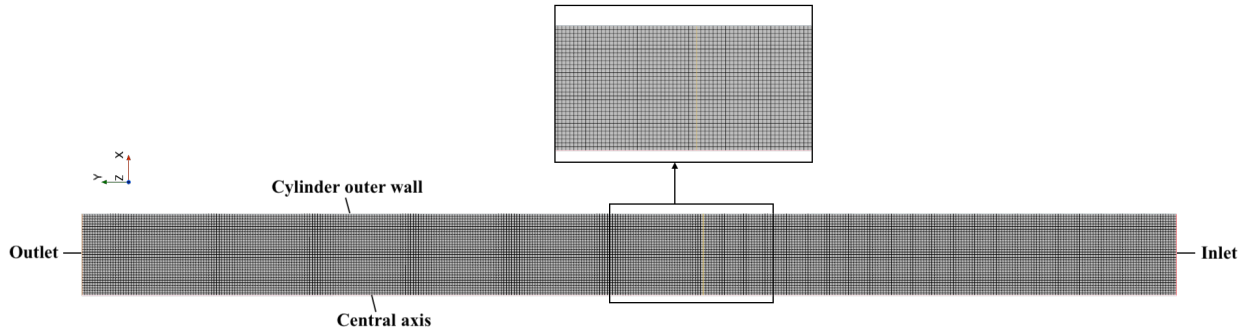

Figure 3.6. Geometry and fine mesh of the Pronghorn and STAR-CCM+ axisymmetric porous media models (TAMU isothermal pebble bed experiments II).

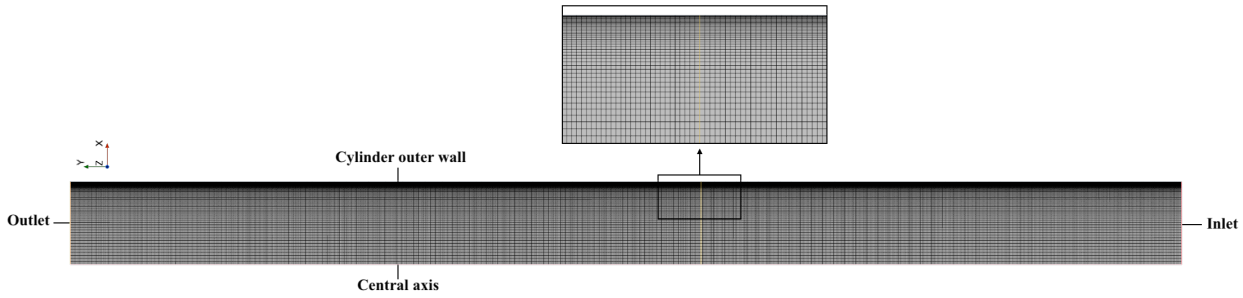

Figure 3.7. Geometry and fine mesh of the STAR-CCM+ axisymmetric porous media models with the turbulence quantities specified in the porous bed, including the SST $k-\omega$ turbulence model in the fluid region.

packed column within four different bed heights of the porous region. Figure 3.10 shows the close ups of the axial and radial cross sections of the VGSTUDIO mesh provided the $10d_p$ bed height. The inlet and outlet are located $2d_p$ away from the packed bed to avoid the reverse flow and the consequent convergence issues. The fluid flow enters the inlet, located $2d_p$ below the porous region, and the outlet is $2d_p$ above the porous region. This applies only for the $10d_p$ and $15d_p$ bed heights, while the CFD simulations with the d_p and $5d_p$ bed heights are executed with the $5d_p$ free flow region on top and bottom of the packed bed due to a lower computational cost. The polyhedral meshes with prism layers are applied with $y^+ < 5$. More details about the mesh characteristics for turbulence modeling are provided in Table 3.5. Similar meshing is performed for the MATLAB reconstructed geometry.

The identical boundary conditions for Pronghorn finite element method (FEM), Pronghorn finite volume

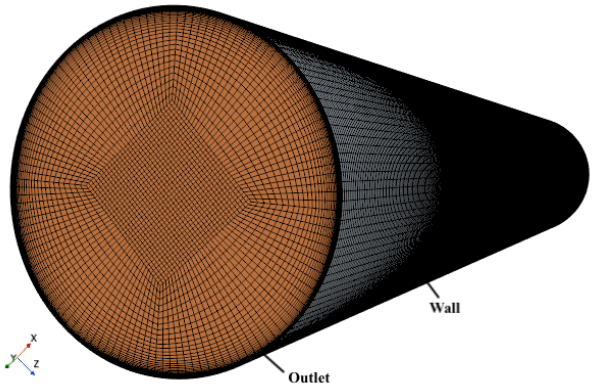

Figure 3.8. Geometry and fine mesh of the 3D STAR-CCM+ porous media models with the turbulence quantities specified in the porous bed, including the SST $k-\omega$ turbulence model in the fluid region.

Table 3.5. Mesh characteristics for the realizable two-layer $k-\varepsilon$ and SST $k-\omega$ turbulence models.

Specific porous bed height (m)	d_p	$5d_p$	$10d_p$	$15d_p$
Number of mesh cells	4.46E6	1.29E7	2.74E7	4.02E7
Base size (m)	0.002			
Number of prism layers	12			
Total thickness of prism layers (m)	6.67E-4			
Volume growth rate	1.0	1.2	1.0	1.0

method (FVM), and STAR-CCM+ axisymmetric porous media models in Section 3.2 are applied for the new pebble bed test facility. For both the axisymmetric and 3D STAR-CCM+ porous media simulations with the turbulence quantities specified in the porous bed, including the SST $k-\omega$ turbulence model in the fluid region, the initial/boundary conditions for the turbulence intensity and turbulent length scale are approximated as follows:

$$I = 0.16 Re_h^{-1/8}, \text{ and} \tag{3.4}$$

$$l = 0.07 D_h. \tag{3.5}$$

Turbulence modeling with explicit meshing of the fluid region around pebbles specifies the mass flow rates at both the inlet and outlet. The turbulence intensity and turbulent length scale at the inlet boundary

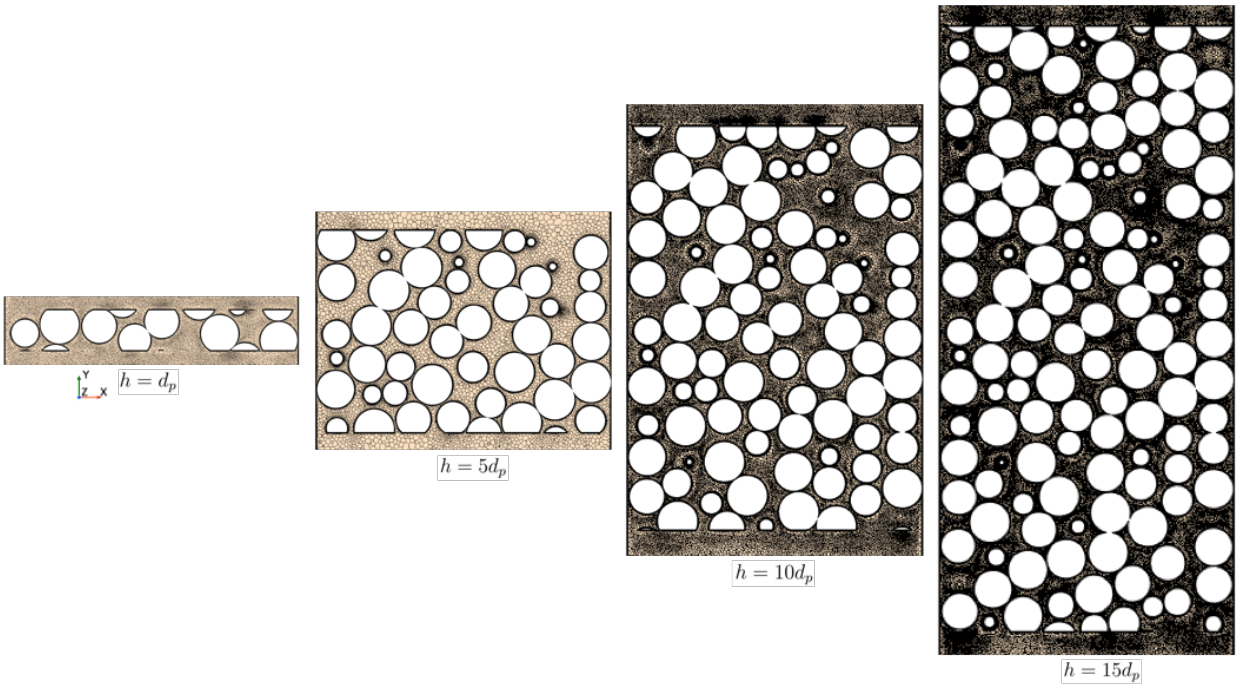

Figure 3.9. Axial cross sections of meshes of the random packed column constructed by VGSTUDIO for turbulence modeling. Four different heights of the porous region ($h = d_p, 5d_p, 10d_p$, and $15d_p$) are used to derive the velocity profile and pressure gradient.

are estimated based on the hydraulic diameter in the free flow region using Equation 3.4 and Equation 3.5. Note that the inlet is located a specific distance away from the porous bed. The initial conditions for the turbulence intensity and turbulent length scale are calculated based on the hydraulic diameter in the porous region since the quantities of interest, such as the pressure drop and volume- or surface-averaged axial velocity, are within the porous bed. Additionally, the no slip condition is applied for all walls.

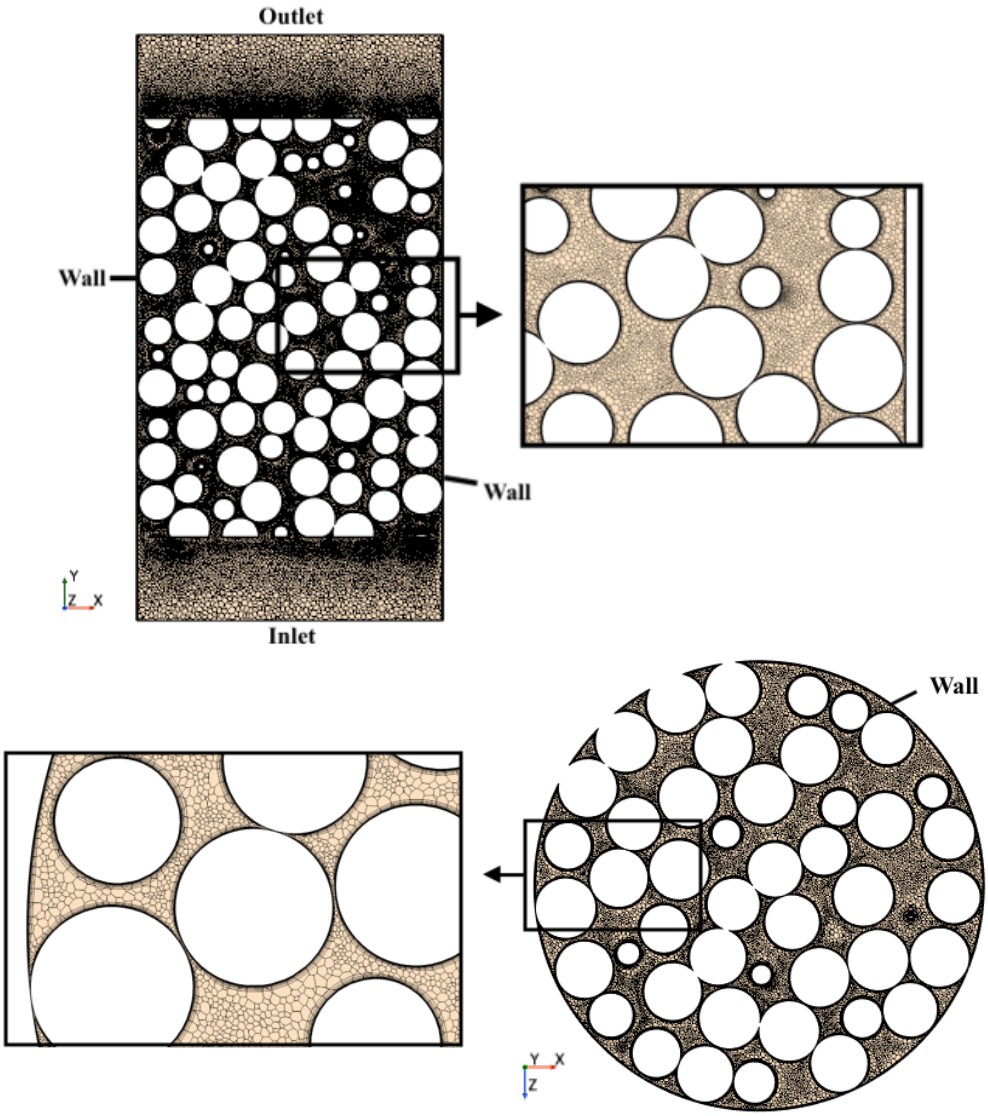

Figure 3.10. Axial and radial cross sections of the VGSTUDIO mesh given the $10d_p$ bed height.

4. SIMULATION SETTINGS/NUMERICAL METHODS*

4.1 SANA Experiments

Modern equations aim at improving on the fidelity of the fluid model by including the fluid advection and time derivative terms in the fluid momentum equations. The STAR-CCM+ v14.06.012 R-8 results are used to generate reference solutions for quantities that were not measured during the SANA experimental campaign (e.g., fluid temperature, pressure, and velocities). In addition, axisymmetric modeling accounts for the cylindrical shape of the SANA facility. This reduces the computational cost significantly for both Pronghorn and STAR-CCM+.

The KTA drag coefficients in Table 2.6 are used to simulate the isotropic pressure drop in the pebble bed since the SANA experiments satisfy its validity conditions. The solid-fluid convective heat transfer coefficient is calculated by Equation 2.8 in Section 2.7. Here, the Nu is estimated by the Petrovic and Thodos model, and the thermal dispersion is considered by calculating the effective fluid thermal conductivity by Equation 2.12. The Breitbach and Barthels correlation, the Zehner and Schlünder model, and the Chan and Tien model are built on the concept of a heat transfer in Section 2.8 and are used in this study.

Pronghorn uses the streamline upwind Petrov-Galerkin continuous finite element method (SUPG-CFEM) to discretize legacy and modern Pronghorn equations. The details of the weak form of compressible Euler equations implemented in modern Pronghorn are shown in [10]. The Newton's method is used to solve a system of coupled non-linear equations, and an implicit time advancement scheme with time step control is adopted by the models. On the other hand, STAR-CCM+ uses the FVM. Under the laminar flow condition, the pressure-implicit with splitting of operators (PISO) algorithm is used for an unsteady compressible flow. The time step is modified to satisfy the Courant-Friedrichs-Lewy (CFL) condition, ensuring stability. The second-order upwind scheme is used for convection. Both Pronghorn and STAR-CCM+ reach a steady state solution by running a pseudo-transient simulation.

4.2 TAMU Isothermal Pebble Bed Experiments I, II

Pronghorn with the FEM uses the SUPG method to discretize the Navier-Stokes equations. The details of the weak form of compressible Navier-Stokes equations in Pronghorn are provided in [10]. Similar to

*Adapted with permission from [11, 12].

the Pronghorn simulation settings for the SANA experiments in Section 4.1, the Newton's method is also used to solve the system of coupled non-linear equations, and Pronghorn furthermore reaches a steady state solution by running a pseudo-transient simulation. In addition, Pronghorn can also run FV simulations, and the preliminary pressure drop results are presented in this study. Here, the first-order upwind scheme is used for advection, and the fully coupled solver is used. The FVM is utilized by STAR-CCM+ v16.02.009, and it generates the reference solutions. The steady state solutions under the turbulent flow condition are obtained with the Darcy-Forchheimer model. The second-order upwind scheme is used for convection, and the segregated SIMPLE solver is used for an steady compressible/incompressible flow.

5. RESULTS AND DISCUSSION

5.1 SANA Experiments*

First, the mesh convergence test was performed to ensure that the results were spatially converged. Meshes with three different refinement levels were prepared to study the GCI and to evaluate the discretization error. The maximum solid temperature at the bed height of 0.5 m was utilized as the convergence test quantity, and it was predicted to be 688.01^{o}K for modern Pronghorn by using the RE. By satisfying that the ratio of $GCI_{32}/GCI_{21}r^p$ is $\sim$1, all solutions were in the asymptotic range of convergence, and the GCI was a valid estimator. The GCI for fine mesh was 4.78%; the fine mesh provided numerical results close to the asymptotic solutions with an error band of 4.78%. Similar processes were carried out for the STAR-CCM+ results. See Table 5.1 for further details on the mesh convergence study. In addition, legacy Pronghorn results were considered mesh independent because the difference in the maximum centerline solid temperature was about 0.23^{o}K between the medium and fine mesh results in Figure 5.1.

Table 5.1. Mesh convergence study results. Adapted with permission from [11].

Model	Modern Pronghorn	STAR-CCM+
Maximum solid temperature at bed height = 0.5 m (^{o}K)	688.01	677.22
GCI_{21} (%)	4.78	5.23
GCI_{32} (%)	5.61	7.81

The SANA benchmark does not report all quantities that are required for performing a full validation exercise. The initial fluid temperature (i.e., the temperature of the fluid before the heater is switched on) and pressure are not provided in the technical report, but this information is required to calculate the total fluid mass in the system. SANA is a closed system such that the initial mass does not change throughout the pseudo-transient simulation. Different fluid masses lead to significantly different fluid and solid temperatures. In this exercise, the initial fluid temperature of 419.7^{o}K was used to have a system pressure close

*Adapted with permission from [11].

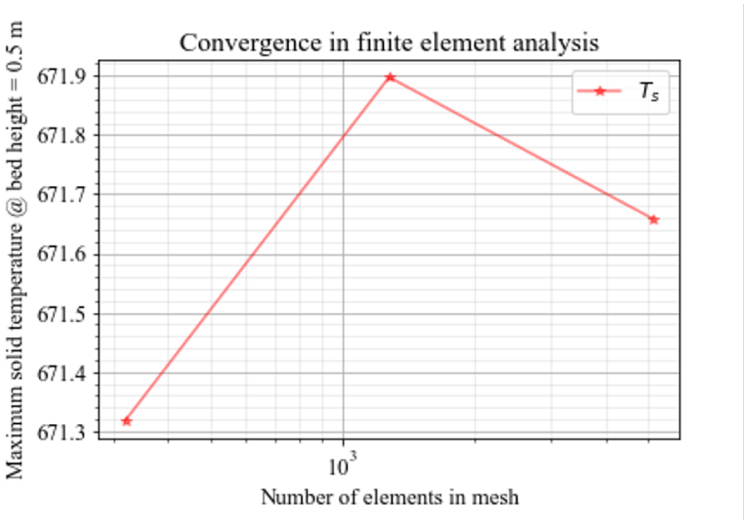

Figure 5.1. Convergence in FEM (legacy Pronghorn). Reprinted with permission from [11].

to the standard atmospheric pressure of 101,325 Pa for the modern Pronghorn fine mesh case at the convergence to steady state. The same initial fluid temperature and pressure were used for both Pronghorn and STAR-CCM+ to ensure that the same amount of nitrogen gas is used in all simulations.

In Figure 5.2, legacy Pronghorn, modern Pronghorn, and STAR-CCM+ overpredict the solid temperature at the bed height of 0.5 m except near the outer wall. Disagreement between the experiments and models is large near the heater rod, as previously pointed out in [21]. This discrepancy is at least partially caused by:

- Lack of information about the total amount of fluid in the system,
- Discrepancy between models and the as-built facility, and
- Measurement errors.

In addition, implementing more sophisticated correlations for capturing the near-wall physics may be necessary. The amount of heat provided to the porous region from the heating rod may also be split differently between two phases.

The Pronghorn (both legacy and modern) and STAR-CCM+ results agree exceptionally well with each other on fluid and solid temperatures (see Figure 5.2 and Figure 5.3). This leads to two conclusions: 1) the approximations inherent in the legacy formulations do not strongly affect the solutions in the bed, even in the presence of a plenum where these approximations are not appropriate; 2) the computational models are

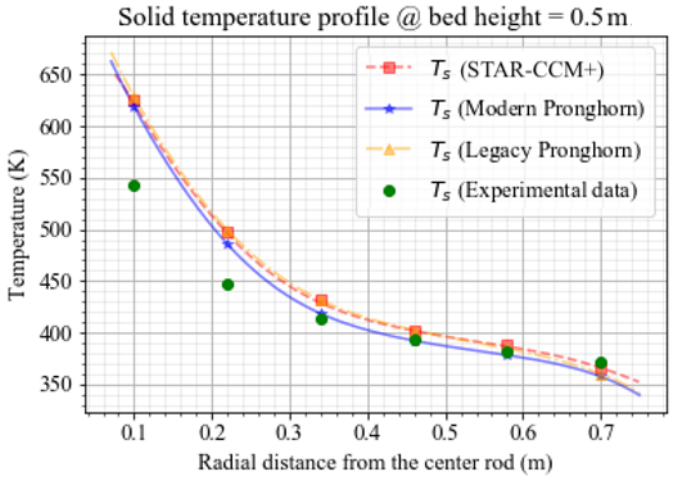

Figure 5.2. Solid temperature profile at the bed height of 0.5 m. Adapted with permission from [11].

consistent, and the remaining difference from the experimental results is common between all of them. In Figure 5.2, the simulated results are shown together with the SANA experimental data. Legacy Pronghorn, modern Pronghorn, and STAR-CCM+ have the 15.7%, 13.9%, and 15.3% maximum relative differences at $r = 0.1$ m near the heating rod. However, the 1.46% minimum relative difference is obtained at $r = 0.7$ m for STAR-CCM+ while 0.67% is obtained at $r = 0.58$ m, and 0.23% is obtained at $r = 0.46$ m, respectively, for legacy and modern Pronghorn. In Figure 5.3, the fluid temperature follows a similar trend as the solid temperature shown in Figure 5.2.

Modern Pronghorn and STAR-CCM+ estimate the solid temperature better than legacy Pronghorn in terms of the relative difference from the experimental data near the heating rod until the half bed height (see Figure 5.2, Figure 5.4, and Figure 5.5). Overall, the modern Pronghorn results are closer to the experimental results than other models at the half bed height (see Figure 5.2). In Figure 5.6, at $y = 0.63$ m of the bed, both Pronghorn models estimate the solid temperature better than STAR-CCM+, except at $r = 0.7$ m.

The velocity streamlines and fluid temperature color maps for legacy Pronghorn, modern Pronghorn, and STAR-CCM+ are shown in Figure 5.7. The nitrogen gas rises near the heat source, and it flows downward when reaching the outer wall of the experiment. At the bottom of the experiment, the gas flows inwardly towards the heater, and it flows outwardly towards the outer wall at the top of the reactor. The predicted flow pattern in the upper plenum is similar for modern Pronghorn and STAR-CCM+ but significantly dif-

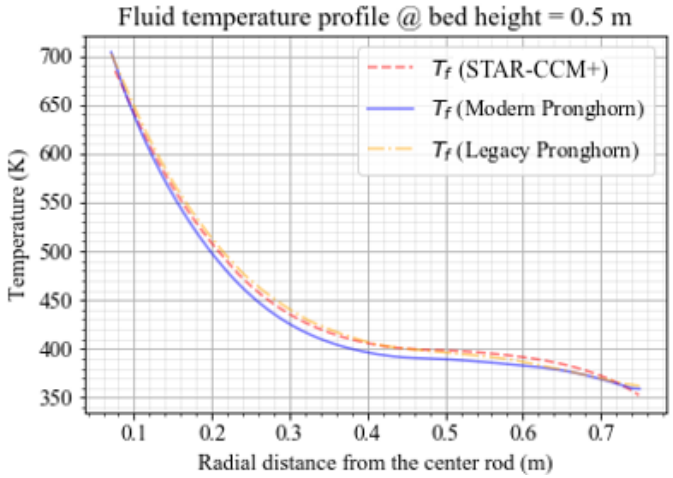

Figure 5.3. Fluid temperature profile at the bed height of 0.5 m. Adapted with permission from [11].

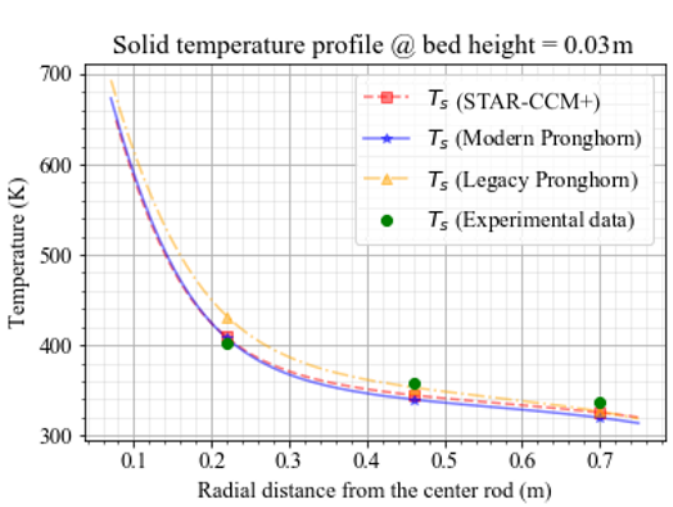

Figure 5.4. Solid temperature profile at the bed height of 0.03 m. Adapted with permission from [11].

ferent for legacy Pronghorn, confirming the unsuitability of legacy Pronghorn's approximations in the upper plenum. In the plenum, vortices are predicted by legacy Pronghorn, while no vortex is estimated by modern Pronghorn and STAR-CCM+. Nevertheless, fluid and solid temperatures in the bed are in good agreement across all three simulations. Therefore, for the SANA plenum experiment, the flow in the upper plenum has a negligible influence on temperatures in the bed.

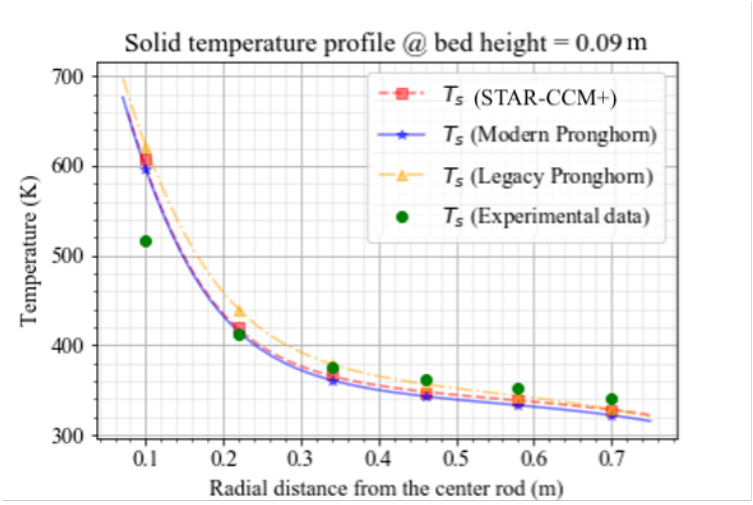

Figure 5.5. Solid temperature profile at the bed height of 0.09 m. Adapted with permission from [11].

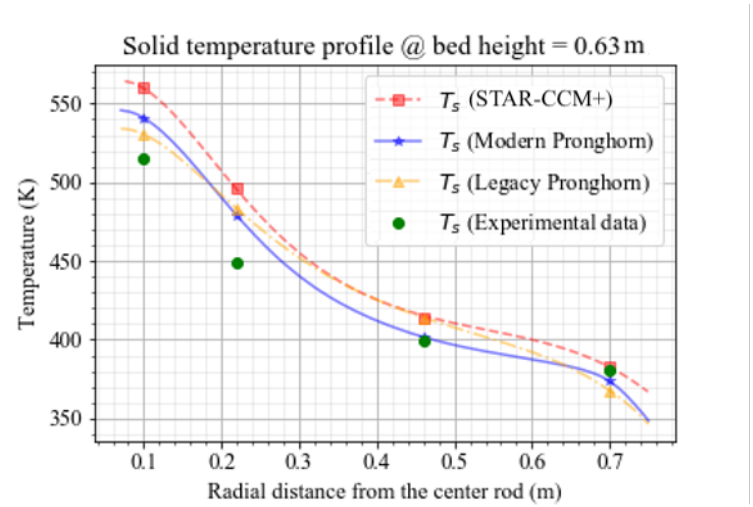

Figure 5.6. Solid temperature profile at the bed height of 0.63 m. Adapted with permission from [11].

5.2 TAMU Isothermal Pebble Bed Experiments I*

The average bed porosity of a random packed bed was estimated by twelve different average porosity correlations from [10]. Mueller, Sato, and Zou and Yu correlations were investigated because their experimental setups are similar to the TAMU isothermal experiments, and the parameters of the TAMU

*Adapted with permission from [12].

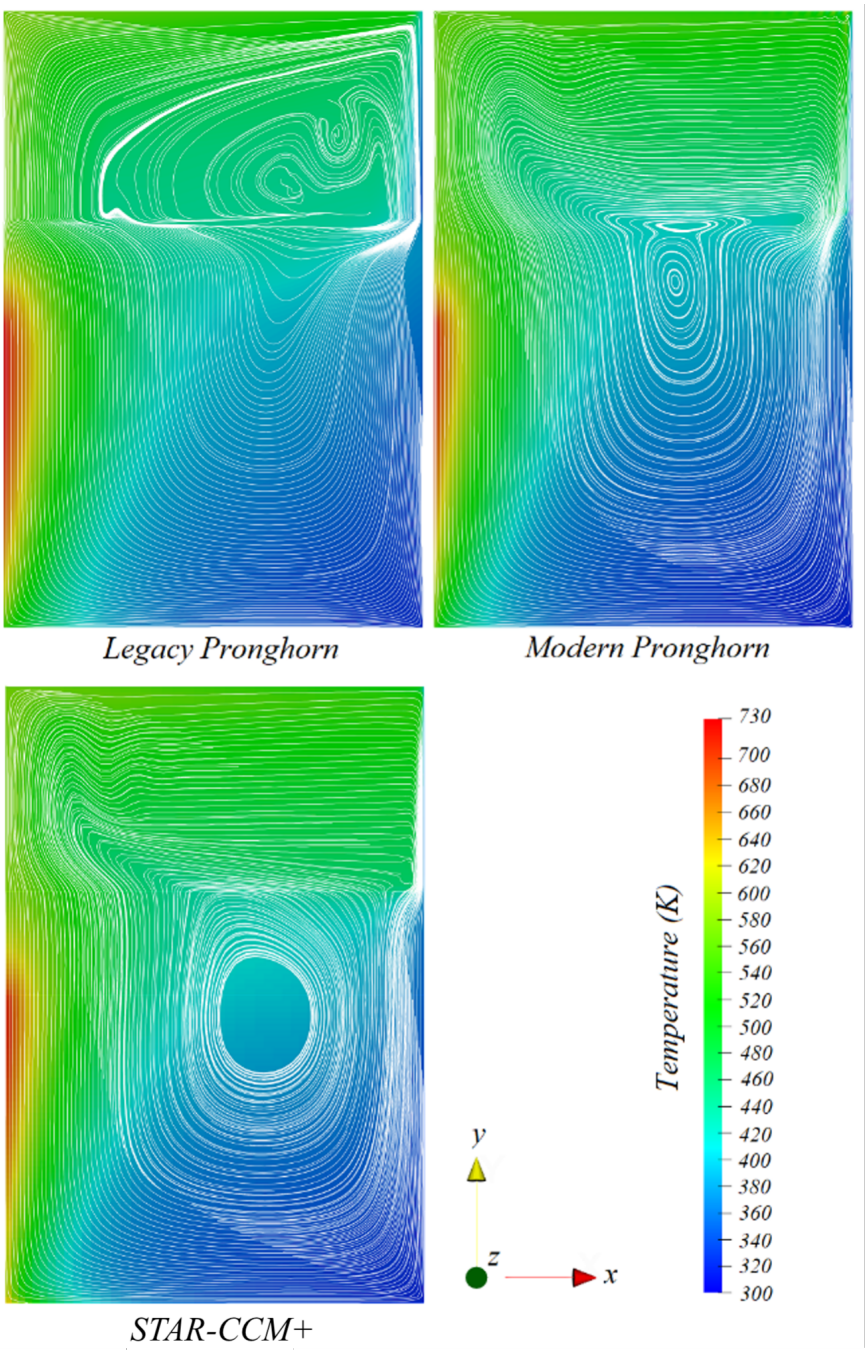

Figure 5.7. Velocity streamlines and fluid temperature profile. Adapted with permission from [11].

experiments fall within the correlations' validity conditions. These correlations were developed by the researchers with pebble and bed diameters similar to the current experiments, including the random packing method and the pebble material, such as acrylic glass. On the other hand, other correlations derived from

experiments different from the TAMU experiments were excluded. For instance, Beavers et al. [42] derived the correlation by using a rectangular bed, and Foumeny et al. [43] vibrated the cylinder for packing the pebbles. In Figure 5.8, red lines represent the aspect ratios of 11 and 7.33 used for the air and water cases, respectively. The uncertainty bands are provided for the Mueller and Sato correlations by propagating the SDs of the pebble diameter. The uncertainties were calculated by multiplying the SDs by 2 for the 95% confidence level given the normal distributions, and they are less than 1% of the average porosities at the corresponding aspect ratios of 11 and 7.33. Note that the Zou and Yu model is accounted for with both the loose and dense packing methods. The average porosities calculated by the above correlations vary within the porosity range by $\sim$0.05, which is relatively large compared to the values of the averages. This would likely provide the differences in pressure drop when the empirical pressure drop correlations are applied in the Darcy-Forchheimer model (see Table 5.2).

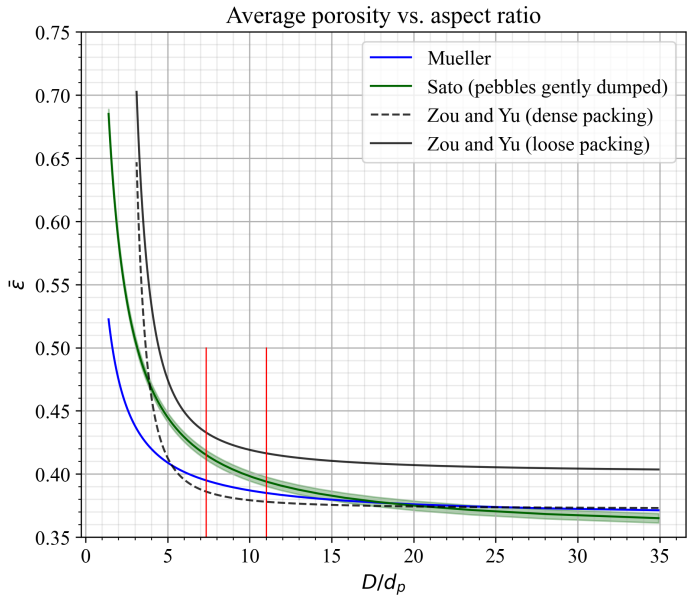

Figure 5.8. Comparison of average porosity correlations. Adapted with permission from [12].

The optimal porosity function was determined by examining the porosity functions in Table 5.2; these functions were used with the pressure drop correlations listed in Table 5.3 to produce Figure 5.9. As a

Table 5.2. Average porosities estimated by different correlations. Adapted with permission from [12].

Model/average porosity	$\bar{\varepsilon}$ (air)	$\bar{\varepsilon}$ (water)
Mueller	0.385	0.395
Sato (pebbles gently dumped)	0.394	0.4152
Zou and Yu (dense packing)	**0.378**	0.3861
Zou and Yu (loose packing)	0.4164	**0.4329**

result, the Zou and Yu average porosity function with dense packing estimated the pressure drop better than others, specifically for air cases. Given that both the experimental and correlation data are deterministic, the Zou and Yu model with dense packing has the lowest RMSEs, RRMSEs, and average Euclidean distances (commonly known as average L^2 norm) in pressure drop among the porosity functions in Table 5.2. The probabilistic experimental data led to the same conclusion such that the Zou and Yu dense packing model performed exceedingly well in predicting the pressure drop with the lowest averages of the total normalized Euclidean distance given the Eisfeld and Schnitzlein correlation and KTA correlation (see Table 5.3). On the other hand, in Figure 5.10, the Zou and Yu loose packing model approximated the pressure drop more appropriate than other models for the water cases with regard to the validation metrics in Table 5.4.

Table 5.3. Validation metrics for the Zou and Yu dense packing model (air). Adapted with permission from [12].

Validation metrics/model (1D correlation)	Ergun	Eisfeld and Schnitzlein	KTA
Average relative difference (%)	8.496	12.76	13.19
RMSE (Pa)	12.04	43.07	26.53
RRMSE (%)	5.488	19.63	12.09
Average L^2 norm (Pa)	34.06	121.8	75.04
Average of the total normalized Euclidean distance	2.966	4.56	4

The specification of turbulence quantities did not improve the pressure drop significantly. The turbulent quantities were specified for the pebble bed region for $Re_p = 274 \sim 365$ (see Figure 5.11 for the Foumeny

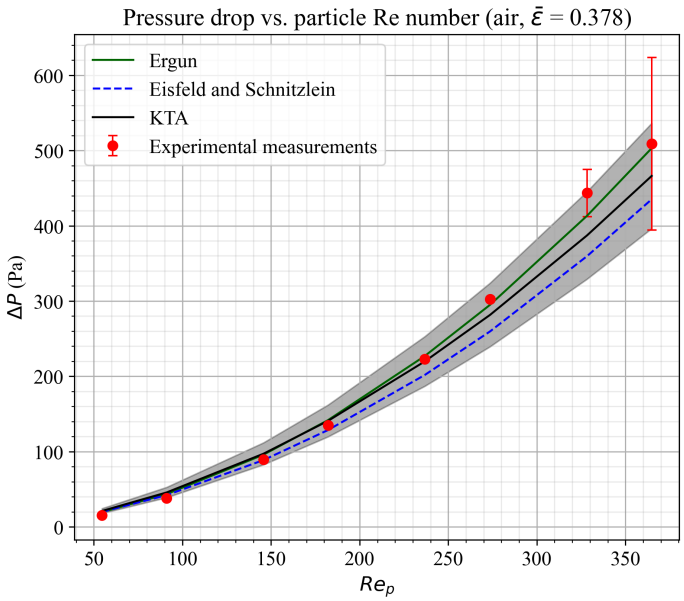

Figure 5.9. Pressure drop comparison with the Zou and Yu dense packing model (air). Reprinted with permission from [12].

Table 5.4. Validation metrics for the Zou and Yu loose packing model (water). Adapted with permission from [12].

Validation metrics/model (1D correlation)	Eisfeld and Schnitzlein	KTA
Average relative difference (%)	37.61	39.82
RMSE (Pa)	52.04	51.17
RRMSE (%)	18.89	18.58
Average L^2 norm (Pa)	194.7	191.5
Average of the total normalized Euclidean distance	0.7963	0.7833

function), and the SST $k-\omega$ model with all-y^+ wall treatment was used for the free flow region with no slip condition. Due to the insignificant pressure drop change by providing the turbulence quantities to the compressible Navier-Stokes equations with the Darcy-Forchheimer model, the axisymmetric porous media simulations were performed without the turbulence properties for the whole Re range for both Pronghorn and STAR-CCM+.

After determining the average porosity, the pressure drop correlations valid in the specific Re and aspect ratio ranges were implemented in both Pronghorn and STAR-CCM+ to estimate the pressure drop in the

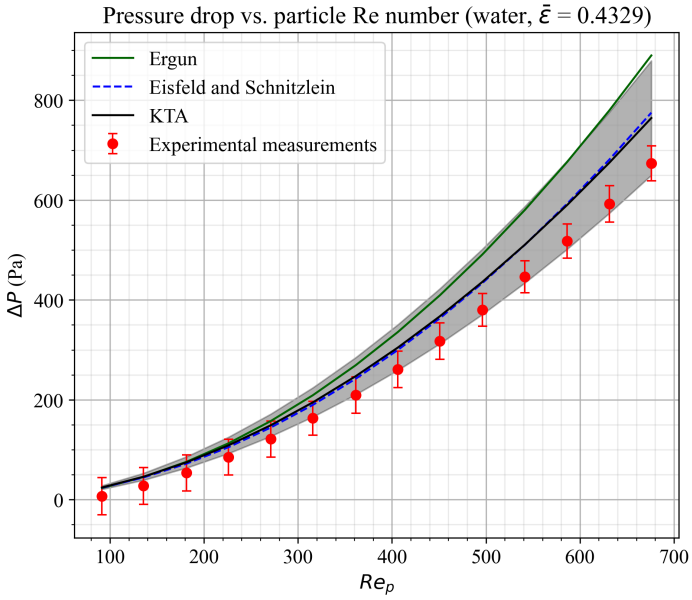

Figure 5.10. Pressure drop comparison with the Zou and Yu loose packing model (water). Reprinted with permission from [12].

pebble bed. Generally, the GCIs for fine meshes were less than 1% with the lowest and highest particle Reynolds numbers for air and water; therefore, the uncertainty bars were estimated as a 1% conservative uncertainty of the predicted pressure drop in Figure 5.11 and Figure 5.12. Peculiarly, they were evaluated as 1.5% of the pressure drop as approximated by STAR-CCM+ with the Foumeny function given the turbulence quantities in the porous region. Therefore, the fine meshes overall provided numerical results close to the asymptotic solutions with the uncertainties less than 1% and ensure a higher than 99% confidence level for the computed values.

In Figure 5.11, although the Ergun correlation is developed with the substantially small pebble and bed diameters, and pebbles are packed with vibration, it predicts the experimental pressure drop data well with an 8.5% average relative difference for both the 1D correlation and Pronghorn FEM compared to the experiments and an 8.34% average relative difference for STAR-CCM+. Macdonald et al. used much smaller particles than the pebbles used in the current experiments; however, the similar packing material and method may have resulted in pressure drop measurements within the 50% prediction band of the Macdonald correlation from [83]. The Foumeny function predicts the pressure drop the most accurately among other valid correlations in [10] (see Table 5.5); however, the Cheng, Eisfeld and Schnitzlein, Harrison, and Liu

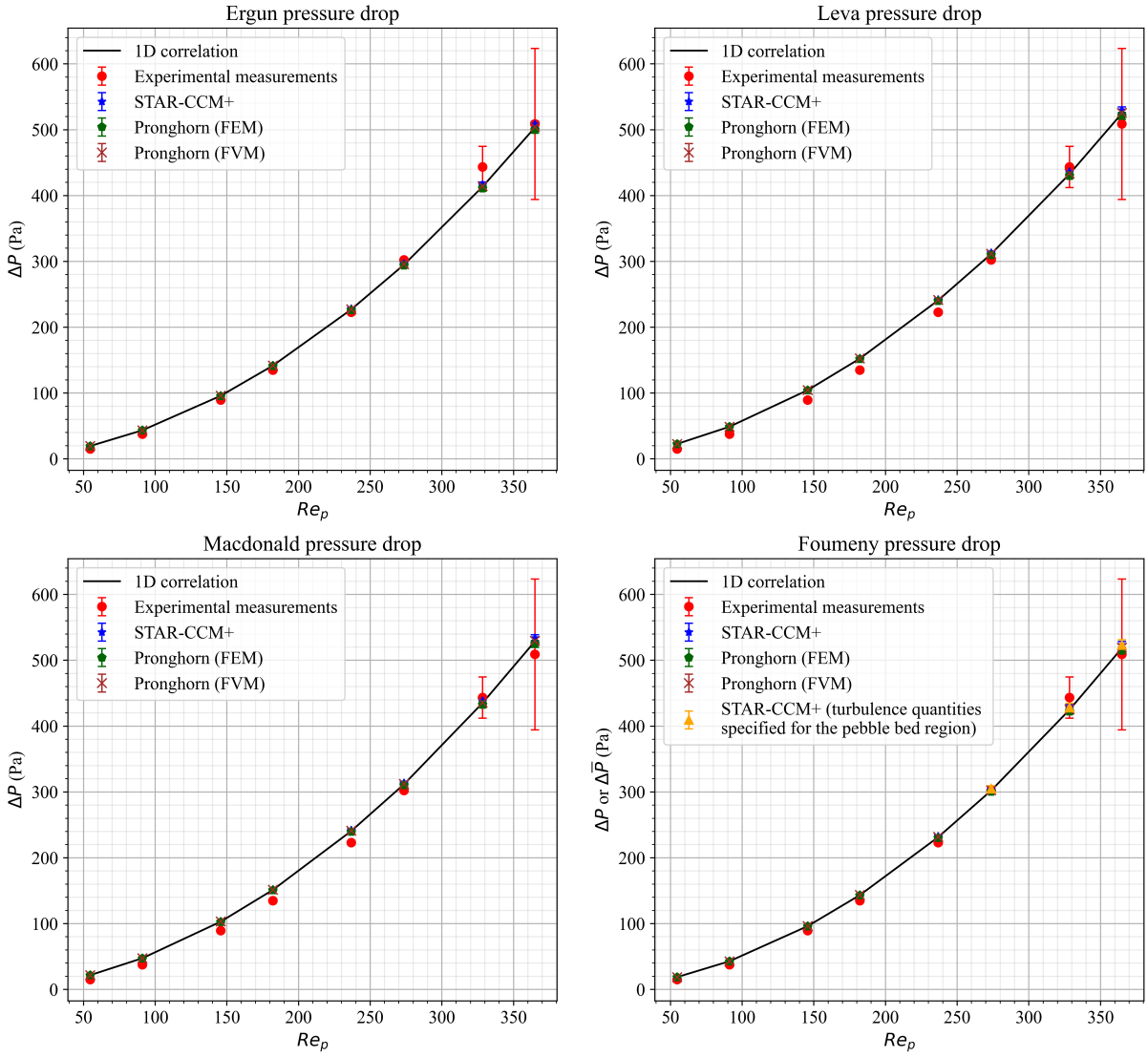

Figure 5.11. Pressure drop estimated by empirical correlations (air). Adapted with permission from [12].

functions, which use the bed diameter to account for the near-wall effects, deteriorate the pressure drop calculation. Figure 5.13 describes the gauge pressure and velocity magnitude profiles for $Re_p = 365$ given the Foumeny function.

For the experiments with the nearly incompressible fluid (water), the Montillet dense packing model brings the lowest RMSEs, RRMSEs, average L^2 norms, and averages of the total normalized Euclidean distance with Pronghorn and STAR-CCM+. The Montillet function was developed based on the similar pebble and bed sizes, including the random packing of glass particles, and it considers the near-wall effects

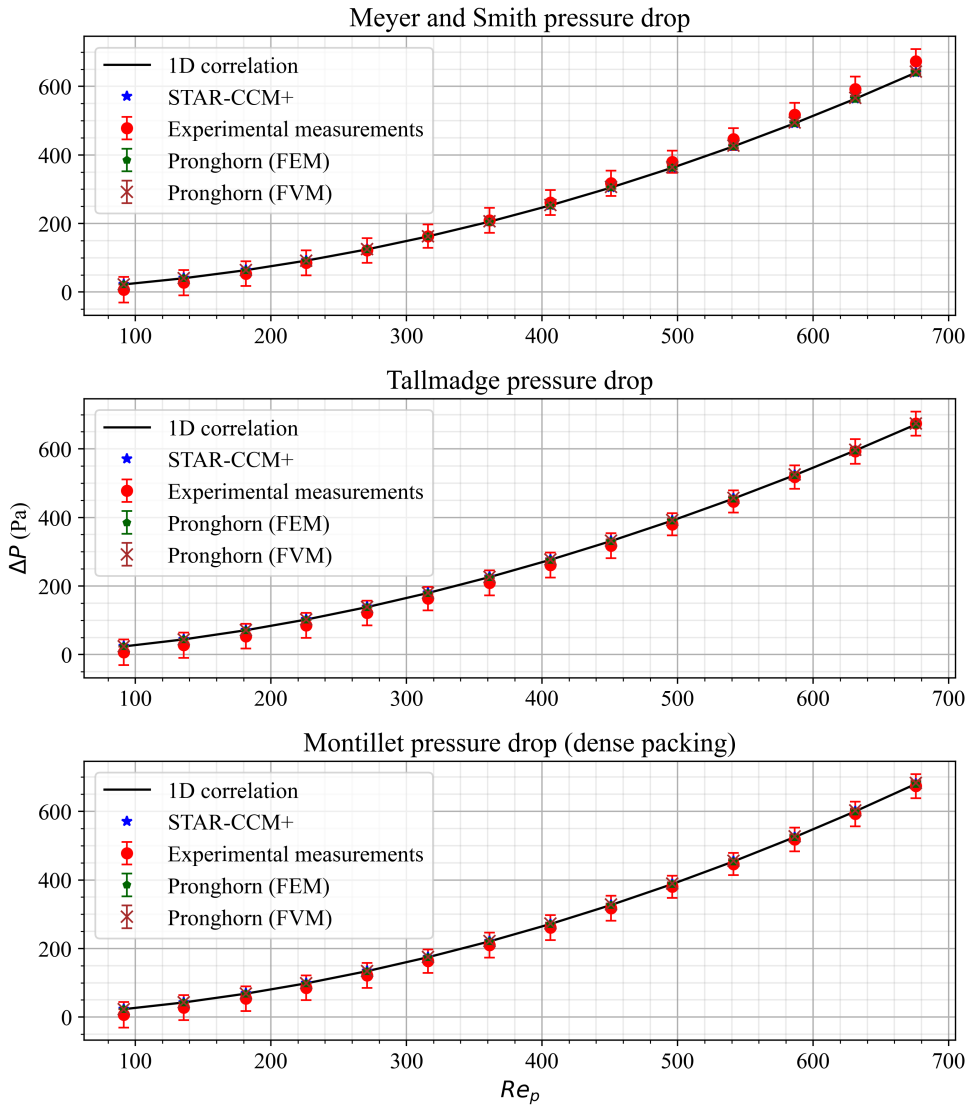

Figure 5.12. Pressure drop estimated by empirical correlations (water). Adapted with permission from [12].

to improve the pressure drop prediction. Although the average relative differences in Table 5.5 are beyond the 10.4% maximum relative difference in [51], in Figure 5.12, overall, the overlap of the 95% confidence interval bars of the experiments and simulation results is more than half of a single arm. Therefore, the two-tailed p-value is $\leq$0.05, and this provides strong evidence for the null hypothesis of the zero difference in means [181–183]. In other words, the statistical significant effect is most likely small.

Table 5.5. Validation metrics for the Foumeny and Montillet functions. Adapted with permission from [12].

Validation metrics/model	Foumeny (air)			Montillet (dense packing, water)		
	Pronghorn FEM	Pronghorn FVM	STAR-CCM+	Pronghorn FEM	Pronghorn FVM	STAR-CCM+
Average relative difference (%)	7.454	7.707	7.779	26.69[§]	27.37[§]	26.92[§]
RMSE (Pa)	9.2754	9.161	9.355	10.9	12.19	11.23
RMSRE	0.1032	0.1055	0.105	0.6687[**]	0.6742[**]	0.6715[**]
RRMSE (%)	4.227	4.175	4.264	3.958	4.424	4.075
Average L^2 norm (Pa)	26.23	25.91	26.46	40.79	45.59	42
Average of the total normalized Euclidean distance	2.902	3.082[†]	3.094[‡]	0.1621	0.1821	0.1671

[†]The Ergun function provides a similar average of the total normalized Euclidean distance of 3.028 by Pronghorn FVM for air.
[‡]The Ergun function provides a similar average of the total normalized Euclidean distance of 3.012 by STAR-CCM+ for air.
[§]The Meyer function brings similar average relative differences of 24.21%, 24.16%, and 24.26% for Pronghorn FEM, Pronghorn FVM, and STAR-CCM+, respectively.
[**]The Meyer function shows similar RMSREs of 0.6298, 0.6347, and 0.6324 for Pronghorn FEM, Pronghorn FVM, and STAR-CCM+, accordingly.

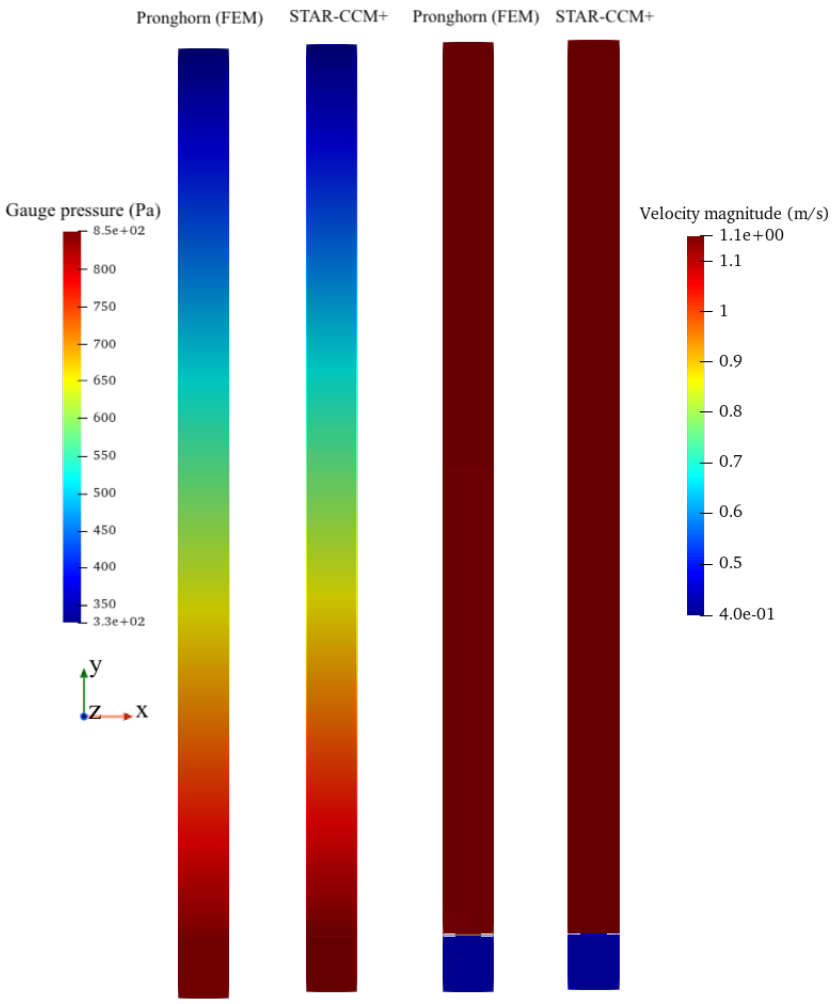

Figure 5.13. Gauge pressure and velocity magnitude profiles estimated by the Foumeny function with Pronghorn and STAR-CCM+ for $Re_p = 365$. Reprinted with permission from [12].

5.3 TAMU Isothermal Pebble Bed Experiments II

5.3.1 Pebble Bed Reconstruction

The new pebble bed facility was reconstructed by the MATLAB algorithms and VGSTUDIO. While the detailed MATLAB pebble bed reconstruction process is provided in [180], the following VGSTUDIO reconstruction method brought the average bed porosity and radial porosity profile used in the porous media simulations in Section 5.3.5. First, a total of 100 PIV images were prepared and averaged at each axial location [180]. Six images in the axial direction were stitched together to bring the full height of the pebble bed test section in Figure 5.14. The PIV images were taken with a uniform spacing of 4.064 mm, which place about 4 to 5 images for capturing each sphere.

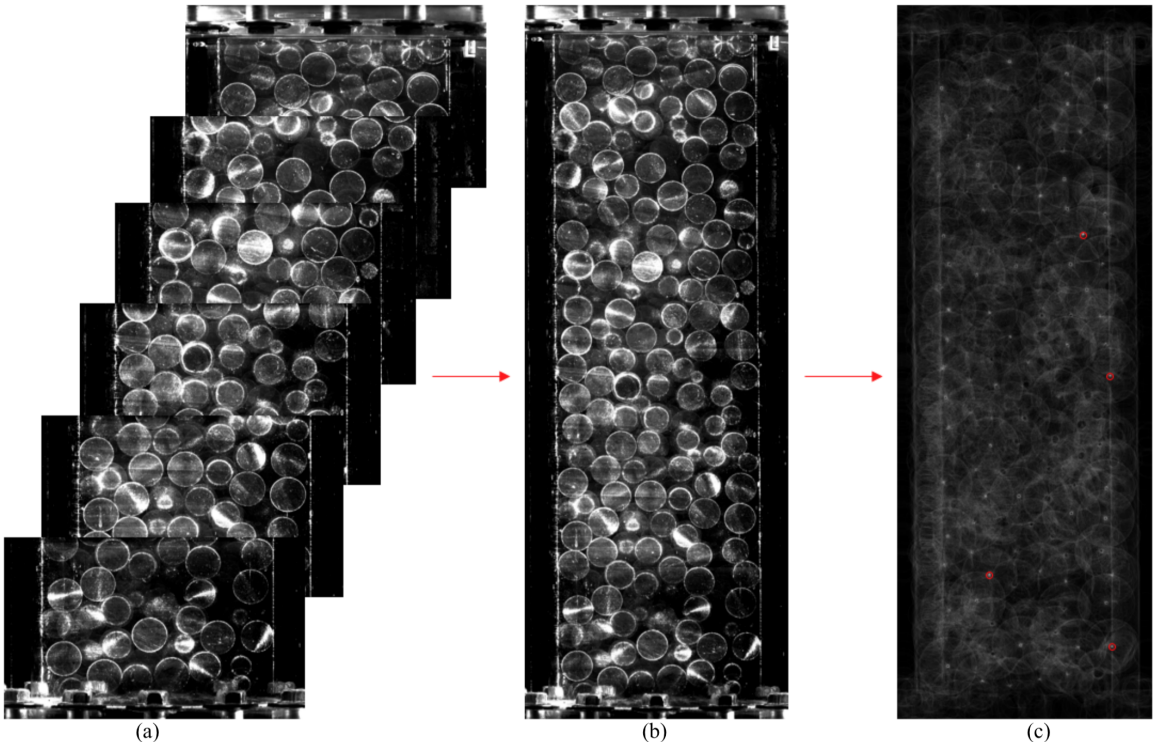

Figure 5.14. Visualization of image processing for reconstructing the pebble bed. (a) Original images at six different axial locations, (b) full view of the stitched image, (c) Hough transform of image (b) with potential circle detection marked with red circles. Reprinted from [180].

After the full views of the channel were constructed, the PIV images were realigned and scaled based on the reference bed height so that they all shared the same coordinate system. Next, the PIV images were transferred into the binary images by applying white pixels for pebbles with the black background of the fluid region after detecting the pebble boundaries. This eliminated the voxel noises in the 3D object. Due to the limited number of images, buffer images were added between 35 PIV images. The horizontal and vertical resolutions were verified to be the same since the images were displayed with square pixels. After stacking the clean images into 3D by using VGSTUDIO, the region of interest (ROI) was created by the geometry analysis tool. The least squares method ("Gauss") found the best fits by providing a set of data points on the spheres. Empty voxels of the buffer layers were modified to white voxels in the ROI specified with all the pebbles in the cylindrical bed. This was for creating the complete solid pebbles, and similarly, other empty voxels were assigned to the inverted ROI for developing the fluid region. At last, the gray-scale value distribution was used to observe the material peaks and detect the adequate location of the isosurface line for determining the surfaces.

The reconstruction process of converting the PIV images into the 3D pebble bed is described in Figure 5.15. The fit point distance was observed to verify that the Gaussian least squares method was applied adequately to detect pebbles in Figure 5.16. The 90% of the fit points have less than or equal to 0.324 mm of the fit point distance.

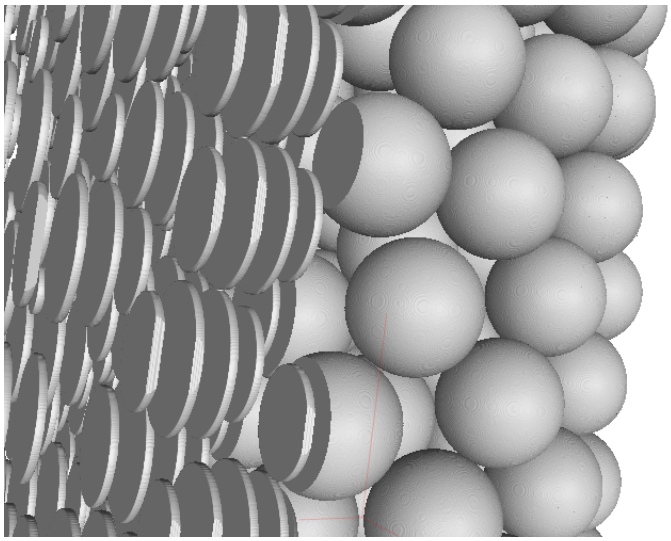

Figure 5.15. 2D PIV images to 3D pebble bed reconstruction.

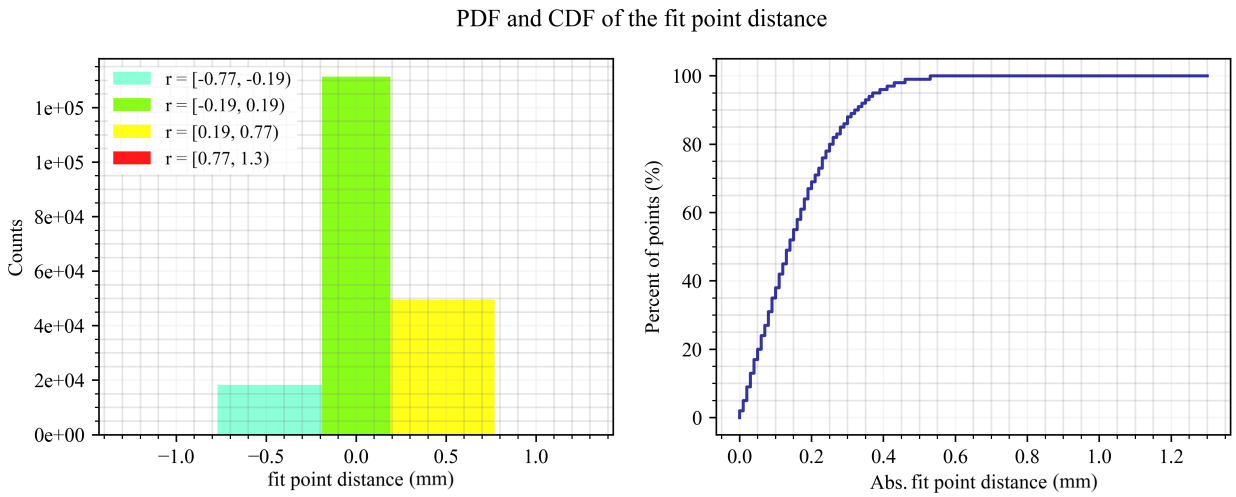

Figure 5.16. Probability distribution function (PDF) and cumulative distribution function (CDF) of the fit point distance.

When pebble surfaces were determined, the foam analysis was performed to observe the thickness of the fluid region between pebbles as the strut thickness. In Figure 5.17 and Figure 5.18, the highest strut thickness is 30.88 mm, and the strut thickness is close to zero when pebbles are touching each other, or pebbles are toughing the cylindrical wall. Figure 5.18 shows that the mean thickness is around 8.78 mm, which is smaller than the pebble radius, and the SD of the thickness is 4.17 mm. The thickness of the fluid region is relatively high at a few locations at the bottom of the bed. It could be from the missing pebbles due to non-detected circles from the PIV images, or large random gaps may be generated during the packing process. The strut thickness is provided at the arbitrary radial (y = 68.55 mm) and axial (z = -1.78 mm) cross sections given the origin is located at the center of the bed in Figure 5.19. The strut thickness value randomly distributes between $\sim$0 and 24.7 mm in these 2D cross sections, which indicates the random packing structure of the pebbles.

A total of 1,047 pebble locations from MATLAB and VGSTUDIO were compared within the bed height of 0.4223 m. The *scipy.spatial.KDTree* class created a set of k-dimensional points with the MATLAB data, and the *scipy.spatial.KDTree.query* function queried the kd-tree for nearest neighbors from the VGSTUDIO data. Here, k would be 3 for the three-dimensional space. Consequently, two sets of the pebble center coordinates from the MATLAB and VGSTUDIO data were paired, and the histogram of the Euclidean distance between these pebble centers is shown in Figure 5.20. The averaged Euclidean distance is 3.309 mm, and

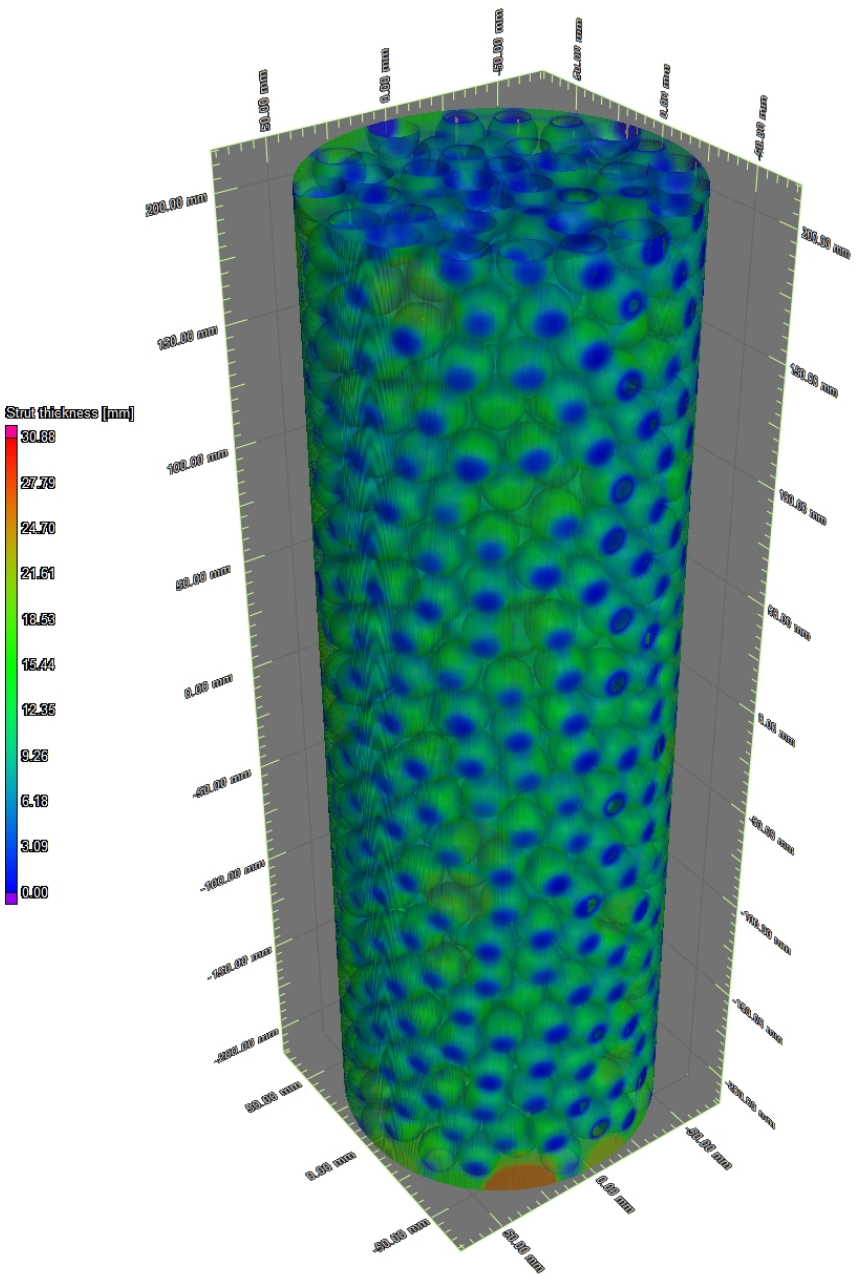

Figure 5.17. Strut thickness in 3D reconstructed pebble bed.

the SD is 1.814 mm. Figure 5.21 shows the visual comparison of the pebble locations obtained by MATLAB and VGSTUDIO in 3D (left) and 2D (right) views. While the majority of the Euclidean distances between the paired pebble center coordinates are less than d_p/2, the Euclidean distances from the twelve sets of pebble locations are greater than d_p/2, represented in Figure 5.22. Twelve sets of the pebble locations were

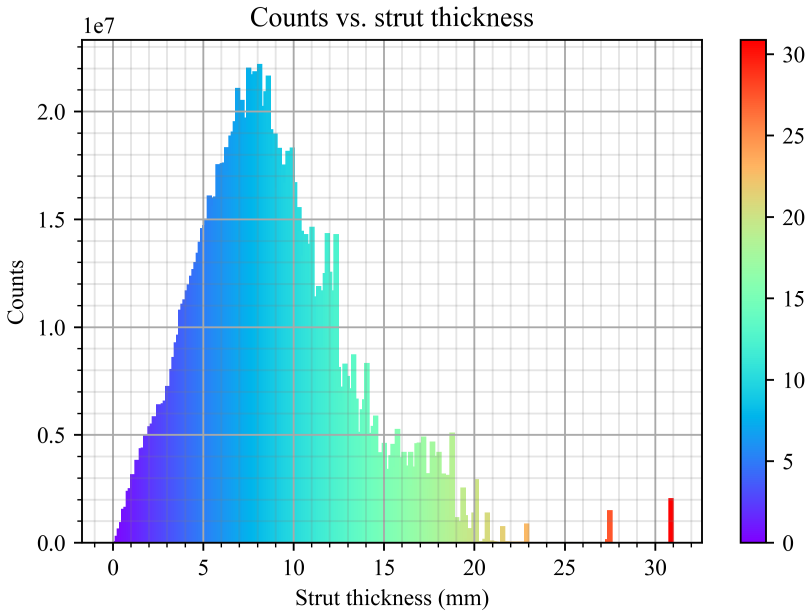

Figure 5.18. Strut thickness distribution.

located near the reconstructed bed surfaces (either top or wall). Generally, pebbles near the top surface were fitted with the points in less than a sphere volume, which could feasibly add errors in the pebble detection. About 1.1% of pebbles provided the relatively large Euclidean distances, but these values are still less than the pebble diameter. Therefore, the average porosity values from MATLAB and VGSTUDIO are expected to be similar while CFD modeling with an explicit mesh of the porous bed may require further improvement of the MATLAB clustering algorithms for accurately estimating the fluid behavior in the pebble bed.

The pebble bed was reconstructed either with the original pebble diameter or 99% of it for avoiding the singularity point issues in finite element analysis, described in [101]. Note that the fabrication tolerance of pebbles in the experiments is about 1% compared to the original pebble diameter, and 206 pixels per inch by VGSTUDIO provides the 0.65% size per pixel, also in reference to the original pebble diameter. Macros were written by using the data of pebble center coordinates for automating the generation of spheres in SOLIDWORKS 2020 SP05. After creating the pebbles, the fluid volume was extracted by constructing the cylindrical bed in a CAD model (see Figure 5.23), and the consequent average porosity value was found. Table 5.6 includes the average bed porosity values computed by different reconstruction methods and by hand. The relative differences of the average bed porosity values with respect to the reference data from

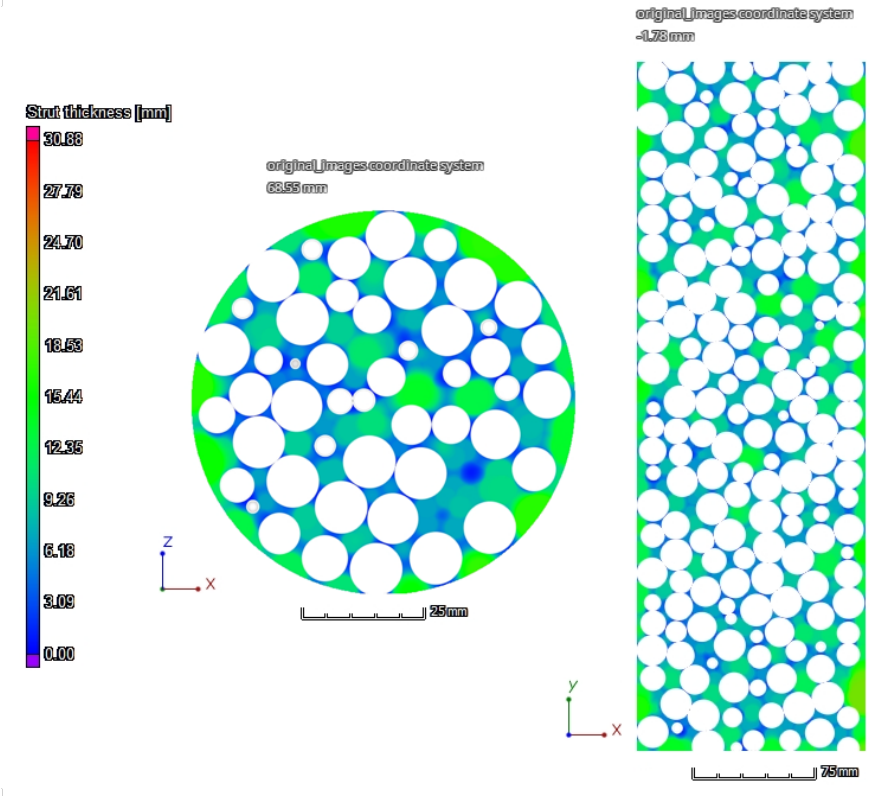

Figure 5.19. Strut thickness at the arbitrary radial (left) and axial (right) cross sections of the reconstructed bed.

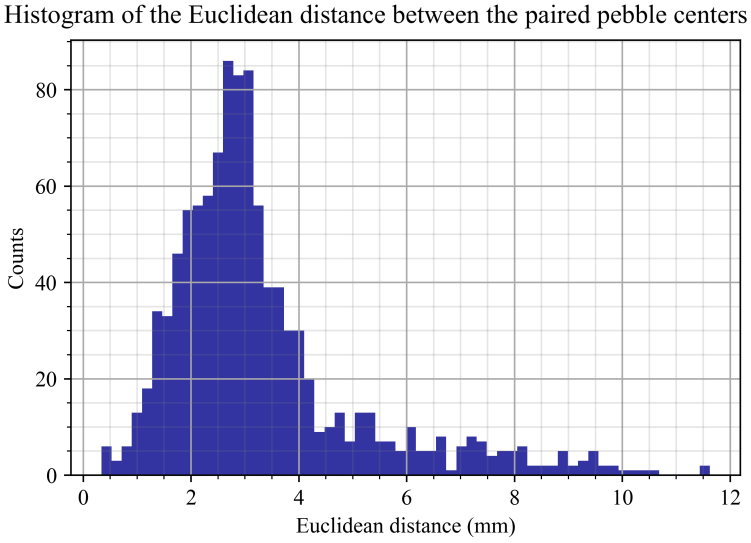

Figure 5.20. Histogram of the Euclidean distance between the paired pebble centers.

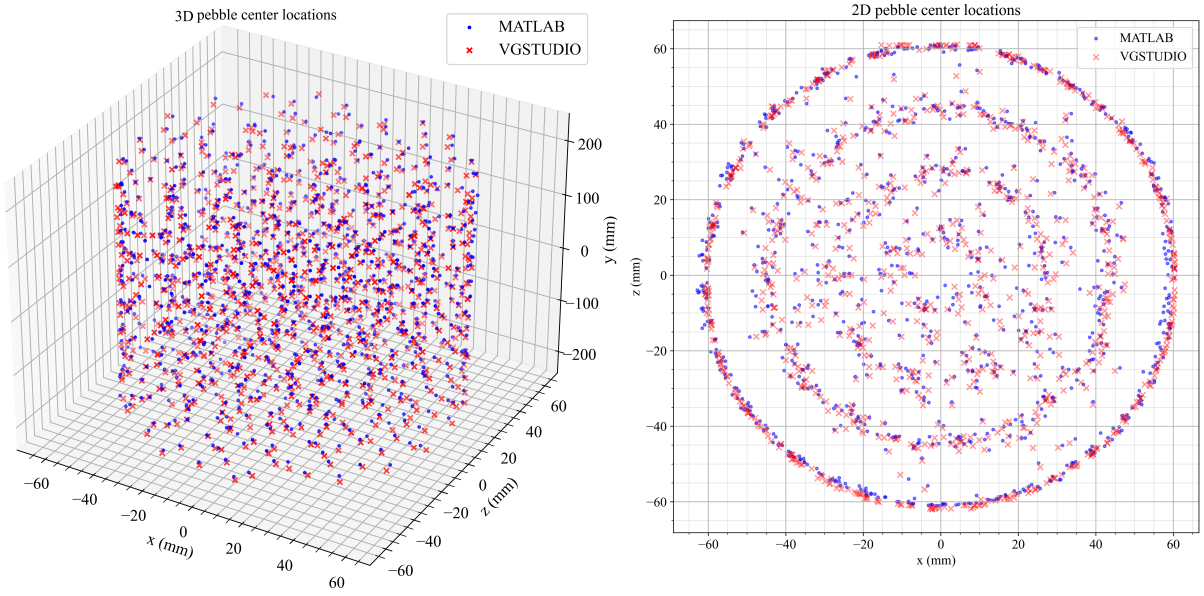

Figure 5.21. 3D and 2D pebble center locations.

Equation 3.3 are less than 1.22%. However, reducing the pebble diameter overall by 1% can change the average bed porosity by ∼4%, which may have an impact on the pressure drop prediction in the porous bed.

Table 5.6. Average bed porosity calculation.

		Reconstruction method or hand calculation		
		MATLAB	VGSTUDIO	Hand calculation
Pebble diameter (m)	$0.99d_p$	0.4378	0.434	0.4335 ± 0.01046
	d_p	0.4213	0.417	0.4162 ± 0.01076

The average and maximum volumes of the overlap between two spheres in percentage are shown in Table 5.7, and the histogram of the overlap volume is described in Figure 5.24. The MATLAB algorithms provided the maximum overlap between two spheres as 24% by volume in the reconstruction with the original pebble diameter, and the average overlap was under 1%. Overall, VGSTUDIO produced less average and maximum overlap volumes compared to those values from MATLAB. Therefore, more accurate reconstruction was accomplished by VGSTUDIO. The overlap was calculated by using the distance between the

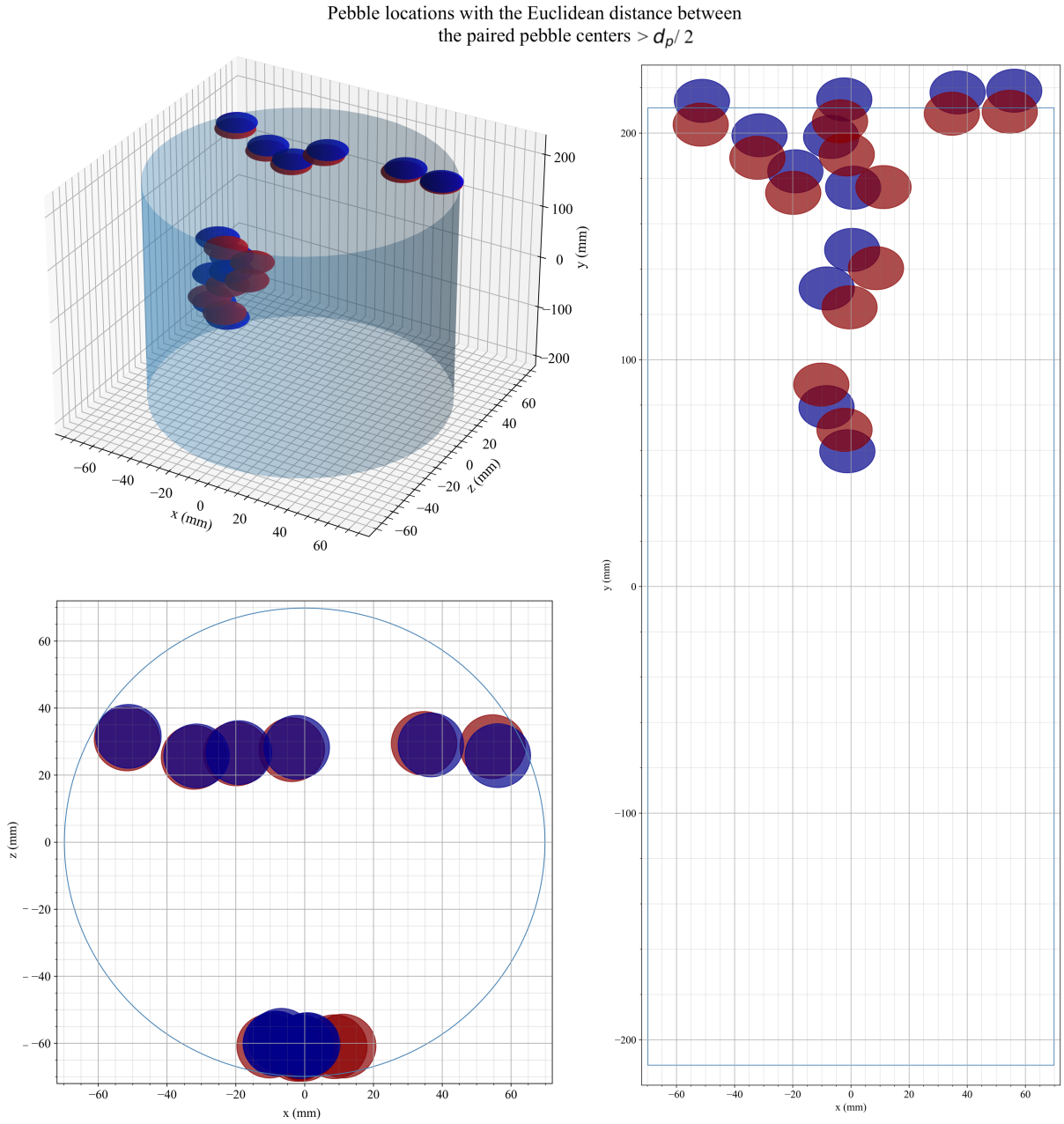

Figure 5.22. Pebble locations with the Euclidean distance between the paired pebble centers $> d_p/2$. Red spheres are located by VGSTUDIO while blue spheres are from MATLAB.

sphere centers, smaller than either $0.99d_p$ or d_p. These overlaps could occur due to slight errors in calibration or improper clustering of the circles in images, especially for MATLAB. Additionally, the statistics of the distance between the centers of touching spheres are provided in Table 5.8. In the reconstructed geometries, these pebbles were touching each other, slightly overlapped, or observed with a small gap due to

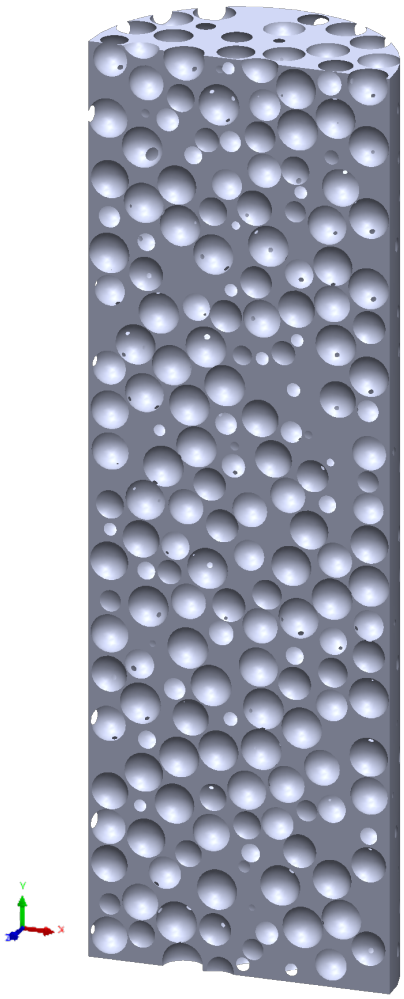

Figure 5.23. Fluid volume in SOLIDWORKS. The axial cross section view is provided to observe the internal structure.

the reconstruction errors. The relative difference in the average minimum distance for VGSTUDIO with reference to the original diameter is 0.25% while MATLAB provides 1.9%, and the relative SDs from MATLAB are higher than those from VGSTUDIO, which also verifies that the VGSTUDIO reconstruction is comparatively accurate.

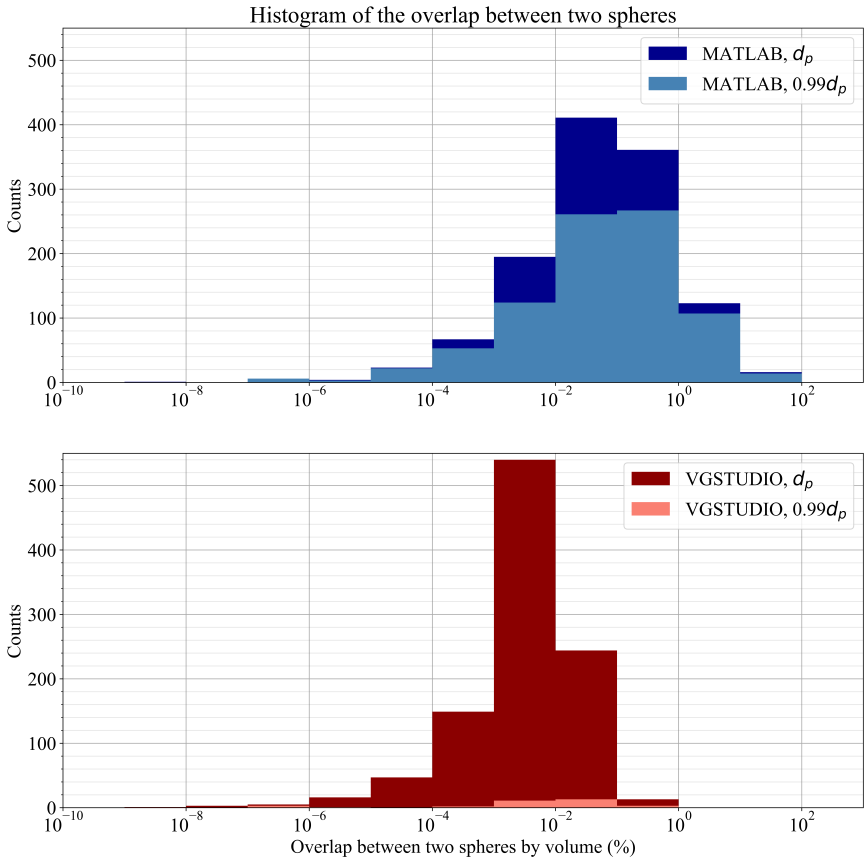

Figure 5.24. Histogram of the overlap between two spheres by volume.

Table 5.7. Studies related to the overlap volume.

Reconstruction method	MATLAB		VGSTUDIO	
Pebble diameter (m)	$0.99d_p$	d_p	$0.99d_p$	d_p
Average overlap volume (%)	0.7039 ± 2.092	0.5863 ± 1.881	0.03883 ± 0.05933	$8.313 \times 10^{-3} \pm 0.02202$
Maximum overlap volume (%)	23.43	24.01	0.2996	0.4387

Table 5.8. Statistics of the minimum distance between the centers of touching spheres.

Reconstruction method	MATLAB		VGSTUDIO	
Pebble diameter (m)	$0.99d_p$	d_p	$0.99d_p$	d_p
Average minimum distance (mm)	18.53	18.7	19.02	19.1
Relative SD (%)	5.026	4.765	0.6596	0.9112

5.3.2 Radial Porosity Study

At every $0.12d_p$ cylindrical layer, the local porosity was found to generate the oscillatory radial porosity profiles. See Figure 5.25 for the locations of the radial surfaces, which the local porosities were obtained at. Here, the full bed height was utilized for acquiring the porosity. The radial porosity profiles with the $0.12d_p$ interval length are similar to the profiles with the $0.073d_p$ interval length in Figure 5.26. Overall, the maximum relative difference between the corresponding porosity profiles, derived with different interval lengths, is 0.6%. Therefore, the following porosity study was completed by taking the local porosity at every $0.12d_p$ cylindrical layer, assuming that there are small discrepancies in the porosity values, except for generating the new radial porosity function. The average relative difference between the MATLAB and VGSTUDIO porosity profiles in Figure 5.27 is 2.3%. It can be seen that VGSTUDIO is preferable by observing the maximum overlap between pebbles by volume and relative SD of the minimum distance between the centers of touching spheres (see Table 5.7 and Table 5.8). However, the average bed porosity and oscillatory radial porosity from MATLAB are relatively accurate and may also be applicable for the porous media simulations.

The sensitivity of radial porosity was studied within different bed heights, such as d_p, $5d_p$, $10d_p$, $15d_p$, and $20d_p$ (reference data), in Figure 5.28. The distance between two consecutive points on a reference function, which are in the same state of oscillation, is about one pebble diameter. The MATLAB and VGSTUDIO radial porosity profiles follow the similar trend. The $15d_p$ bed height provided the radial porosity close to the reference data with the 1.1% average relative difference for both MATLAB and VGSTUDIO. These precise porosity values would result in the accurate pressure drop prediction in porous media simulations. About a 3% average relative difference was obtained with the $10d_p$ bed height, and further porous media simulations are suggested to confirm that the radial porosity with the $10d_p$ bed height would provide the

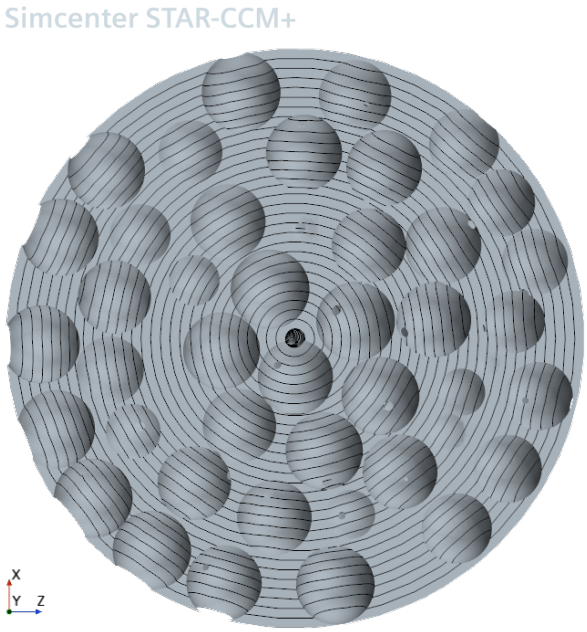

Figure 5.25. Radial cross section of the reconstructed bed including the radial surfaces, where the local porosities are determined.

proper pressure drop estimation. This applies the same for the $5d_p$ bed height, which provided the 4.4% and 5% average relative differences for MATLAB and VGSTUDIO, respectively. With the d_p height, the 7% average relative difference of the porosity was derived with close radial oscillation locations compared to the reference values. The near-wall porosity was approximated adequately among all the heights due to the larger areas of the outer radial surfaces compared to the inner radial surfaces in Figure 5.28. In Figure 5.29, the radial porosity was determined by taking a quarter, a half, and three quarters of the d_p bed volume, and these volumes are described in Figure 5.30. The local porosities are more randomized and the resulting radial porosity is more oscillating with less than the full volume of the d_p bed volume. Therefore, at least the full volume of the d_p volume is necessary to bring the radial porosity oscillation locations similar to those with the $20d_p$ bed height.

The radial porosity obtained by VGSTUDIO with the $0.073d_p$ interval length and original pebble diameter size (the most accurate porosity data from the pebble bed reconstruction) was compared with the existing correlations in Table 2.3 and Table 2.4. In Figure 5.31, the radial porosity functions proposed by Cohen and Metzner, Martin, and de Klerk do not match the porosity from the VGSTUDIO pebble bed reconstruction precisely, therefore, the new oscillating porosity correlation was derived by applying the non-linear least

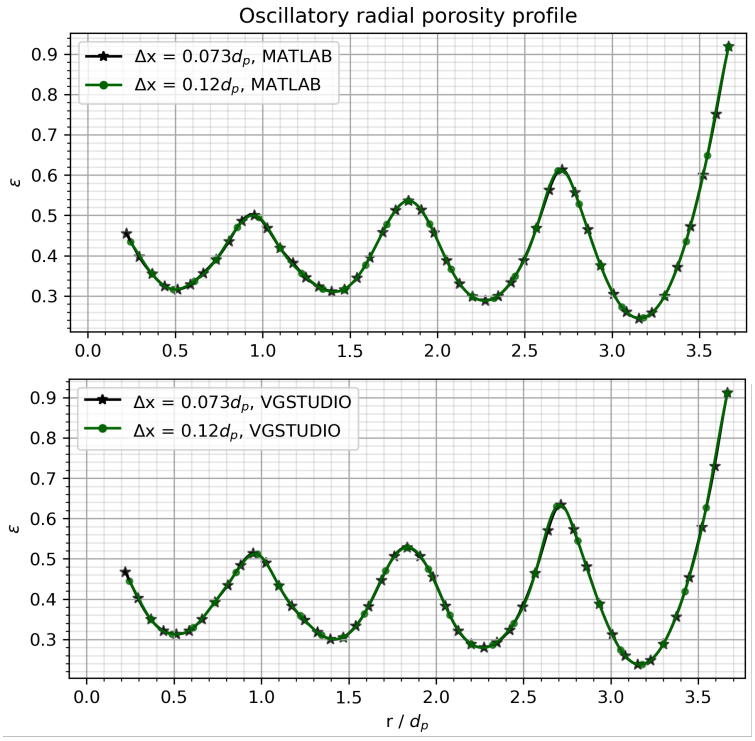

Figure 5.26. Oscillatory radial porosity profile.

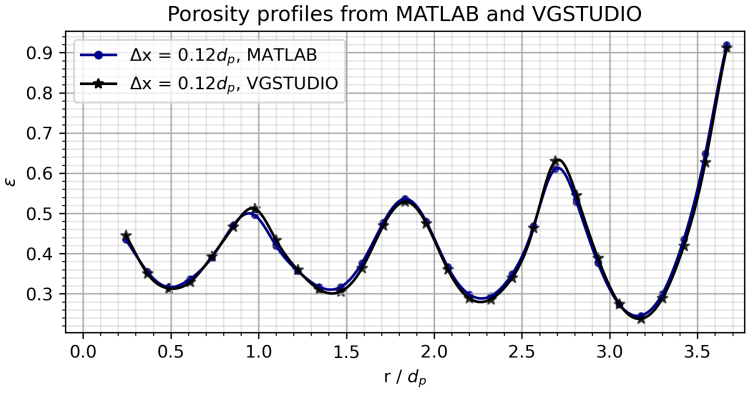

Figure 5.27. Comparison of the radial porosity profiles from MATLAB and VGSTUDIO.

squares method with bounds on the coefficients. The new porosity function was derived based on the Martin porosity correlation in Table 2.3, however, the coefficients were adjusted accordingly given the aspect ratio of 7.33, shown in Equation 5.1. The standard error of the regression is 0.02372 (5.7% of the average bed porosity), and the residual sum of squares (in other words, the cost function) is 0.02701. In Figure 5.31, with the de Klerk function, the discontinuous radial porosities exist at $d/d_p = 0.637$ since the infinite or

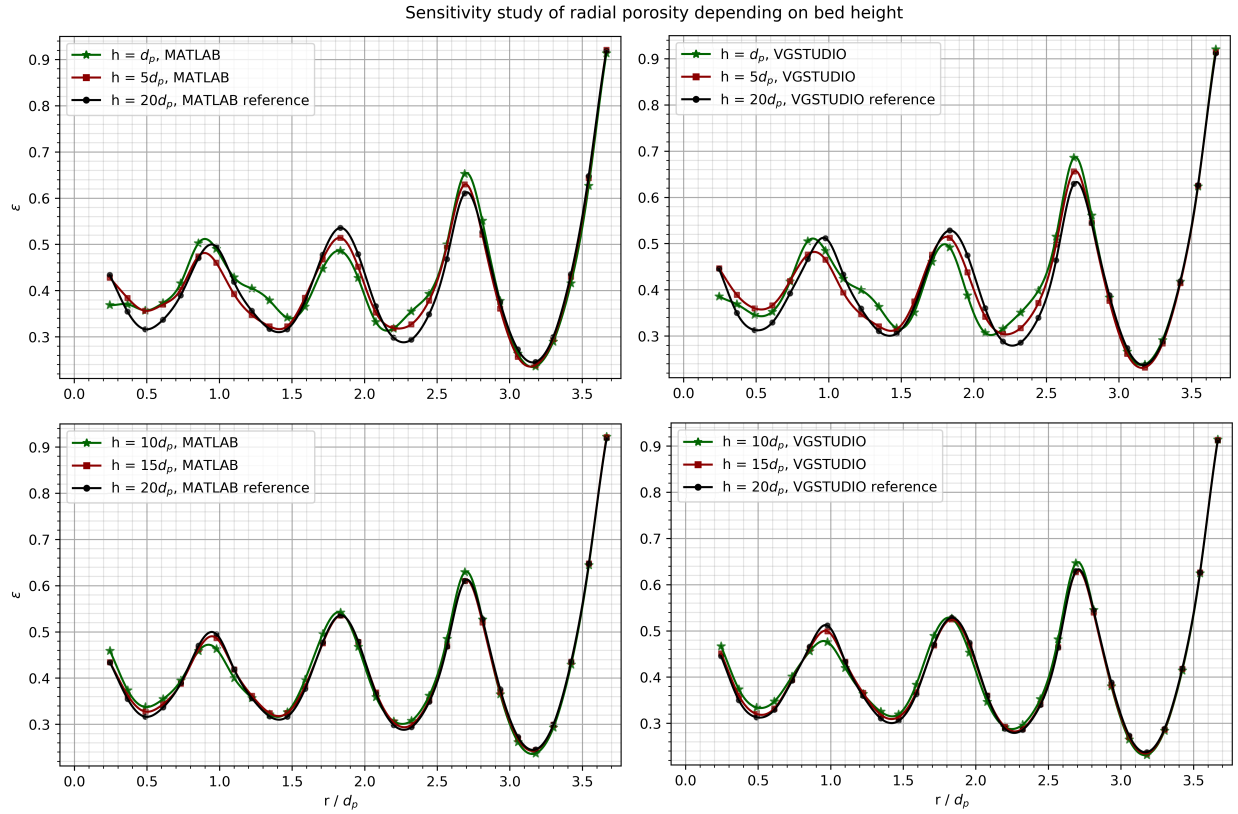

Figure 5.28. Sensitivity study of radial porosity on bed height.

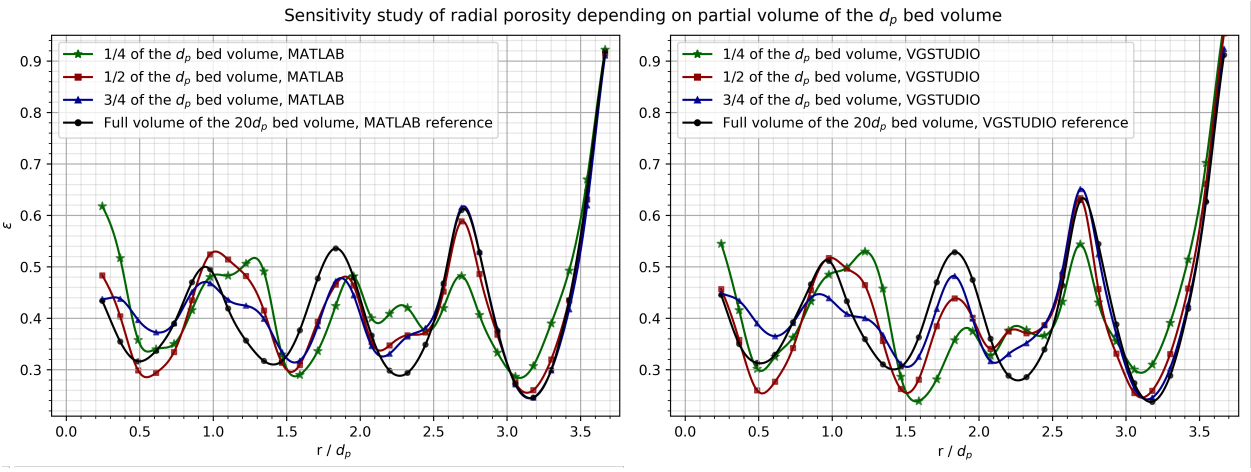

Figure 5.29. Sensitivity study of radial porosity on partial volume of the d_p bed volume.

minimum porosity is not considered to predict the near-wall porosity. On the other hand, the Martin function uses two different regions based on the $2d/d_p - 1$ distance, and the minimum porosity is expected at

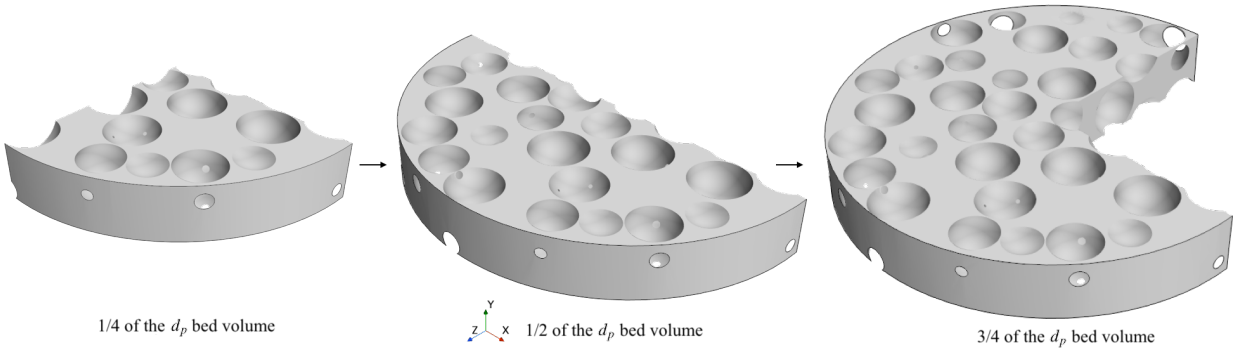

Figure 5.30. The quarter, half, and three quarters of the d_p bed volume.

$d = d_p/2$. Furthermore, the Hunt and Tien function estimates the porosity from the VGSTUDIO pebble bed reconstruction better than other exponential porosity functions in Table 2.4 provided that the average relative difference is 2.5%.

$$\varepsilon = \begin{cases} \varepsilon_{min} + (1-\varepsilon_{min})(\left|\frac{2d}{d_p} - 1\right|)^{2.3} & \text{if } -1 \leq \frac{2d}{d_p} - 1 \leq 0. \\ \varepsilon_{\infty} + (\varepsilon_{min} - \varepsilon_{\infty}) exp\left[-\frac{1}{10}(\frac{2d}{d_p} - 1)\right] cos\left[\frac{\pi}{0.885}(\frac{2d}{d_p} - 1)\right] & \text{if } \frac{2d}{d_p} - 1 > 0. \end{cases} \tag{5.1}$$

Average relative difference = 3.3%.

5.3.3 Average Porosity Correlations

The average bed porosities were determined by MATLAB and VGSTUDIO, and they were validated with the experimental reference data in Section 5.3.1. Furthermore, some average bed porosity correlations with specific validity conditions were examined for future references in Figure 5.32, similar to the approach in Section 5.2. Sato et al. predict the average porosity better than other functions in Table 2.1 with the 0.24% relative difference given the aspect ratio of 7.33, represented as the red lines in Figure 5.32. The Sato experimental specifications are similar to the TAMU isothermal experimental setups, such as the random packing method, pebble diameter, column diameter, material for pebbles, and the material for the column. The parameters of the current experiments also fall within the correlation's validity conditions. The uncertainty bands are provided for the Sato function and the Benyahia and O'Neill correlation. They were calculated by multiplying the SDs by 2 for the 95% confidence level given the normal distributions. The Sato uncertainty

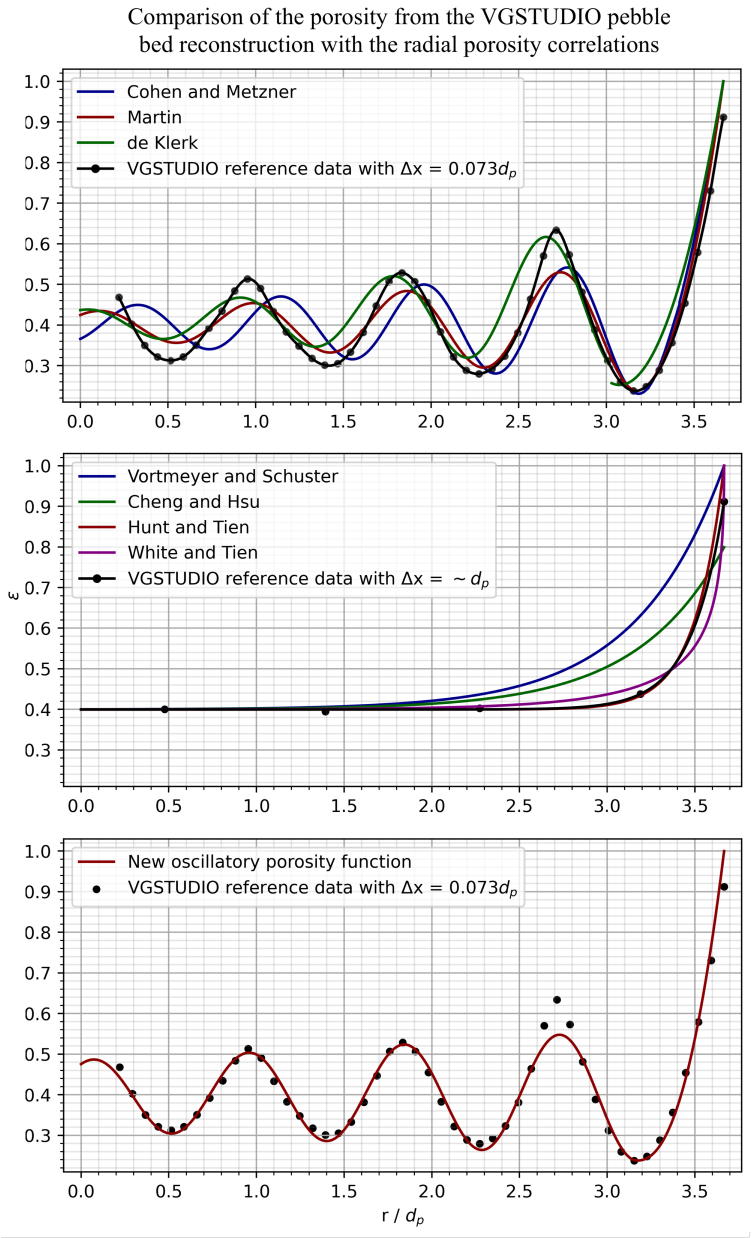

Figure 5.31. Comparison of the porosity from the VGSTUDIO pebble bed reconstruction with the radial porosity functions in Table 2.3 and Table 2.4.

is less than 1% of the average porosity at the aspect ratio of 7.33 while Benyahia and O'Neill provide 7.2% of the average value.

Other correlations still have comparable relative differences up to 1.6% in Figure 5.32. Although the aspect ratio is smaller than 10 for the current experiments, the Aerov function estimated the average porosity well. Gentle tapping by de Klerk, Benyahia, and O'Neill did not add much discrepancies in the average

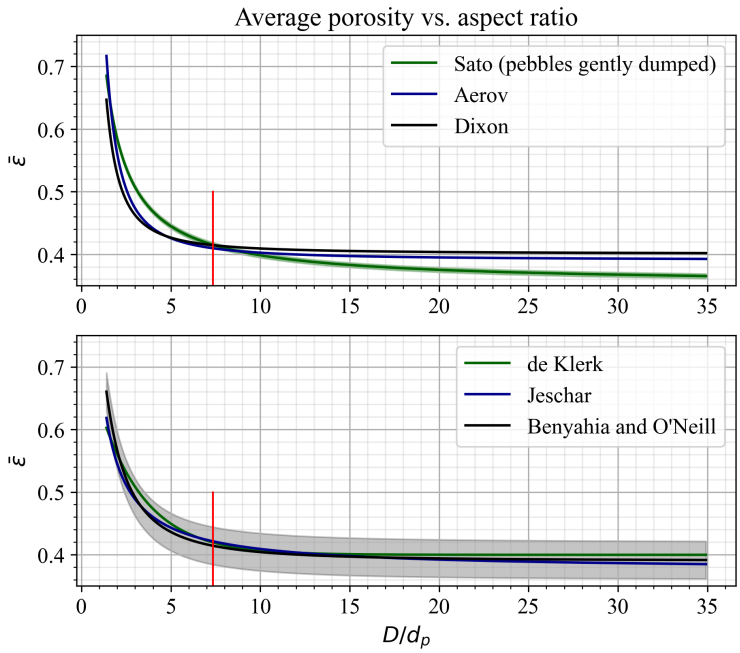

Figure 5.32. Average bed porosity with respect to the aspect ratio (p-Cymene).

porosity values. The experimental porosity is within both the absolute difference value provided by Dixon and the relative difference in percentage by de Klerk in Table 2.1. However, the studies related to different aspect ratios are recommended since the average porosity profiles with respect to the aspect ratio are different by the researchers in Figure 5.32.

5.3.4 Simulation Uncertainty Quantification

The numerical uncertainties were determined by the GCI method. Although the factor of safety (FS) method can be utilized to overcome the drawbacks of the GCI method, the numerical uncertainties obtained by the GCI method were larger than the values from the FS method. These drawbacks are described as: no smooth variation of F_s follows when the solutions are far from the asymptotic range [144], and an insufficient statistical analysis is shown to determine the uncertainty estimate [184]. Therefore, conservative uncertainties from the GCI method were added to ultimately derive the total simulation uncertainties.

The input uncertainties were computed by LHS, and the summary of the uncertain input parameters for porous media simulations is listed in Table 5.9. The 95% symmetric probability bands of the average porosity, inlet physical velocity, bed diameter, pebble diameter, and the specific bed height for pressure drop measurements were utilized to provide a pseudo-random sample from each equal probability interval. A total of 10 latin hypercube samples were used by evaluating the means and SDs of input parameters given their relative differences are less than 1%. Figure 5.33 shows how the relative difference in percentage evolves by increasing the number of samples. Figure 5.34 represents the CDF of the average bed porosity, and the equal probability bins in [0, 1) were converted to [0.025, 0.975) for providing the samples in the 95% confidence interval. In other words, the sample scaling was completed with specific lower and upper bounds, and these bounds were also applied for other input parameters. Figure 5.35 verifies that a sample was adequately chosen from each probability bin, and only the distribution of a few input parameters is represented due to the limited space. Note that the probability data is provided before scaling for simple visualization purposes. After quantifying the numerical, input, and consequent model uncertainties using Equation 2.55, the simulation uncertainties were derived with Equation 2.56. They were factored by 2 and applied as the Pronghorn and STAR-CCM+ simulation error bars in Figure 5.36, Figure 5.38, and Figure 5.39.

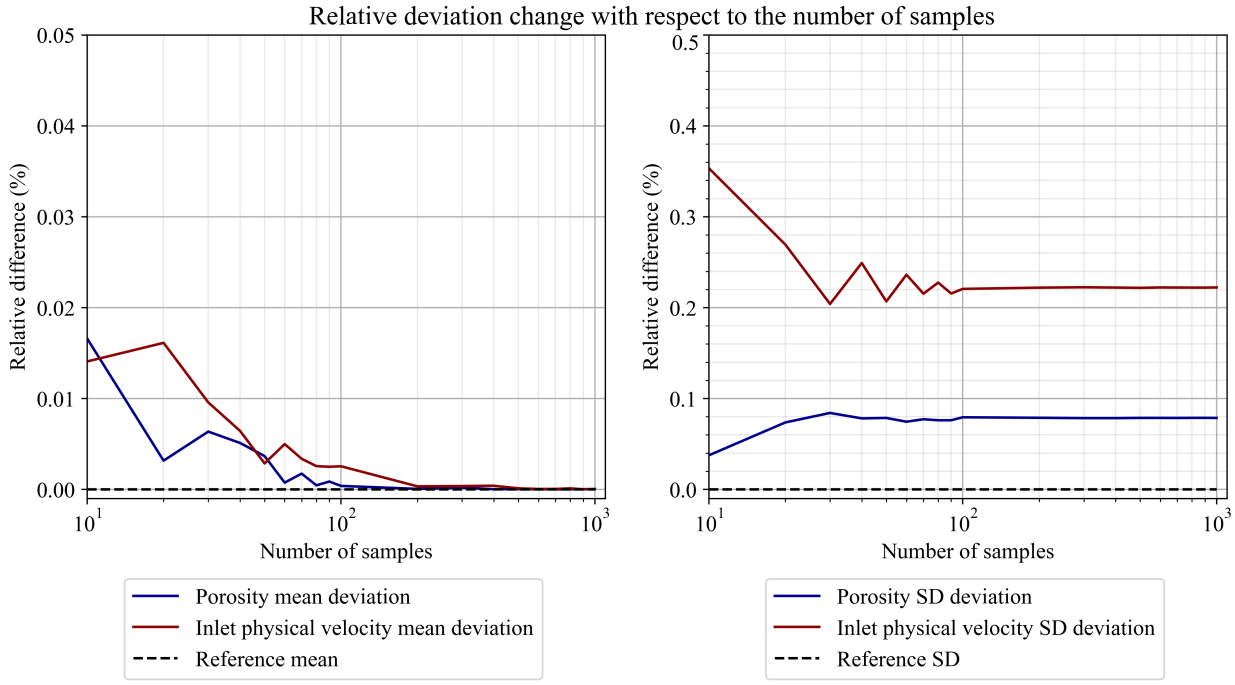

Figure 5.33. Relative difference change with respect to the number of samples.

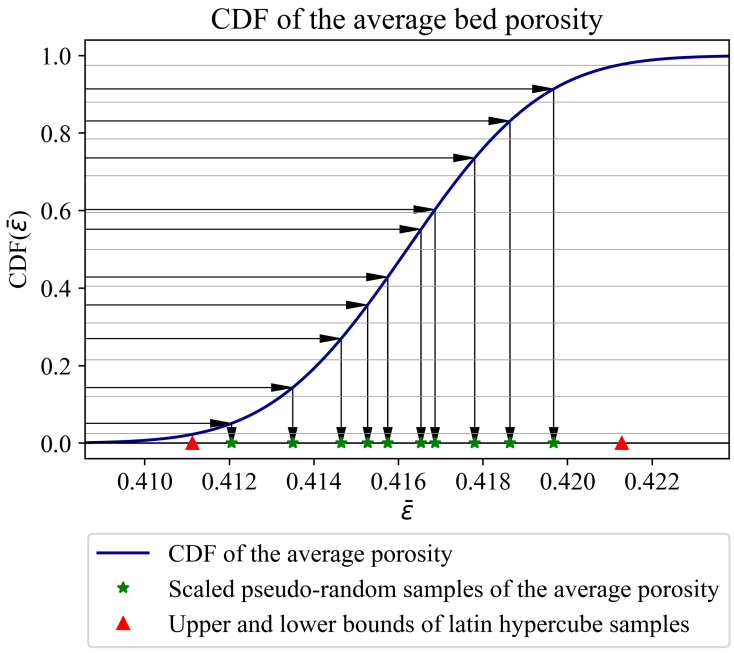

Figure 5.34. CDF of the average bed porosity.

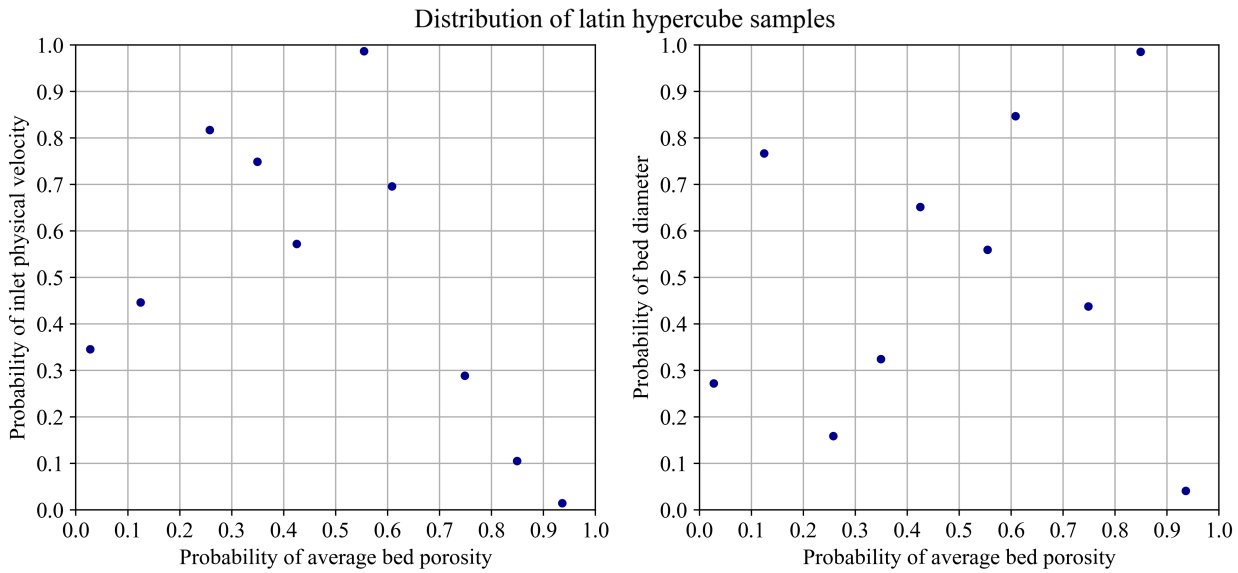

Figure 5.35. Distribution of latin hypercube samples.

Table 5.9. Summary of the uncertain input parameters for porous media simulations.

Input parameter	Mean value	Uncertainty/uncertainty band
Average bed porosity [-]	0.4162	5.078×10^{-3}/[0.4111, 0.4213]
Inlet physical velocity† [m/s]	0.01609	5.547×10^{-4}/[0.01554, 0.01665]
Bed diameter [m]	0.1397	7.938×10^{-4}/[0.1389, 0.1405]
Pebble diameter [m]	0.01905	1.905×10^{-4}/[0.01886, 0.01924]
Specific bed height for pressure drop measurements [m]	0.5334	7.938×10^{-4}/[0.5326, 0.5342]

†Only the data for $Re_p = 324$ is provided due to the limited space; however, an uncertainty band was derived individually for each Reynolds number to quantify the corresponding input uncertainty.

5.3.5 Porous Media Simulations

There are no significant differences in the pressure drop data obtained by the 3D and axisymmetric STAR-CCM+ porous media simulations with the turbulence quantities specified in the porous bed and the SST $k - \omega$ model used for the free flow region in Figure 5.36. The all-y^+ wall treatment with no slip condition for the free flow region was utilized for these specific simulations given the Carman pressure drop correlation. In addition, a laminar model in both the porous and free flow regions did not change the pressure drop significantly (less than a 1% relative difference) and the similar trend is shown in [12]. In

Figure 5.37 (middle and right), the axial velocity goes to zero at the wall, and the fluid moves rapidly near the centerline of the cylinder in the free flow region. However, it did not influence both the pressure drop and volume-averaged axial velocity in the porous region substantially. Therefore, the axisymmetric porous media simulations (incompressible Navier-Stokes equations with the Darcy-Forchheimer model) without the turbulence properties were overall utilized for the V&V of Pronghorn. The mesh convergence tests were performed for all porous media simulations, and the GCIs for fine meshes were obtained at $\leq$1%. This shows that the fine meshes, in general, provided numerical results close to the asymptotic solutions with the $\leq$1% uncertainty and ensured a confidence level of at least 99% for the computed values.

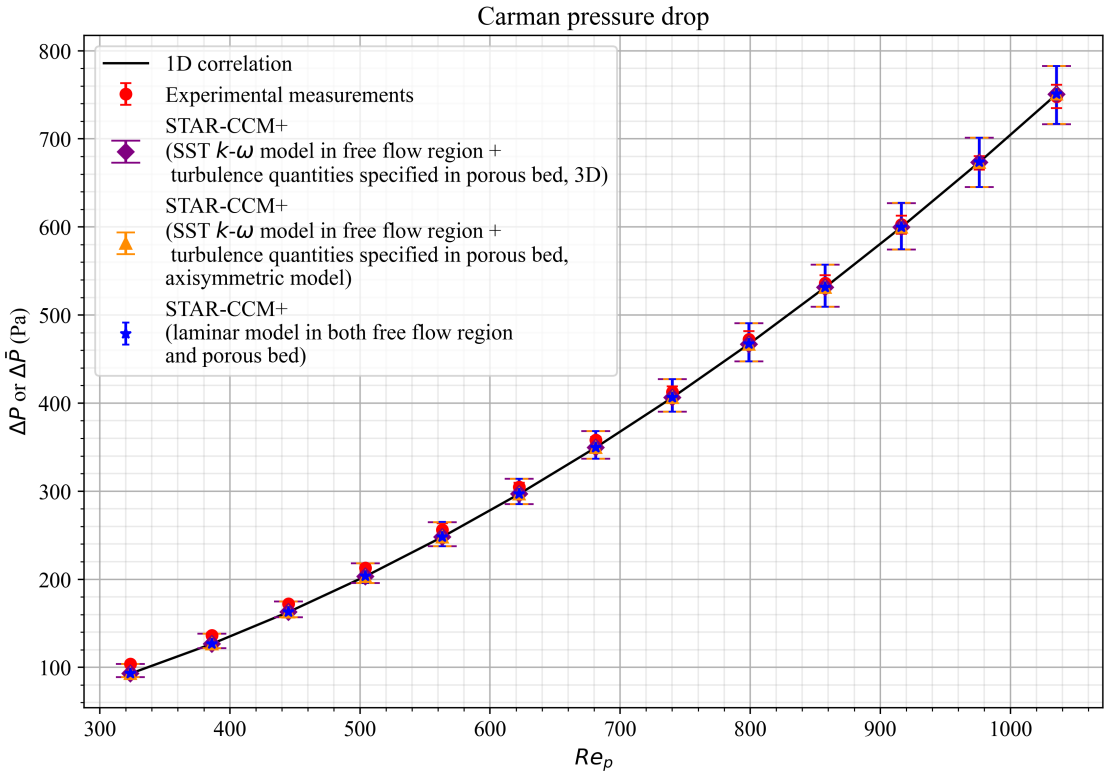

Figure 5.36. Pressure drop comparison of the 2D axisymmetric laminar model with the 3D and axisymmetric STAR-CCM+ porous media simulation results with the turbulence quantities provided in the porous bed and the SST $k-\omega$ model in the free flow region.

The pressure drops predicted by the Pronghorn and STAR-CCM+ porous media models using the pressure drop correlations in Table 2.6 agree well with the experimental pressure drop, as shown in Figure 5.38.

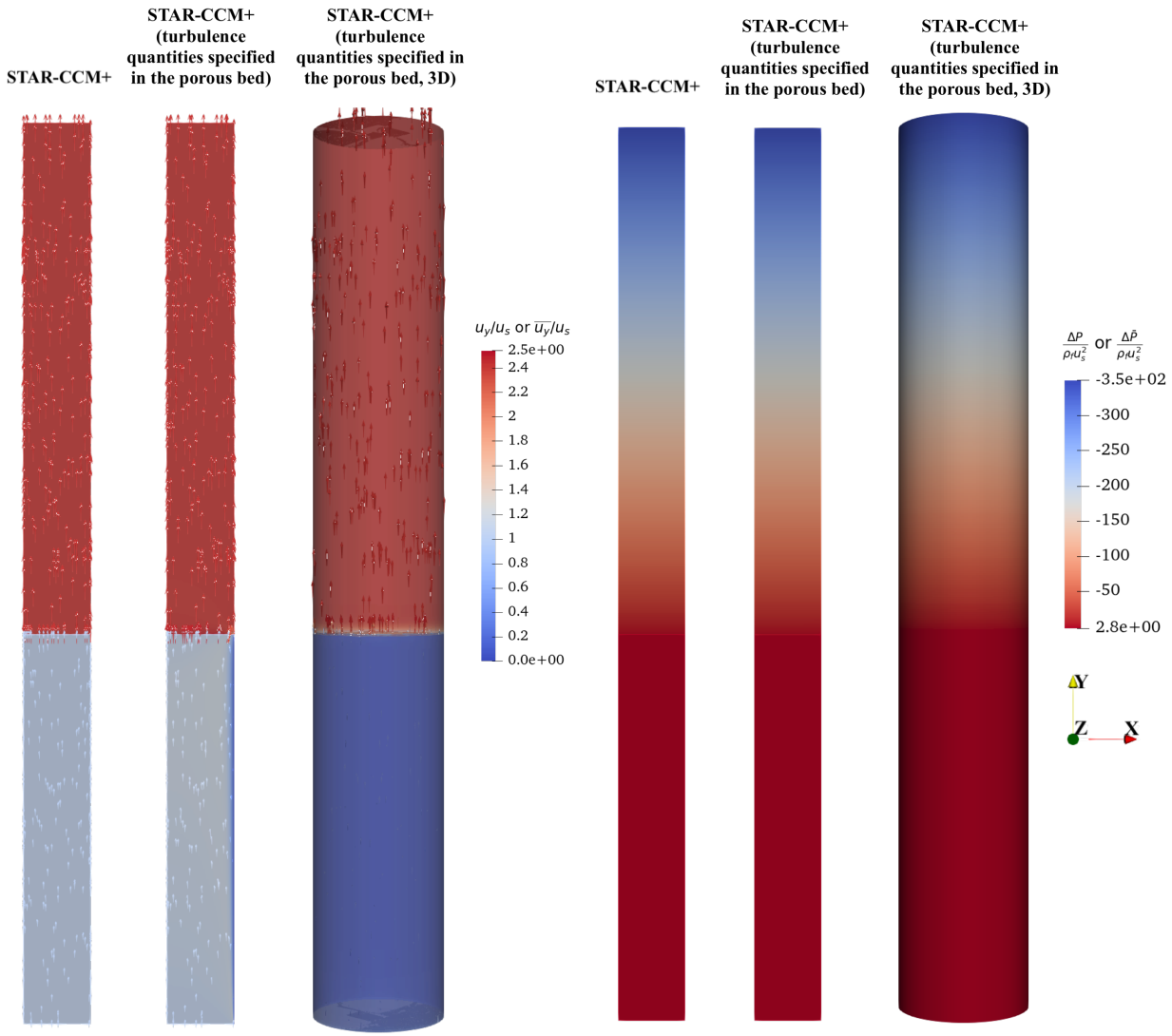

Figure 5.37. STAR-CCM+ dimensionless axial velocity and pressure drop provided the Carman function ($Re_p = \sim$800). Axisymmetric model (left), axisymmetric model with the turbulence quantities specified in the porous bed and the SST $k-\omega$ model in the free flow region (middle), 3D model with the turbulence quantities specified in the porous bed and the SST $k-\omega$ model in the free flow region (right).

In Figure 5.38 and Figure 5.39, the Handley, KTA, and Carman correlations comparably estimate the pressure drop, pressure gradient, and friction factor better than other correlations in terms of the validation metrics in Table 5.10. In Figure 5.39, both the experimental and simulation data are within the uncertainty or error ranges given for the correlations. Despite the fact that the Handley function was developed with relatively small porosity and aspect ratios, the current experimental Re_p range was within its validity condi-

tion. Consequently, the function provided the average relative differences from 2.56% to 3.34% between the experimental data and Pronghorn FEM, Pronghorn FVM, and STAR-CCM+ simulation results. Although the KTA function might not be valid for smaller Reynolds numbers ($Re_p = 324$ and 386), and the Carman function was derived with the aspect ratios larger than 10, the KTA and Carman functions also brought the approximate average relative differences to the values obtained by the Handley function in Table 5.10. The Handley and Carman correlations estimated the pressure drop better than KTA for $Re_p \geq 800$ by observing the absolute difference in pressure drop between the experimental data and simulation results while the KTA function performed better with $Re_p < 800$ in Figure 5.38. The pressure drop data obtained by Pronghorn FEM, Pronghorn FVM, and STAR-CCM+ using the Reichelt, Eisfeld and Schnitzlein, Brauer, Jones and Krier, and Hicks functions were reasonable with the 5.1% maximum average relative difference. Therefore, the Carman-type pressure drop correlations, such as the KTA and Carman functions, with suitable coefficients for the friction factors estimated the pressure drop more appropriately than previous efforts by considering the bed diameter to pebble diameter ratio (aspect ratio) for the near-wall effects.

Table 5.10. Validation metrics for the Handley, KTA, and Carman pressure drop functions.

Validation metrics/ model	Handley			KTA			Carman		
	Pronghorn FEM	Pronghorn FVM	STAR-CCM+	Pronghorn FEM	Pronghorn FVM	STAR-CCM+	Pronghorn FEM	Pronghorn FVM	STAR-CCM+
Average relative difference (%)	3.01	2.56	3.34	2.92	3.1	2.81	2.87	2.6	3.08
RMSE (Pa)	8.05	6.53	9.24	14.1	16.3	12.8	6.8	6.6	7.32
RMSRE	0.0364	0.0323	0.0389	0.0361	0.0369	0.0357	0.0406	0.0376	0.0425
RRMSE (%)	2.1	1.7	2.41	3.68	4.25	3.33	1.77	1.72	1.91
Average L^2 norm (Pa)	29	23.6	33.3	50.9	58.8	46	24.5	23.8	26.4
Average of the total normalized Euclidean distance†	0.577	0.502	0.624	0.55	0.584	0.532	0.596	0.541	0.63

†The experimental error is considered for this specific validation metric.

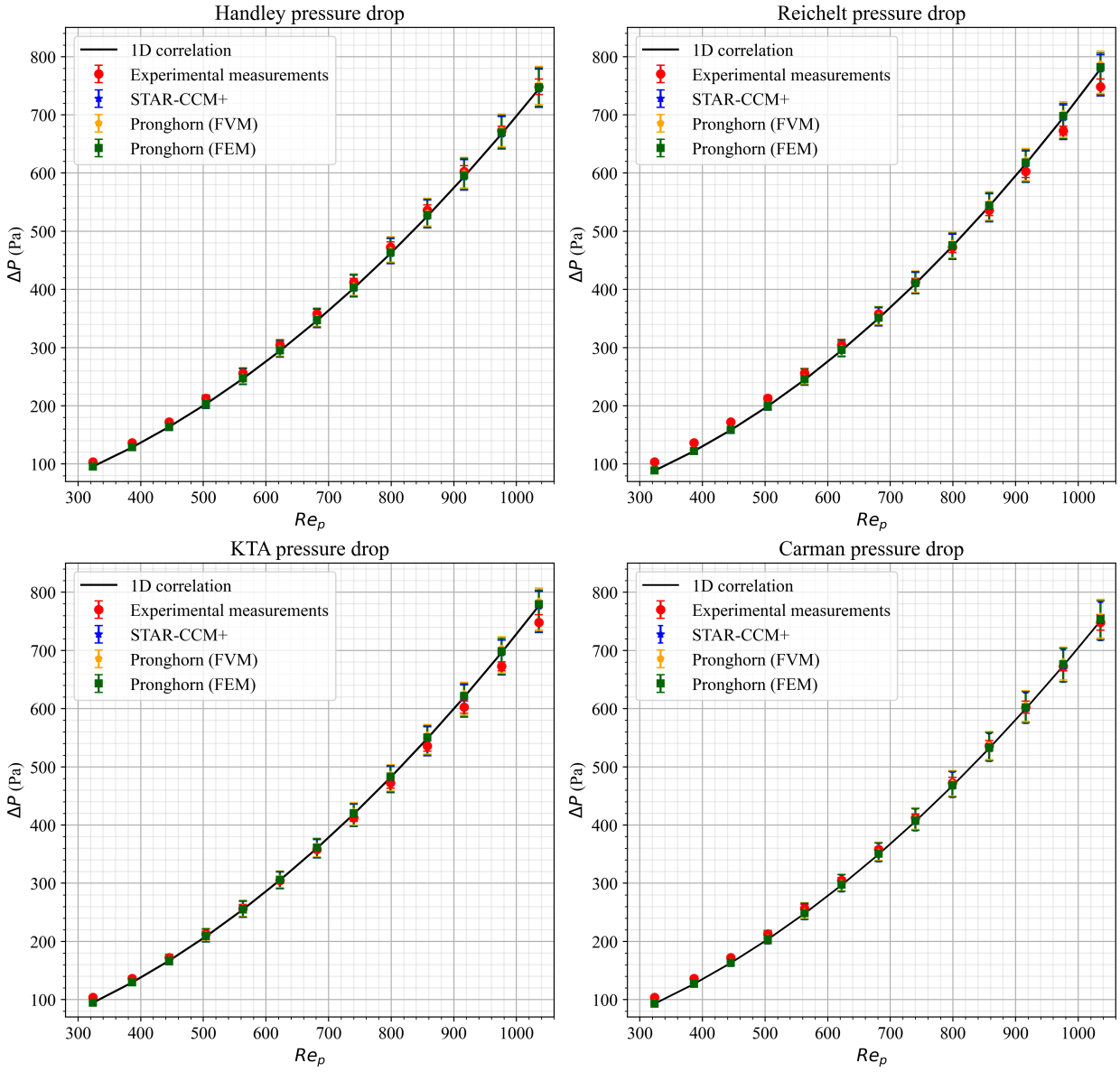

Figure 5.38. Pressure drop with respect to the particle Reynolds number.

By only accounting for the numerical and input uncertainties, the overlap of the 95% confidence uncertainty intervals of the experiments and the Handley, KTA, and Carman simulation results was more than half of a single arm. This provides strong evidence for the null hypothesis of the zero difference in the average values, equivalent to the analysis in Section 5.2. Only the numerical and input uncertainties were considered because propagating the model uncertainties resulted in asymmetric total simulation uncertainties, and the probability distributions were no longer Gaussian distributions.

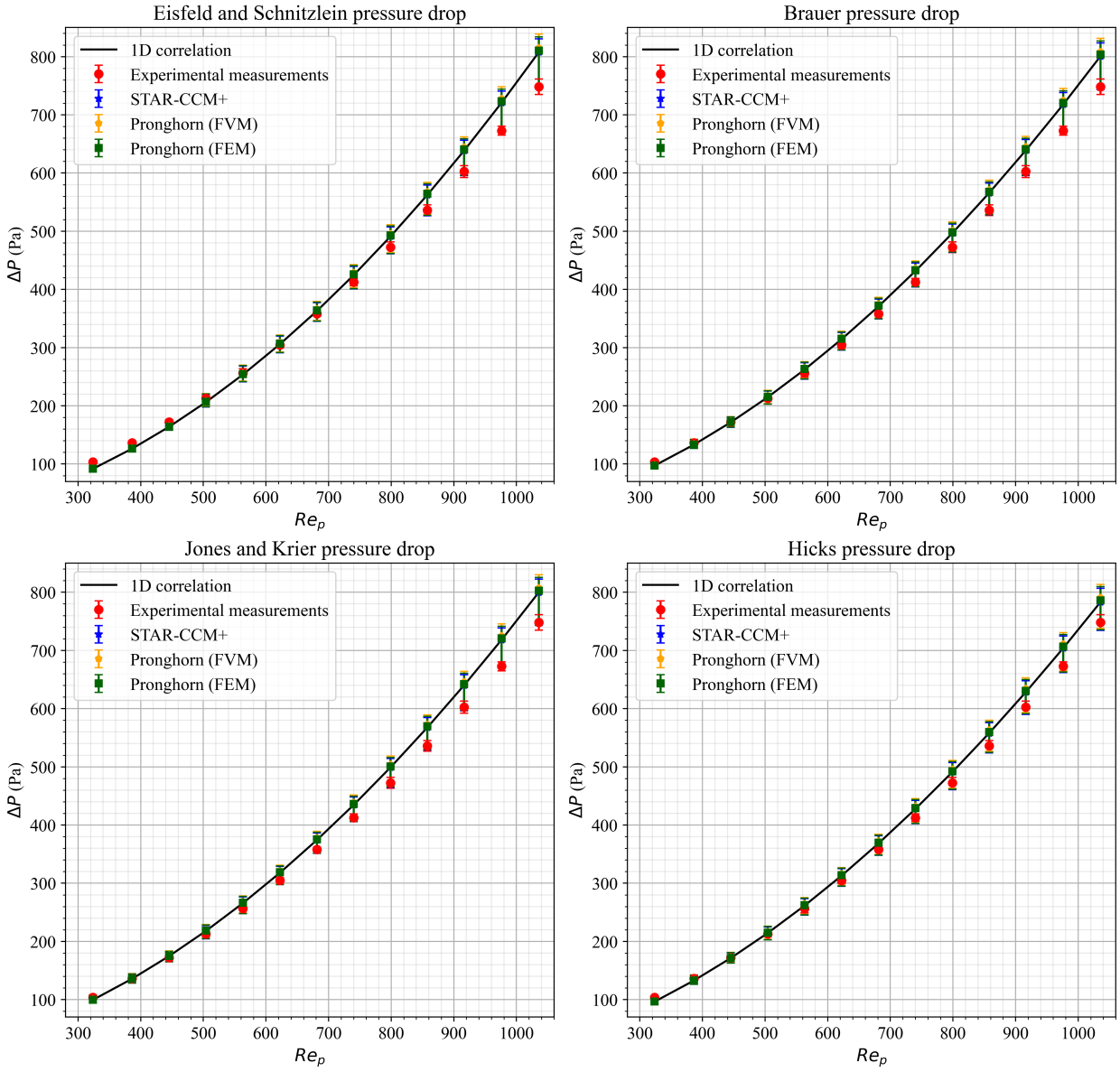

Figure 5.38. Continued.

The average relative differences, RMSEs, RMSREs, RRMSEs, and average L^2 norms were obtained by assuming that both the experimental and simulation data were deterministic. The KTA function showed relatively higher RMSEs, RRMSEs, and average L^2 norms than the Handley and Carman models due to the discrepancies in pressure drop for $Re_p \geq 800$. The averages of the total normalized Euclidean distance were calculated by considering the experimental uncertainties, provided that the simulation data were point values. They are less than the tolerance in Table 2.15 for all Pronghorn and STAR-CCM+ porous media

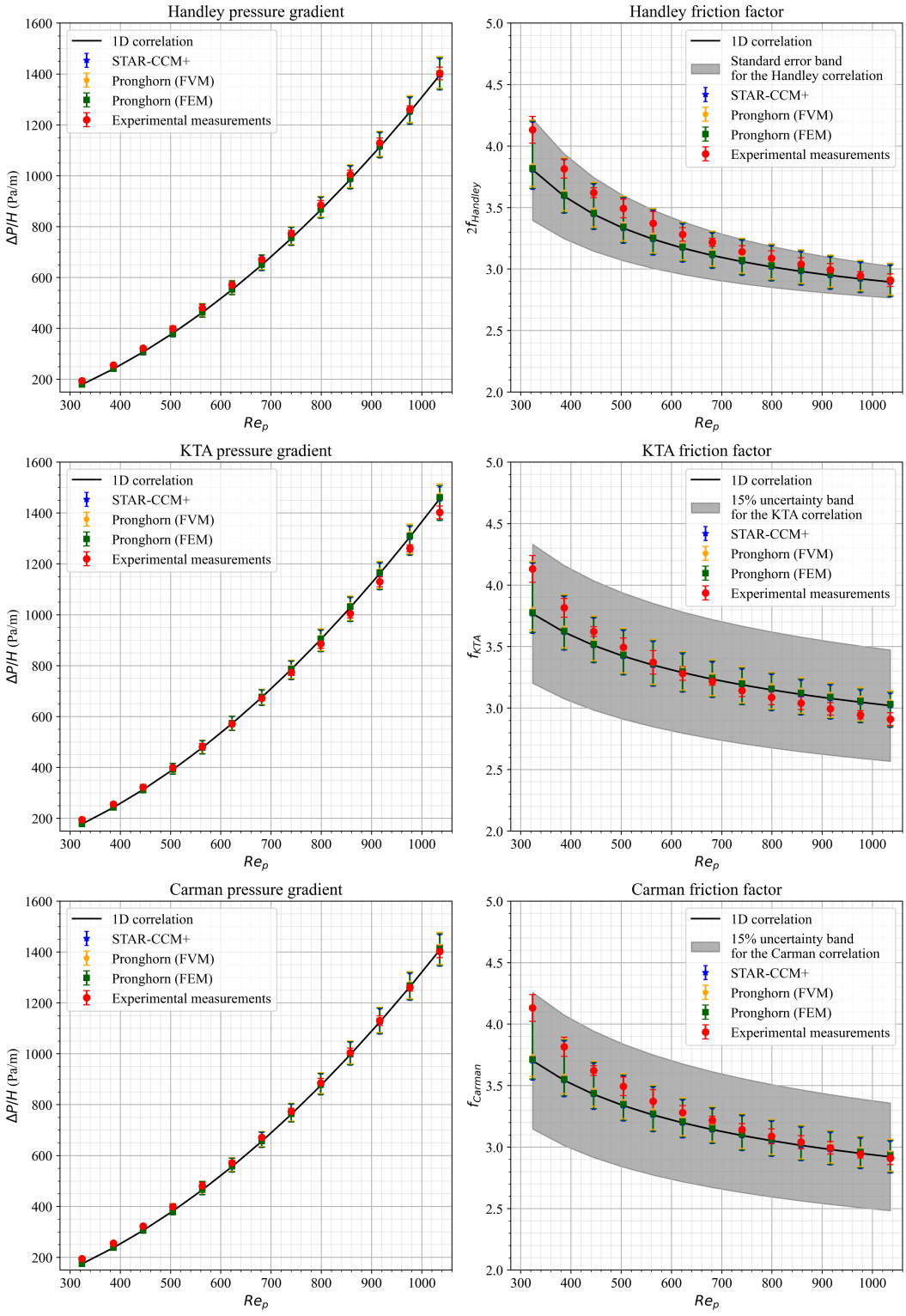

Figure 5.39. Pressure gradient and friction factor for the Handley, KTA, and Carman correlations.

simulations with the pressure drop correlations in Figure 5.38. In Table 5.11, assuming that both the experimental and simulation data distributions are probabilistic and Gaussian (by considering the numerical and input uncertainties only), the average Kullback-Leibler divergences are within the tolerance in Table 2.15 for $Re_p \geq \sim$800 using the Handley and Carman models. The averages of the symmetrized Kullback-Leibler divergence for the same Re_p range are close to the tolerance value of 1. Additionally, the $\bar{d}_{KS}$ and $\bar{d}_{area}$ metrics use the discrepancies between the CDFs [156]. While $\bar{d}_{KS}$ only considers the vertical differences, $\bar{d}_{area}$ also accounts for the horizontal differences. The zero $\bar{d}_{KS}$ or $\bar{d}_{area}$ indicates the agreement between the CDFs from the experiments and simulations. Figure 5.40 shows an instance of the CDFs of the experimental pressure drop and STAR-CCM+ simulation output given the Carman function. The pressure drops at different particle Reynolds numbers produce different areas between the CDFs, represented as the red shaded areas in Figure 5.40. Including the Handley, KTA, and Carman functions, other correlations in Figure 5.38 achieved the relatively low average normalized area metrics (less than or close to 5%) within the entire Re_p range used for the experiments. Figure 5.41 also verifies the agreement of the dimensionless pressure drop and axial velocity profile between the Pronghorn FEM, Pronghorn FVM, and STAR-CCM+ porous media models.

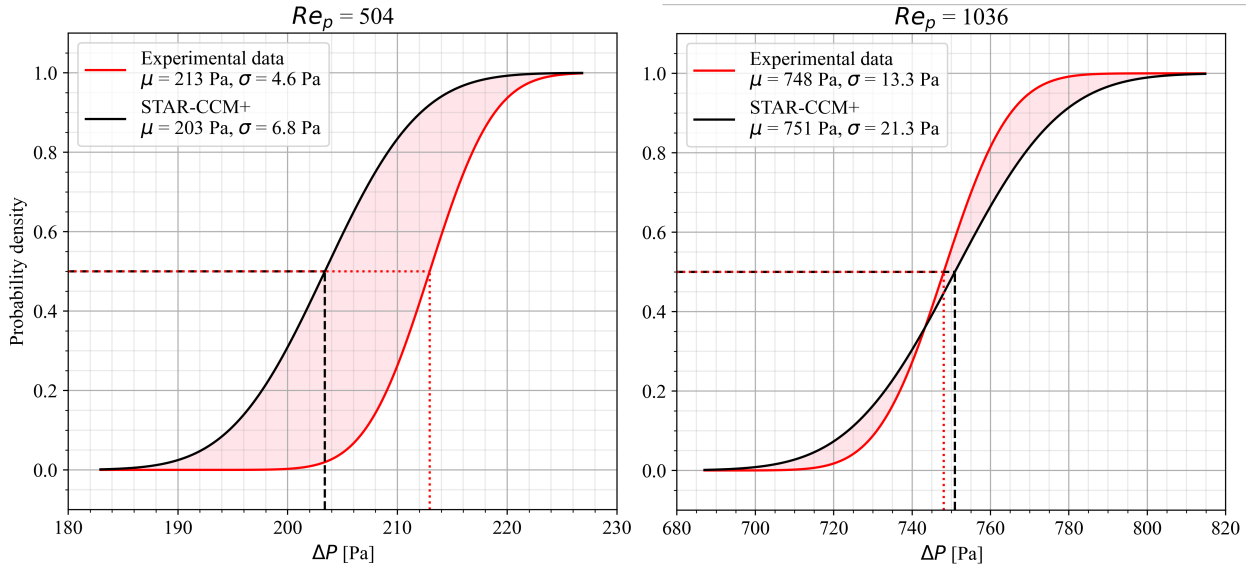

Figure 5.40. Quantification of the vertical and horizontal discrepancies between the CDFs from the experiments and simulations (μ = mean, σ = SD).

Table 5.11. Validation metrics for the Handley and Carman pressure drop functions, provided that the experimental and simulation data are probabilistic.

Validation metrics/ model	Handley			Carman		
	Pronghorn FEM	Pronghorn FVM	STAR-CCM+	Pronghorn FEM	Pronghorn FVM	STAR-CCM+
Average Kullback-Leibler divergence[†]	0.369	0.3	0.429	0.282	0.283	0.288
Average of the symmetrized Kullback-Leibler divergence[†]	1.37	1.1	1.58	1.07	1.12	1.06
Average Hellinger metric[†,‡]	0.349	0.314	0.375	0.305	0.306	0.308
Average Kolmogorov-Smirnov[†]	0.306	0.248	0.361	0.205	0.211	0.233
Average normalized area metric[§]	0.0318	0.0278	0.0344	0.0316	0.029	0.0332

[†]The validation metrics were obtained within or close to the tolerances for $Re_p \geq \sim$800.
[‡]The zero value of H_{ave} represents the exact agreement between the experimental and simulation results [156].
[§]The average normalized area metrics were obtained from Re_p equal to 324–1036.

Next, the pressure drop or friction factor with the relatively high particle Reynolds number ($Re_p \geq 800$) was improved by utilizing the volume-averaged radial porosity function, Equation 5.1. Applying an oscillatory porosity function directly in the porous media simulations would not improve the pressure drop results. This is because the variable porosity is the micro-heterogeneous information, and the pressure drop correlations are generally developed based on the superficial velocity accounting for the average bed porosity. The macroscopic quantities, defined within at least the d_p^2 surface or d_p^3 volume as the REV, are necessary for the valid macroscopic approach. Figure 5.42 describes how the new oscillatory function or its volume-averaged porosity was applied in the porous bed region for the Pronghorn FEM and STAR-CCM+ simulations. The dimensionless axial velocities and the corresponding porosity profiles from the center of the porous bed to the wall are represented in Figure 5.43. The magnitude of the axial velocity increases as the porosity increases. With the new oscillatory porosity function, the agreement in the dimensionless axial velocities between the Pronghorn FEM and 3D STAR-CCM+ models is acceptable with less than the 5% average relative difference. Herein, the numerical errors obtained by the GCI method were applied as the error bars. The Pronghorn FEM mesh was refined by a factor of 2 compared to the original mesh described in Section 3.3,

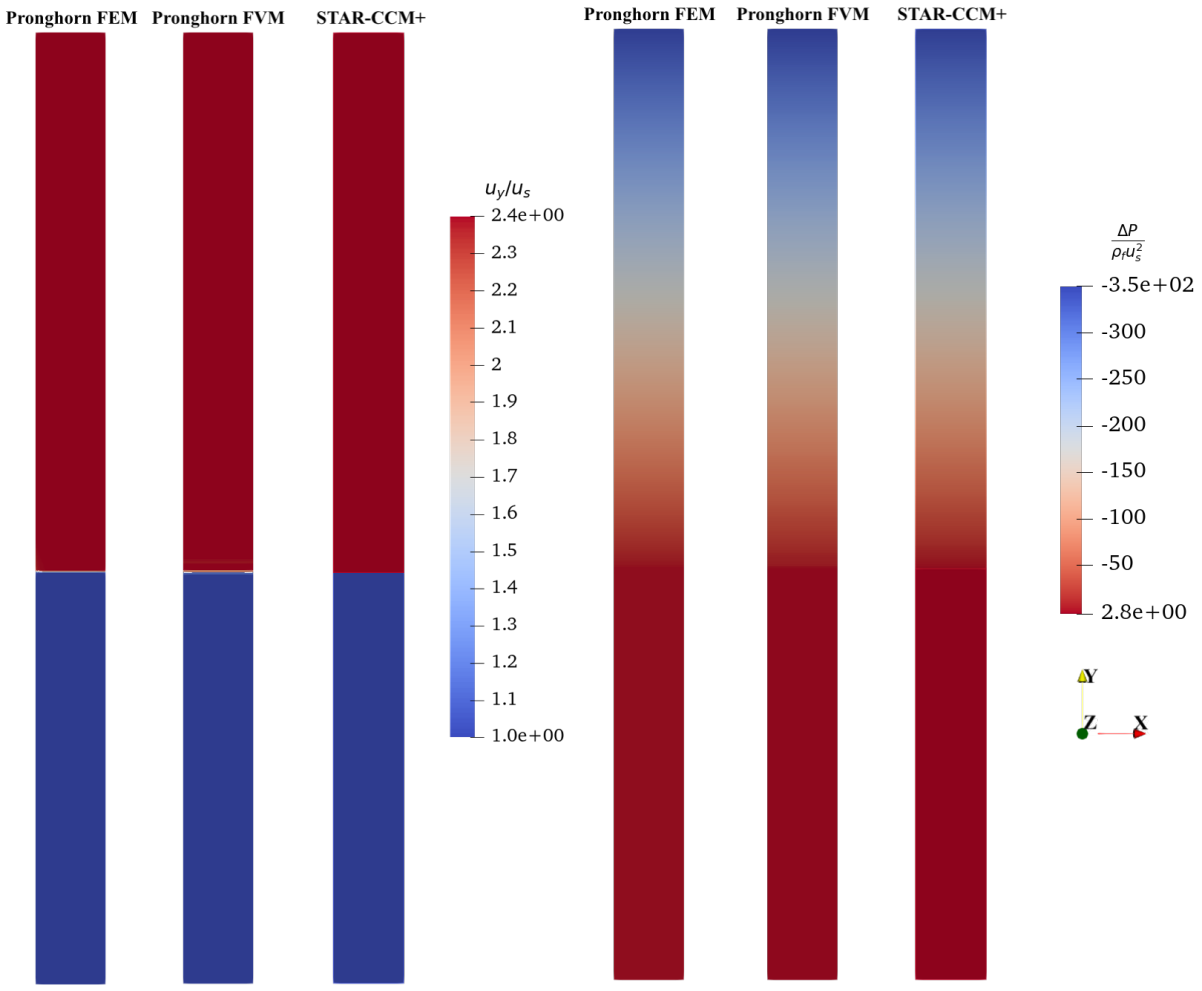

Figure 5.41. Carman porous media simulations performed by Pronghorn FEM, Pronghorn FVM, and STAR-CCM+ for $Re_p = \sim$800.

and this brought the GCIs under 5% with the oscillatory porosity. Meanwhile, other meshes were kept the same as presented in Section 3.3 for the GCIs less than 5%. The trend of the oscillatory axial velocities in Figure 5.43 is similar to the data provided in [9].

The pressure drop and corresponding friction factor deteriorated significantly by applying the variable porosity straight in Figure 5.44. The average bed porosities for all simulations are less than 0.7% different compared to the experimental reference porosity. Applying the volume-averaged oscillatory porosity within two annular cylinders and the solid cylinder in the middle of the porous bed overall moved the pressure drop or friction factor closer to the experimental measurements, compared to the values obtained by the simulations with one average bed porosity used for the whole porous bed. Three sectored volumes were

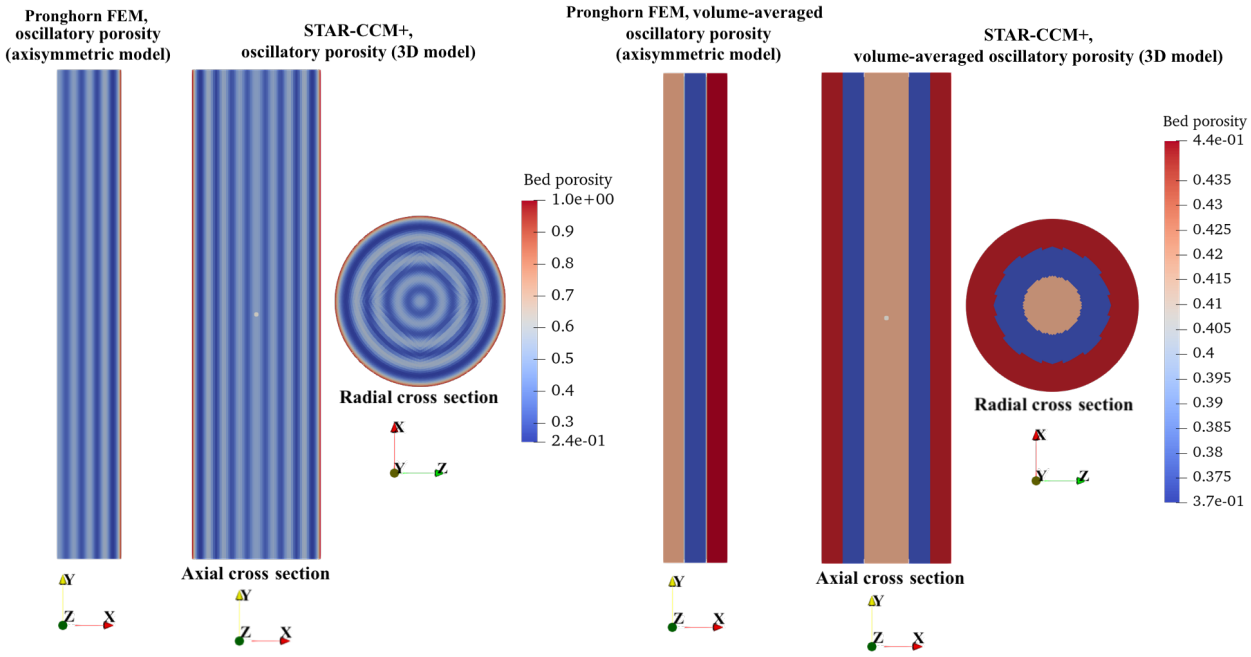

Figure 5.42. Variable porosity or volume-averaged porosity profile applied in the Pronghorn FEM and STAR-CCM+ simulations.

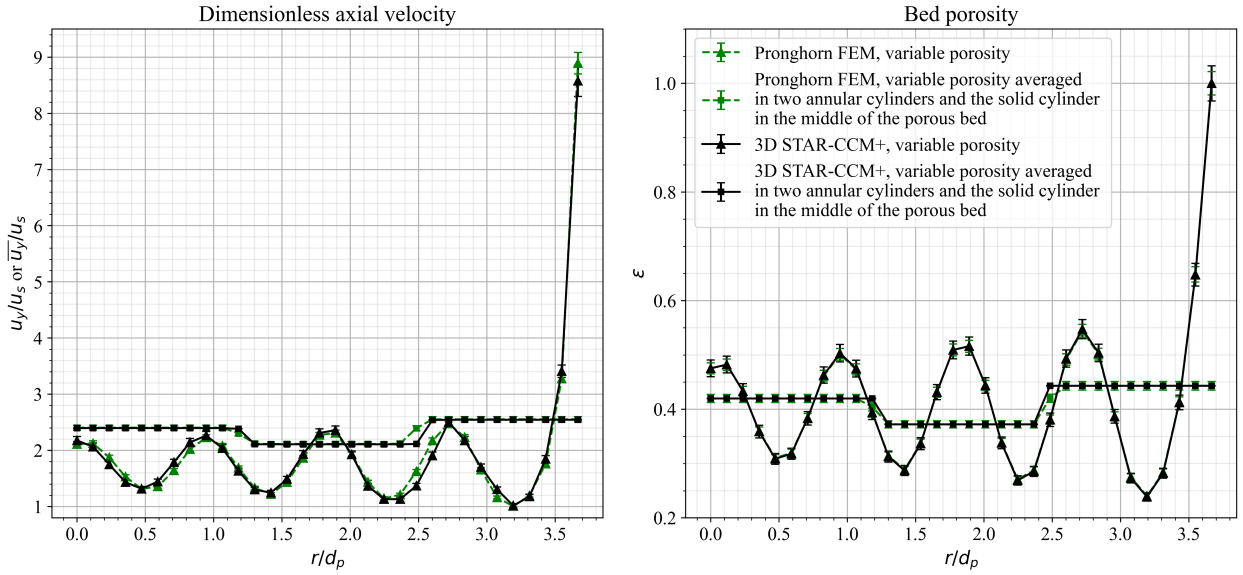

Figure 5.43. Dimensionless axial velocities and the corresponding porosity profiles from the center of the bed to the wall, given the new oscillatory porosity function from Equation 5.1 or its volume-averaged porosity profile with the Brauer function.

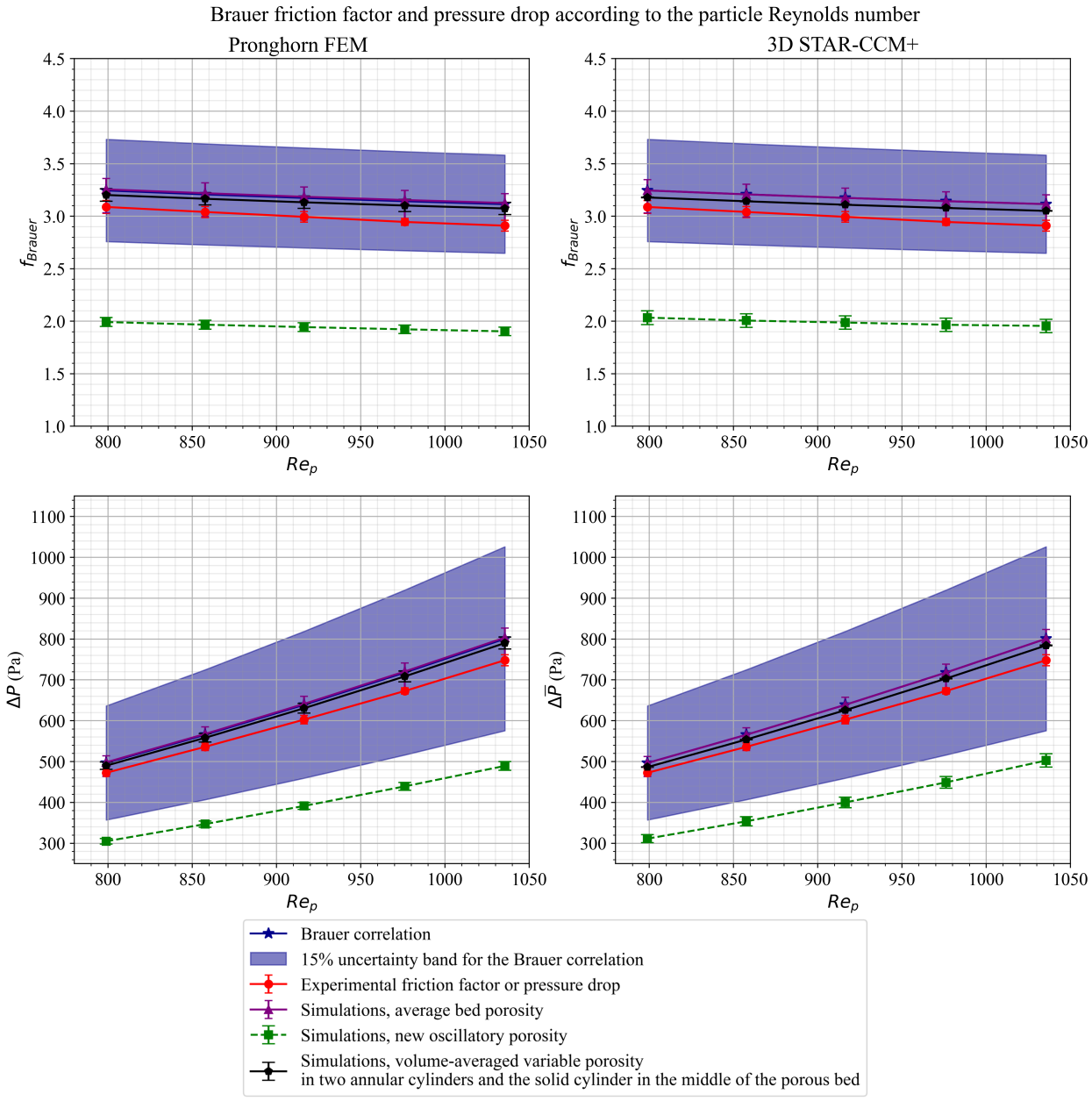

Figure 5.44. Brauer friction factor and pressure drop for $Re_p \geq \sim 800$.

chosen because the $1.22d_p$ thickness of the annular cylinder or radius of the solid cylinder located in the middle of the bed is larger than the d_p representative elementary length. Figure 5.45 verifies that the detailed porosity information in the REV deteriorated the pressure drop predicted by porous media simulations. When using up to three sectors, the pressure drop decreased with the volume-averaged oscillatory porosity. However, with four sectored volumes, the pressure drop increased or moved back close to the value obtained

with the overall average bed porosity. Although the pressure drop improvement might not be significant using the volume-averaged variable porosity within sectored volumes larger than the REV, this approach has the potential to improve the pressure drop or provide more detailed axial velocity profiles in nuclear reactors. They have much higher aspect ratios than the current pebble bed experiments, which helps in computing the volume-averaged quantities in many REVs. Wall effects can be considered using this method by having the relatively larger volume-averaged porosity near walls than the average bed porosity. Figure 5.46 describes the dimensionless axial velocity averaged in the whole pebble bed, and this quantity agrees well between the Pronghorn and 3D STAR-CCM+ models. The dimensionless volume-averaged axial velocity obtained by the Pronghorn FEM model with the oscillatory porosity is $\sim$17% different compared to the model with the average bed porosity. Figure 5.43, Figure 5.44, Figure 5.45, and Figure 5.46 were obtained with the Brauer function, and a similar trend was also achieved with the Jones and Krier function. Due to the limited space available, only the simulation results using the Brauer function are described.

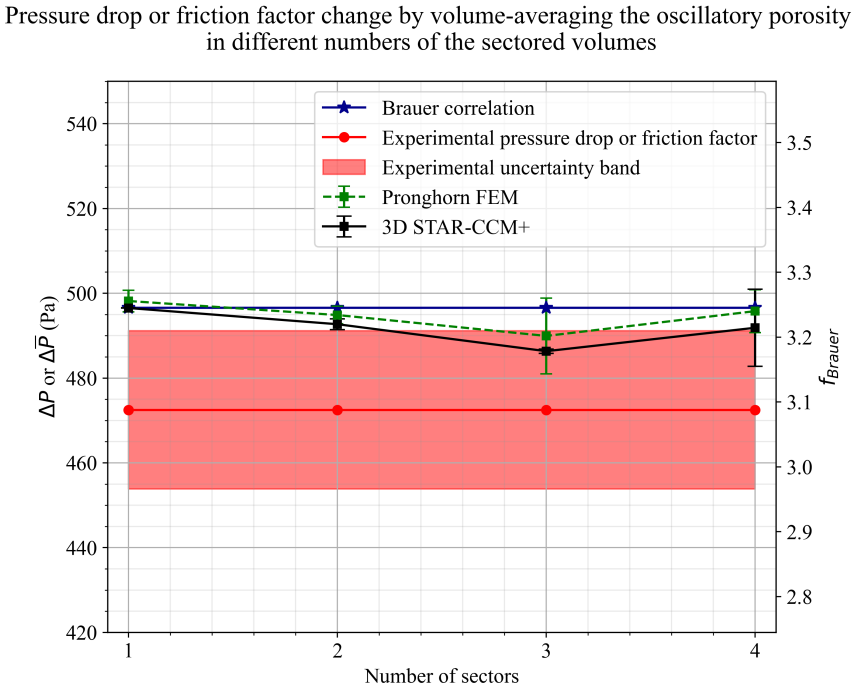

Figure 5.45. Pressure drop or friction factor change with respect to the number of sectored volumes applied for volume-averaging the oscillatory porosity ($Re_p = \sim$800).

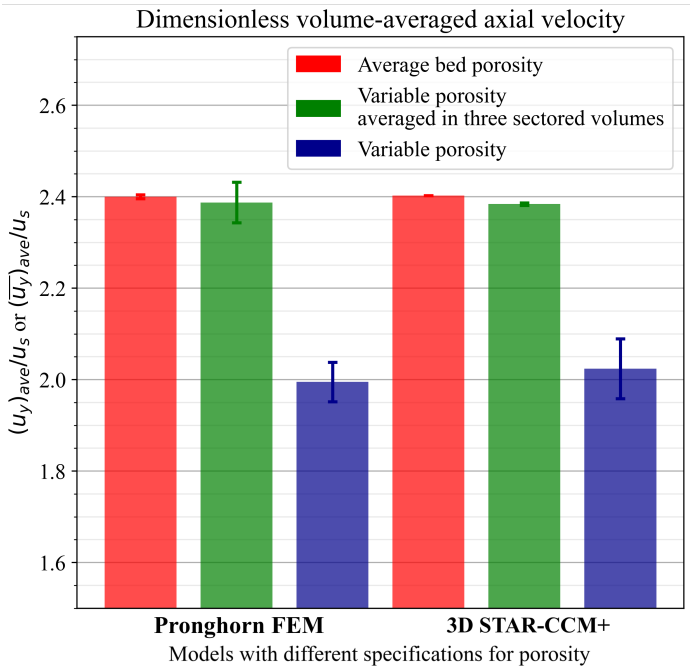

Figure 5.46. Comparison of the dimensionless volume-averaged axial velocity in the whole porous bed between the Pronghorn FEM and 3D STAR-CCM+ models ($Re_p \geq 800$).

5.3.6 Turbulence Modeling with Explicit Meshing

The porous media simulations cannot provide the details of the complex velocity or vorticity profiles developed around pebbles because the macroscopic properties, such as the average bed porosity and superficial velocity, are used to homogenize the micro-heterogeneity. It is still questionable if the volume- or surface-averaged velocities from the turbulence models or high-fidelity PIV data are comparable with those values from the porous media simulations. First, the GCI study was performed with a refinement ratio of 2 to ensure that fine meshes bring at least a 95% confidence level for the computed quantities of interest, the dimensionless volume-averaged axial velocity and pressure gradient in the porous bed in Figure 5.47. The GCI_{21}s were calculated as 0.11% and 1.7% for the dimensionless volume-averaged axial velocity and pressure gradient, respectively. Figure 5.47 only shows the GCI study for the SST $k-\omega$ simulation results with the $15d_p$ VGSTUDIO reconstructed bed height. In Figure 5.48, Figure 5.50, and Figure 5.51, the error bars were determined by taking the GCI study for each turbulence model with the different specific bed height and reconstructed geometry.

The pressure gradient and friction factor obtained by the realizable two-layer $k-\varepsilon$ and SST $k-\omega$ models

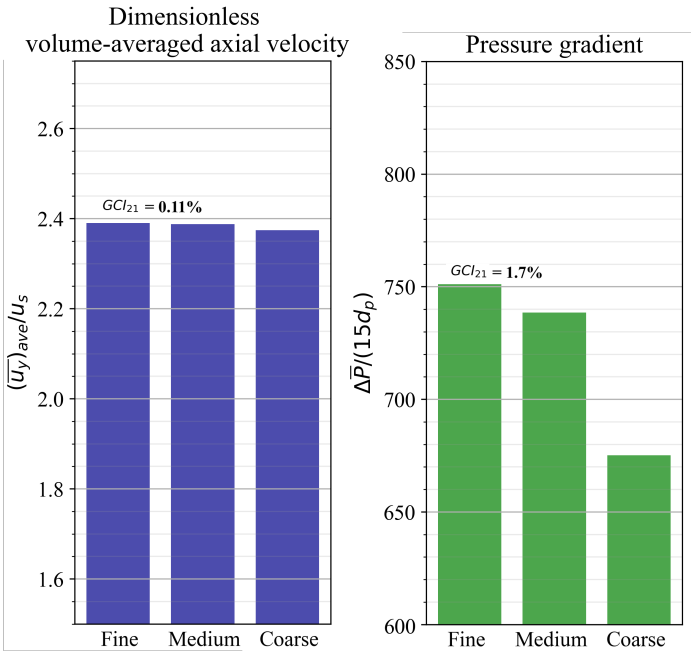

Figure 5.47. Grid sensitivity analysis with the dimensionless volume-averaged axial velocity and pressure gradient in the porous bed. The SST $k-\omega$ simulation results are with the $15d_p$ VGSTUDIO reconstructed bed height.

with the MATLAB and VGSTUDIO reconstructed geometries are within or close to the 15% uncertainty band for the Carman function in Figure 5.48. The similar trends in the pressure gradient and friction factor were obtained by the realizable two-layer $k-\varepsilon$ and SST $k-\omega$ models, and increasing the bed height from d_p to $15d_p$ did not necessarily improve these quantities but kept a similar accuracy level. In Figure 5.38, specifically for $Re_p = \sim$800, the Pronghorn and STAR-CCM+ axisymmetric simulation results and the Carman function are all within $\sim$1%. Therefore, the porous media models' pressure gradient and friction factor are also comparable with those values from the turbulence models. With the d_p bed height, the radial porosity oscillation locations match well with the reference values in Section 5.3.2. Consequently, the 7% average relative difference of radial porosity did not add many discrepancies in the pressure gradient or friction factor. Figure 5.49 describes the axial cross sections of the dimensionless time-averaged pressure drop obtained by the SST $k-\omega$ model for the VGSTUDIO reconstructed geometry given the different bed heights. The gradual pressure drop seems to be in good agreement between all four bed heights, except the flow at the inlet of the porous bed had entrance effects.

For the validation purposes of the velocities in the pebble bed near the cylindrical wall, the realizable

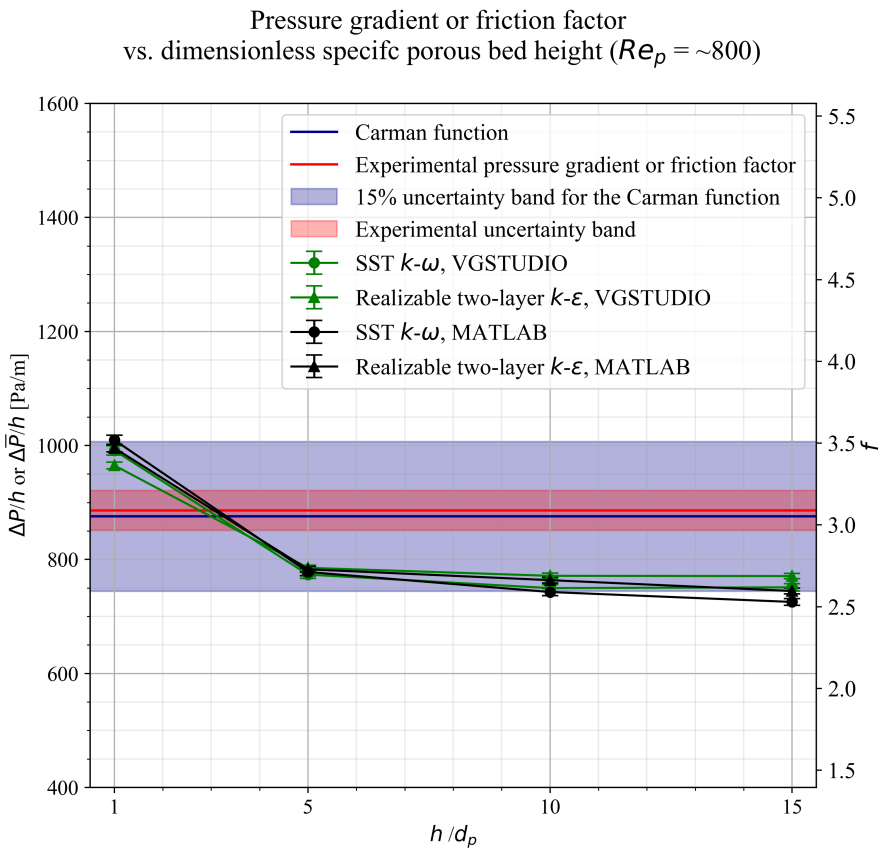

Figure 5.48. Pressure gradient or friction factor obtained by the realizable two-layer $k-\varepsilon$ and SST $k-\omega$ models for the MATLAB and VGSTUDIO reconstructed geometries ($Re_p = \sim$800).

two-layer $k-\varepsilon$ and SST $k-\omega$ models provided the axial velocity data averaged within the PIV window, which is the $10d_p^2$ surface area of the pebble bed from [180]. With $Re_p = \sim$800, the relative difference between the dimensionless surface-averaged axial velocity from the SST $k-\omega$ model and the value from the PIV data is 4% with the VGSTUDIO reconstructed geometry in Figure 5.50. The realizable two-layer $k-\varepsilon$ model provided the 0.4% relative difference of the surface-averaged axial velocity in the PIV window. The Carman porous media simulation with the porosity volume-averaged in three different sectors performed better than other Pronghorn simulations in Figure 5.50. The direct implementation of the oscillatory porosity decreased the axial velocity averaged in the PIV window significantly by ~19%. Furthermore, Figure 5.51 shows the axial velocities volume-averaged in the fluid region of the porous bed obtained by the turbulence models. They are reasonable for all four different bed heights because the maximum rela-

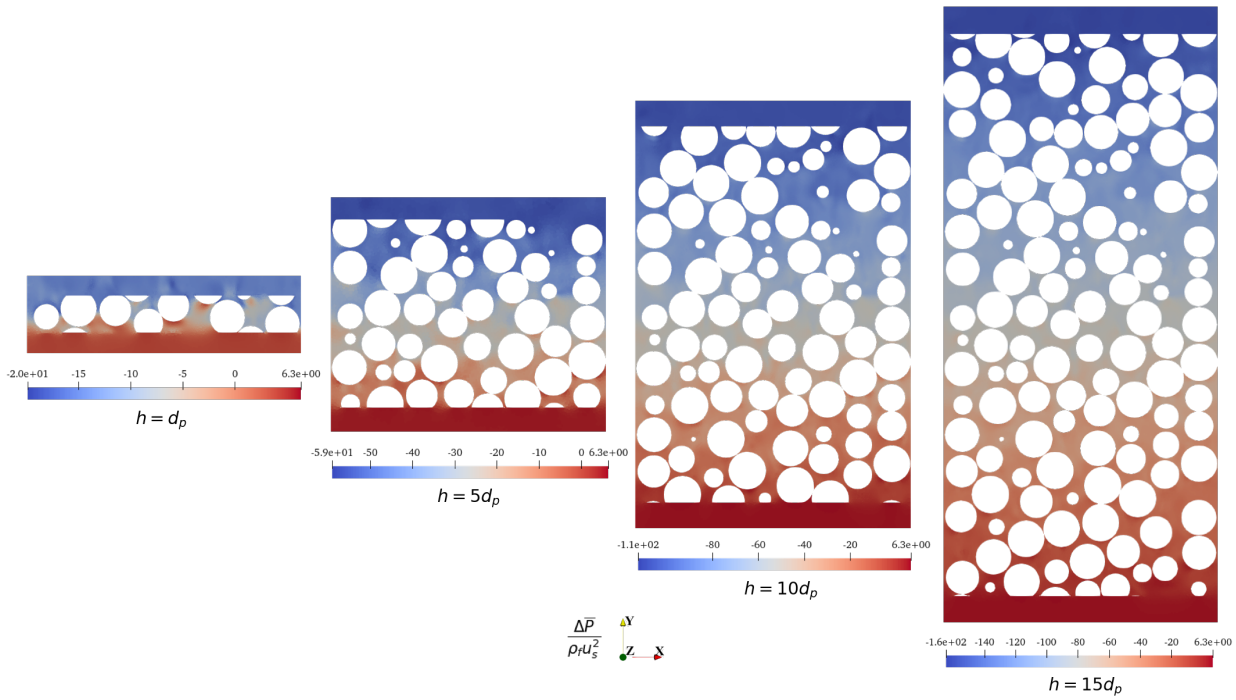

Figure 5.49. Dimensionless time-averaged pressure drop by the SST $k-\omega$ model for the VGSTUDIO reconstructed geometry. Four different specific bed heights are provided with $Re_p = \sim$800.

tive difference compared to the reference data is 2.75%. In Figure 5.52, Figure 5.53, and Figure 5.54, the detailed velocity profiles from the SST $k-\omega$ model verify that the vertical flow through the porous bed is much higher compared to the lateral flow. A few small eddies may have less impact on the volume- or surface-averaged axial velocities due to the dominant axial flow in the porous bed. The dimensionless time-averaged axial velocity and turbulent kinetic energy profiles in Figure 5.52 and Figure 5.55 follow the similar trend to those in [185]. Lastly, the turbulent kinetic energy averaged within the PIV window is about 0.00159 m^2/s^2 with the realizable two-layer $k-\varepsilon$ model, and it is different from 0.0024 m^2/s^2, obtained from the PIV data. It could be due to the uncertainties propagated for the PIV measurements or the limitations for two-equation turbulence models used for the pebble bed experiments. Nevertheless, overall the pressure gradients and averaged axial velocities are in reasonable agreement between the turbulence models, porous media simulations, and the PIV data.

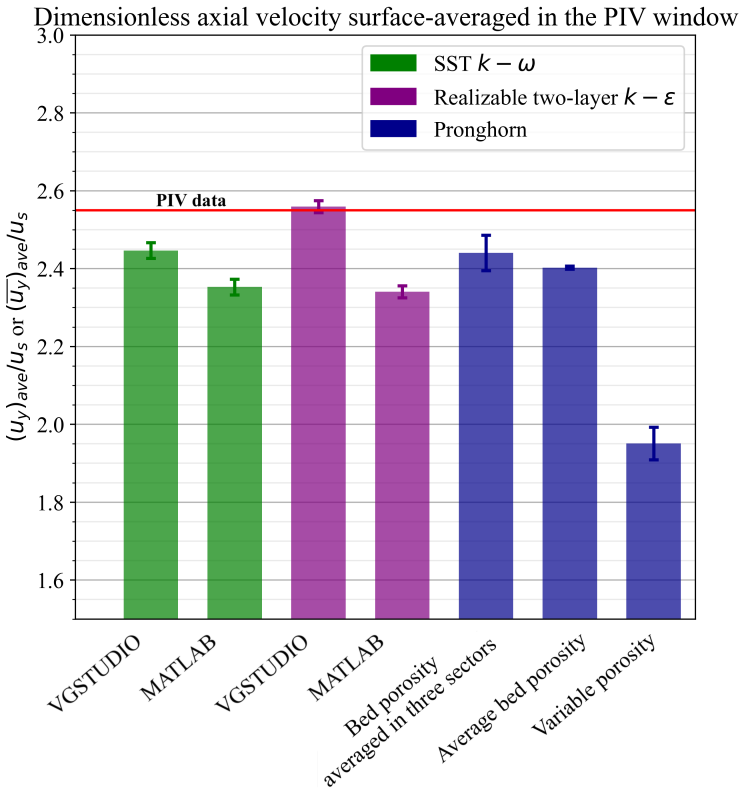

Figure 5.50. Comparison of the dimensionless axial velocities surface-averaged in the PIV window. The Pronghorn porous media simulations are based on the Carman function.

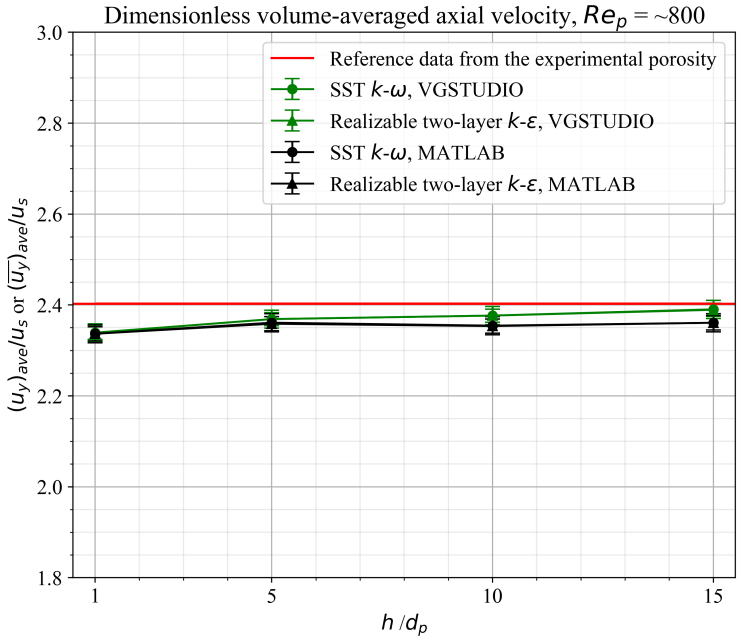

Figure 5.51. Dimensionless volume-averaged axial velocity in the porous bed according to the specific bed height.

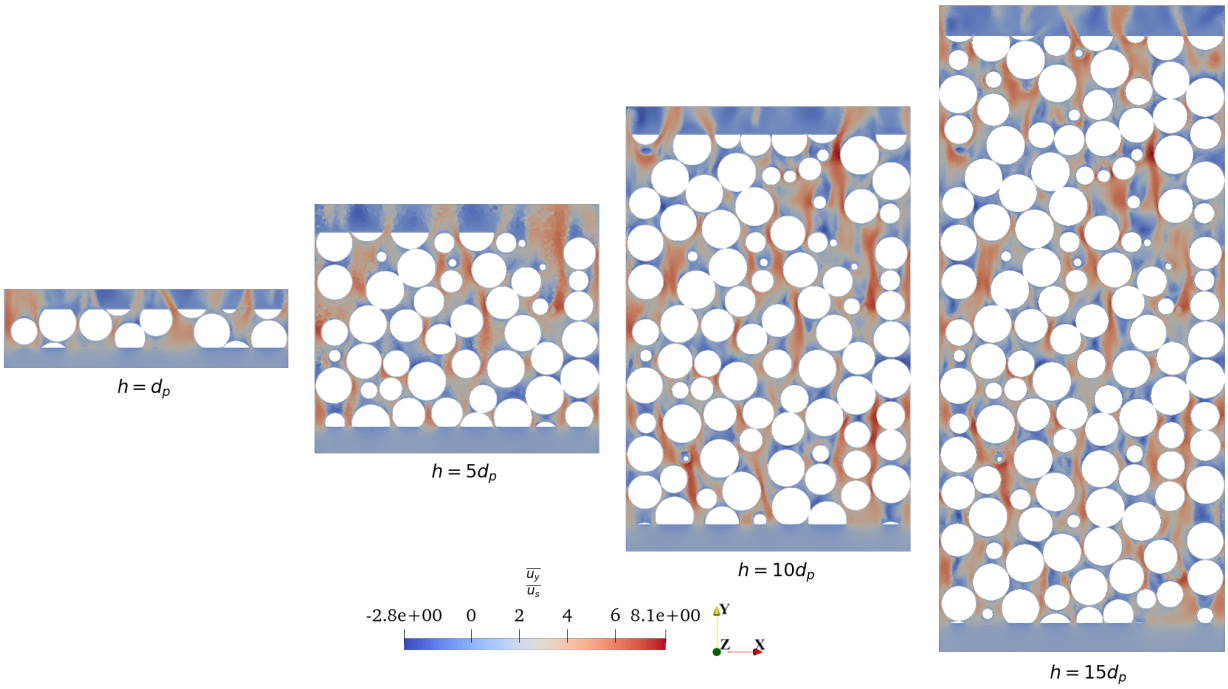

Figure 5.52. Dimensionless time-averaged axial velocity by the SST $k - \omega$ model for the VGSTUDIO reconstructed geometry. Four different specific bed heights are provided with $Re_p = \sim$800.

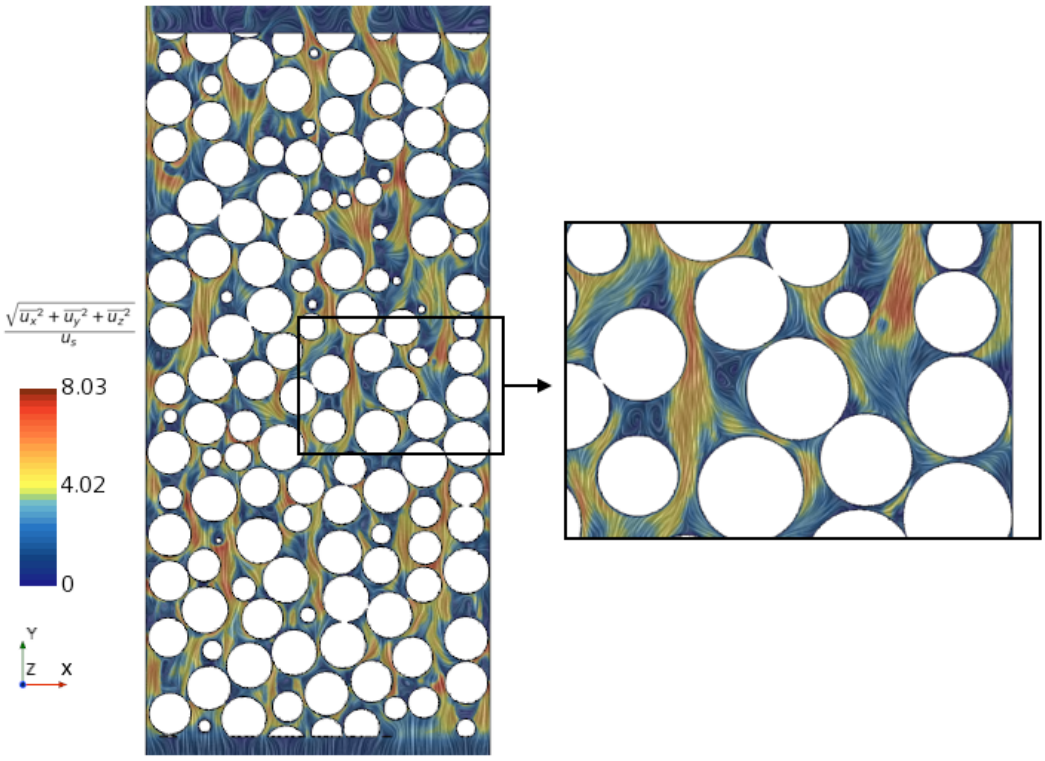

Figure 5.53. Visualized vector field by the line integral convolution. The SST $k - \omega$ model for the VGSTUDIO reconstructed geometry is shown with the $15d_p$ bed height.

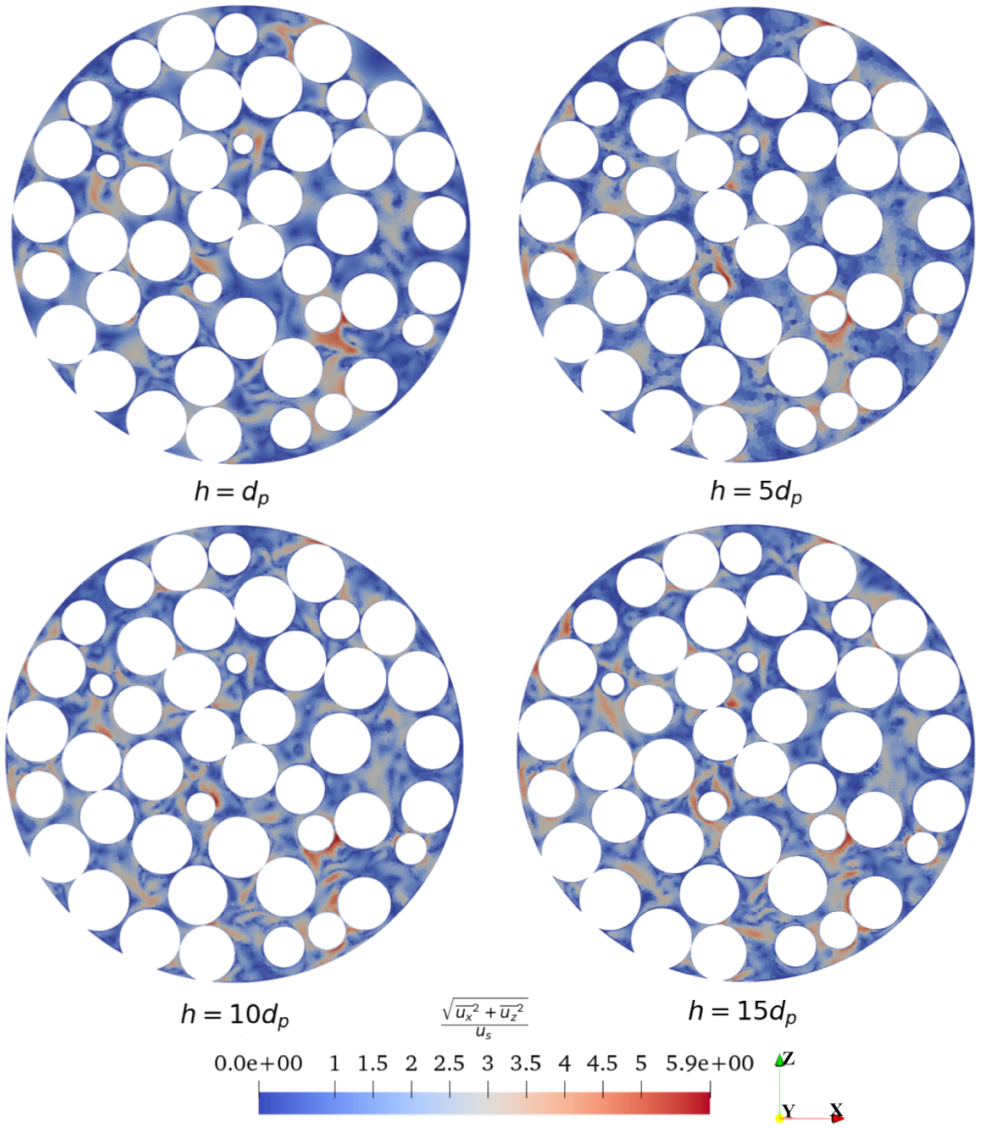

Figure 5.54. Dimensionless time-averaged cross-flow velocity by the SST $k - \omega$ model for the VGSTUDIO reconstructed geometry. Four different specific bed heights are used with $Re_p = \sim$800.

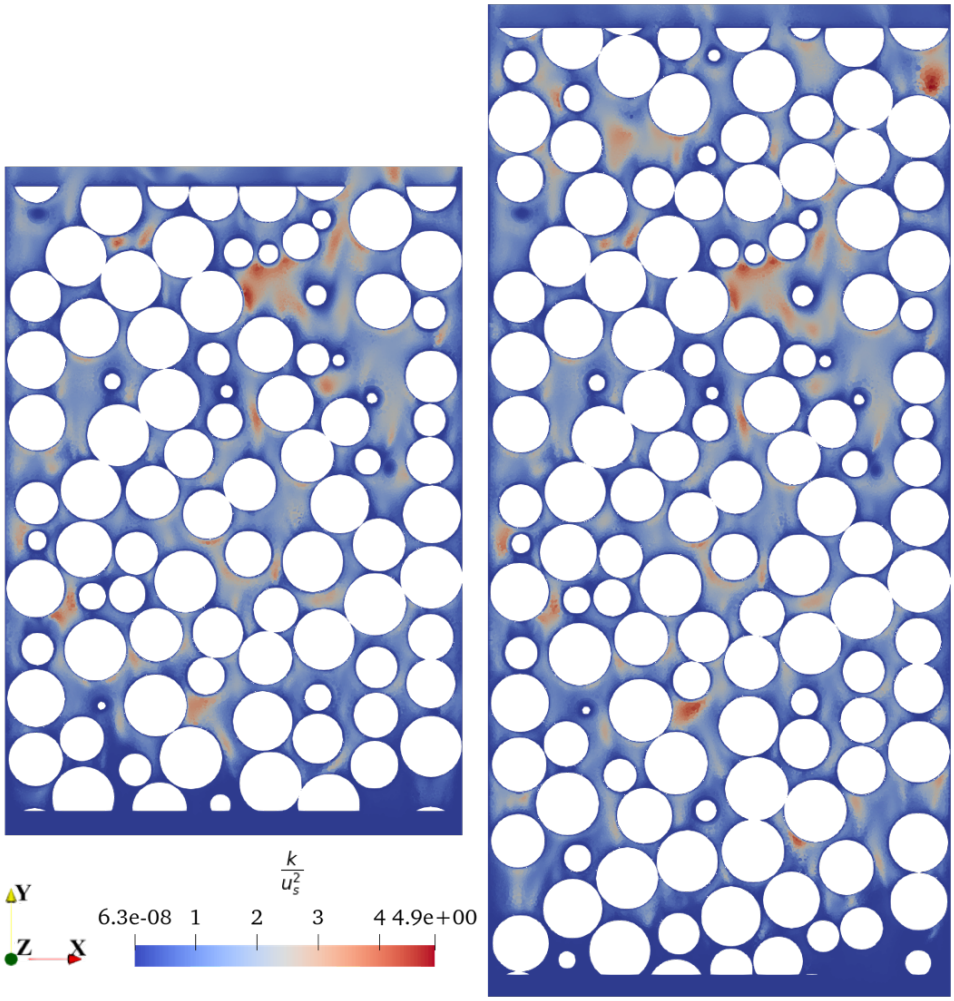

Figure 5.55. Dimensionless turbulent kinetic energy by the realizable two-layer $k-\varepsilon$ model for the VGSTUDIO reconstructed geometry. $Re_p = \sim$800 with the $10d_p$ and $15d_p$ bed heights.

5.4 Facility Scaling

Several PBR prototypes were examined to optimize the experimental installations in Table 5.12. Small modular reactors, such as the pebble bed modular reactor (PBMR 400), MIT PBR, and HTR-PM, are the HTGR generation IV conceptual designs developed partially based on the earlier experimental and commercial scale reactors. While the Xe-100 reactor is of interest since it is the advanced reactor design that is most supported in the U.S., its detailed design specifications are not provided to the public. Therefore, the similar modular reactor, HTR-PM, was used as the prototype for building the scaled-down facility.

Geometric scaling ratios were chosen by considering the feasibility of the experimental setups; the operating temperature and pressure ranges, total power of the heating element, installation cost, space availability, etc. First, the characteristic length scaling ratio, which is the ratio between the model pebble diameter and prototypic facility pebble diameter, was initially calculated as 1/0.8197. Integral similarity relations similar to [173, 177, 186] in Table 5.13 were used to calculate the scaling ratios in Table 5.14 and the operating conditions for the model in Table 5.15. The effective solid thermal conductivity scaling ratio derived from the correlations in Section 2.8 is different from the value obtained by the modified Bi integral similarity relation. It would be adjusted accordingly when the fluid and solid materials are determined for future pressure drop and temperature measurements including the PIV study.

Table 5.12. PBR prototypes [4, 187–198].

	Experimental reactor		Commercial scale reactor	Modular reactor		
Reactor†	AVR	HTR-10	THTR	PBMR	MIT PBR	HTR-PM
Reactor core height (m)	2.8	1.97	6	∼11	10	11
Reactor core diameter (m)	3	1.8	5.6	3.7	3.5	3
Upper cavity height (m)	-	0.417	-	0.785	-	-
Pebble sphere diameter (mm)	60	60	60	30	60	60
Central reflector diameter (m)	-	-	-	2	-	-
Thermal power (MW(t))	46	10	750	400	250	250
Average power density (MW/m^3)	2.6	2	6	4.8	3.54	$\sim$ 3.22
Reactor inlet temperature (^oC)	270	250	250	500	520	250
Reactor outlet temperature (^oC)	950	700	750	900	900	750
Primary coolant pressure (MPa)	1.1	3	4	9	8	7
Primary coolant flow rate (kg/s)	13	4.32	51.2	185.31	120	96
Average bed porosity	-	0.39	-	0.39	0.39	0.39
Primary coolant	He	He	He	He	He	He
Operational years	1967–1988	2000–present	1985–1991	-	-	-

†Arbeitsgemeinschaft versuchsreaktor (AVR), high temperature gas-cooled reactor 10 (HTR-10), and thorium hochtemperatur reaktor (THTR).

Table 5.13. Integral similarity conditions.

Parameter	Integral similarity relation
Axial/radial length scale	H_R/D_R
Pebble diameter length scale	$(d_p)_R$
Pebble bed core cross-sectional area	$(a_c)_R = D_R^2$
Pebble bed core volume	$(V_{core})_R = (a_c)_R H_R = D_R^2 H_R$
Power density	$(q'''_{core})_R = (\rho_f)_R (d_p)_R^{1/2} P_R^{2/3}$ (forced/natural convection)
Reactor power	$(Q_{core})_R = (q'''_{core})_R (V_{core})_R = (\rho_f)_R (d_p)_R^{1/2} P_R^{2/3} D_R^2 H_R$ (forced/natural convection)
Characteristic velocity	$(u_s)_R$ or $u_R = ((d_p)_R)^{1/2}$ (forced/natural convection)
Temperature rise	$\Delta T_R = (d_p)_R P_R^{2/3}$ (forced/natural convection)
Mass flow rate	$(\dot{m})_R = (\rho_f)_R \sqrt{(d_p)_R} D_R^2$ (forced convection)
Pressure drop	$\Delta P_R = \left[\frac{\rho_f u_s^2 H}{d_p}\right]_R$ (forced convection)
Solid-fluid convective heat transfer coefficient	$\alpha_R = \frac{1}{\sqrt{(d_p)_R}} (\rho_f)_R$ (forced/natural convection)
Effective fluid thermal conductivity	$(\kappa_f)_R = \mu_R$ (forced/natural convection)
Effective solid thermal conductivity	$(\kappa_s)_R = (\rho_f)_R (d_p)_R^{3/2}$ (forced/natural convection)

Table 5.14. Scaling ratios.

Parameter	Scaling ratio
Axial length scale	1:15
Radial length scale	1:2.5
Pebble diameter length scale	1:0.8197
Pebble bed core cross-sectional area	1:6.25
Pebble bed core volume	1:93.75
Power density	1:3.753
Reactor power	1:351.9
Characteristic velocity	1:0.9054
Mass flow rate	1:10.38
Pressure drop	1:27.51
Solid-fluid convective heat transfer coefficient	
1) St similarity	1:2.026
2) KTA Nu correlation	1:2.179
3) Gunn Nu correlation	1:2.22
Effective fluid thermal conductivity	
1) Pr similarity	1:1.361
2) Correlation (εk_f)	1:1.56
Effective solid thermal conductivity	
1) Modified Bi similarity	1:1.361
1) Breitbach and Barthels, Zehner and Schlünder, Chan and Tien correlations	1:10.58
2) Tsotsas, Zehner and Schlünder, Chan and Tien correlations	1:7.618

Table 5.15. Operating conditions for the engineering-scale PBR facility.

Operating condition	
Reactor core height (m)	0.7333
Reactor core diameter (m)	1.2
Reactor core volume (m^3)	0.8294
Upper cavity height (m)	-
Pebble sphere diameter (mm)	73.2
Overall thermal power (MW(t))	0.7105
Average power density (MW/m^3)	0.8567
Average fuel power density (MW/m^3)	1.404
Thermal power generated by an individual pebble (W)	288.4
Reactor inlet temperature (^oC)	9.229
Reactor outlet temperature (^oC)	279.1
Primary coolant pressure (MPa)	2.06
Primary coolant flow rate (kg/s)	9.25
Average bed porosity	0.39
Primary coolant properties	Helium $\rho_f = 3.491$ kg/m^3 $\mu = 1.901 \times 10^{-5}$ Pa·s $k_f = 0.1484$ W/(m·K)
Temperature rise (^oC)	269.9
Interstitial velocity in the porous bed (m/s)	6.007
Superficial velocity in the porous bed (m/s)	2.343
Number of pebbles in the bed	$\sim$2463

6. CONCLUSION*

The V&V of Pronghorn is achieved by predicting the fluid velocity, pressure, or temperature in the pebble bed experiments. Multiple pressure drop correlations (using the Darcy-Forchheimer formation) in the Pronghorn compressible/incompressible Euler/Navier-Stokes equations can predict the fluid velocity and pressure drop in the porous bed within the uncertainty bands for various type of HTGRs, provided the specific Reynolds number, aspect ratio, and porosity ranges. The Pronghorn energy equations with several correlations for the solid-fluid convective heat transfer coefficient and effective thermal conductivities can also estimate fluid and solid temperatures in the porous bed. This helps in optimizing the HTGR designs by observing the fluid motion and heat transfer in both normal operation and accident scenarios in advance. The following highlights the contributions for each research subject and provides the recommendations on future work.

6.1 Pronghorn Fully Compressible Equation Set Validation against SANA Open Plenum Experiments

Legacy Pronghorn, modern Pronghorn, and STAR-CCM+ compressible Euler porous media model agree well on fluid and solid temperatures in the pebble bed. The discrepancy between the experimental data and modern Pronghorn result is the smallest among the compared models near the heater rod and is about 75.5^{o}K at the half bed height. There are multiple possible causes of why the simulation results and experimental measurement do not agree better: 1) there is no information of fluid mass in the closed SANA system on the benchmark specifications, although the mass affects the heat transfer in the experiment significantly; 2) a discrepancy between the models and the as-built facility; and 3) measurement errors. The flow pattern in the plenum is poorly predicted by legacy Pronghorn; however, this does not lead to a poor prediction of temperatures in the bed, indicating a limited effect of plenum flow patterns on the bed temperature distribution.

*Parts of this chapter are adapted with permission from [11, 12].

6.2 Validation of Pronghorn Pressure Drop Correlations against Pebble Bed Experiments

The Pronghorn (both the FEM and FVM) pressure drop estimation using the compressible/incompressible Navier-Stokes equations agrees well with the STAR-CCM+ simulation results and 1D correlations, including the experimental pressure drop measurements. The Reynolds number varies from the laminar to turbulent regime given different specific aspect ratios. The precise porosity function has more impact on the pressure drop estimation than previous efforts by considering the aspect ratio for the near-wall effects.

The V&V of Pronghorn Navier-Stokes equations is successfully accomplished by providing the pressure gradients and averaged axial velocities from porous media simulations, which are comparable with the values from the realizable two-layer $k-\varepsilon$ model, SST $k-\omega$ model, and the experimental data (pressure drop and PIV measurements). The average bed and radial porosities for the pebble bed experiments are accurate such that the consequent pressure drop and averaged axial velocities agree well with the experimental reference values. The Carman-type pressure drop correlations implemented in both Pronghorn and STAR-CCM+ porous media models generally estimate the pressure drop well in pebble bed experiments with the incompressible fluid. Volume-averaging the variable porosity in multiple sectors improves the pressure drop and axial velocity averaged in the PIV window.

6.3 Pebble Bed Reconstruction Using MATLAB Algorithms and VGSTUDIO with the Average Bed and Radial Porosity Analysis

The accurate prediction of the average bed porosity for pebble bed experiments improves the precision of pressure drop or friction factor obtained by the porous media models. Both the MATLAB and VGSTUDIO 3D pebble bed reconstructions using the TR-PIV images provide the average bed porosities close to the reference with the $\leq$1.22% relative difference. Most of the Euclidean distances between the MATLAB and VGSTUDIO paired pebble center coordinates are less than $d_p/2$. Decreasing the pebble diameter size by 1% overall results in the 4% relative difference in the average bed porosity compared to the experimental porosity. This is for removing the potential meshing issues with the singularity points in finite element analysis.

The MATLAB and VGSTUDIO oscillatory porosity profiles generated by taking the local porosity at every $0.12d_p$ cylindrical layer are within the 2.3% average relative difference. The sensitivity study of radial porosity values verifies the 1.1% average relative difference for the $15d_p$ bed height relative to the values

obtained with the original reconstructed geometries. The radial porosity determined by taking a quarter, a half, or three quarters of the d_p bed volume is more randomized and oscillating. Therefore, at least the full volume of the d_p bed volume is necessary to bring the close radial porosity oscillation locations. Additionally, the new oscillatory porosity function derived based on the Martin porosity correlation or the Hunt and Tien exponential function can be utilized for approximating the radial porosity of pebble bed experiments.

6.4 Scaling Analysis

The integral similarity relations specific for PBRs are derived for designing the heated engineering-scale pebble bed experiments. They are written in Python for easily changing the geometric and pressure scaling ratios or material properties, which would be determined based on the feasibility of new experimental setups. This code computes the consequent scaling ratios of power density, reactor power, velocity, temperature rise, mass flow rate, pressure drop, solid-fluid convective heat transfer coefficient, and effective thermal conductivities.

6.5 Recommendations for Further Research

- Further studies on correlations for the solid-fluid convective heat transfer coefficient and effective thermal conductivities are recommended to capture the near-wall phenomena more suitably.
- Improvement of the MATLAB algorithms may be necessary to accurately predict pebble locations with a similar accuracy level obtained by VGSTUDIO.
- VGSTUDIO can be utilized for reconstructing the future pebble bed experiments.
- The STAR-CCM+ discrete element method can be used for packing pebbles in a random manner to properly estimate the average bed and radial porosities.
- While this initial attempt contributes to our understanding, further studies related to volume-averaging the variable porosity in a different number of sectors are recommended in order to improve nuclear reactor pressure drop and velocity profile calculations.
- The heated pebble bed experiments must be built by considering the current scaling study for bringing a similar fluid motion and heat transfer of modular PBRs.

REFERENCES

[1] I. Pioro and R. Duffey, "Current and Future Nuclear Power Reactors and Plants," in *Managing Global Warming*, pp. 117–197, Academic Press, Cambridge, MA, 2019.

[2] I. Hore-Lacy, "The "Front End" of the Nuclear Fuel Cycle," in *Nuclear Energy in the 21st Century*, pp. 55–74, Academic Press, Cambridge, MA, 2006.

[3] M. Richards and C. Hamilton, "HTGR Economic/Business Analysis and Trade Studies Market Analysis for HTGR Technologies and Applications," Tech. Rep. USNC-NIA-G00001/Rev.0, U.S. DOE Office of Nuclear Energy, Science, and Technology, Idaho Falls, ID, 2013.

[4] J. Beck and L. Pincock, "High Temperature Gas-Cooled Reactors Lessons Learned Applicable to the Next Generation Nuclear Plant," Tech. Rep. INL/EXT-10-19329, Idaho National Laboratory, Idaho Falls, ID, 2011.

[5] T. Wilson Jr., S. Ball, R. Wood, M. Cetiner, and W. Poore, "Advanced Control and Protection System Design Methods for Modular HTGRs," Tech. Rep. ORNL/TM-2012/170, Oak Ridge National Laboratory, Oak Ridge, TN, 2012.

[6] H. Reutler and G. Lohnert, "Advantages of Going Modular in HTRs," *Nuclear Engineering and Design*, vol. 78, no. 2, pp. 129–136, 1984.

[7] Y. Hassan and C. Kang, "Pressure Drop in a Pebble Bed Reactor under High Reynolds Number," *Nuclear Technology*, vol. 180, no. 2, pp. 159–173, 2012.

[8] E. Erdim, Ö. Akgiray, and İ. Demir, "A Revisit of Pressure Drop-Flow Rate Correlations for Packed Beds of Spheres," *Powder Technology*, vol. 283, pp. 488–504, 2015.

[9] Z. Guo, Z. Sun, N. Zhang, and M. Ding, "Influence of Confining Wall on Pressure Drop and Particle-to-Fluid Heat Transfer in Packed Beds with Small D/d Ratios under High Reynolds Number," *Chemical Engineering Science*, vol. 209, p. 115200, 2019.

[10] A. Novak, S. Schunert, R. Carlsen, P. Balestra, D. Andrs, J. Lee, J. Kelly, R. Slaybaugh, R. Martineau, and H. Gougar, "Pronghorn Theory Manual," Tech. Rep. INL/EXT-18-44453-Rev001, Idaho National Laboratory, Idaho Falls, ID, 2020.

[11] J. Lee, P. Balestra, S. Schunert, A. Novak, Y. Hassan, and M. DeHart, "Pronghorn Fully Compressible Equation Set Validation against SANA Open Plenum Experiments," in *Proceedings of the High Temperature Reactor Technology (HTR2021)*, Virtual Conference, June 2–5, Indonesian Nuclear Society, 2021.

[12] J. Lee, S. King, Y. A. Hassan, and T. Nguyen, "Pronghorn Porous Media Model Validation with Pressure Drop Measurements," in *19th International Topical Meeting on Nuclear Reactor Thermal Hydraulics (NURETH19)*, Virtual Conference, March 6–11, American Nuclear Society, 2022.

[13] J. Lee, R. Muyshondt, P. Balestra, R. Skifton, Y. Hassan, D. Nguyen, and B. Maher, "Pebble Bed Reconstruction Using MATLAB Algorithms and VGSTUDIO with the Average Bed and Radial Porosity Analysis," *Nuclear Engineering and Design* [Submitted].

[14] M. Quintard, "Introduction to Heat and Mass Transport in Porous Media," Tech. Rep. STO-EN-AVT-261, von Karman Institute for Fluid Dynamics, Rhode Saint Genese, Belgium, 2015.

[15] J. Bear, *Dynamics of Fluids in Porous Media*. Dover Publications, Inc., Mineola, NY, 1988.

[16] M. Yio, H. Wong, and N. Buenfeld, "Representative Elementary Volume (REV) of Cementitious Materials from Three-Dimensional Pore Structure Analysis," *Cement and Concrete Research*, vol. 102, pp. 187–202, 2017.

[17] D. Takhanov, "Forchheimer Model for Non-Darcy Flow in Porous Media and Fractures," Master's Thesis, Imperial College London, London, England, 2011.

[18] R. Zimmerman, A. Al-Yaarubi, C. Pain, and C. Grattoni, "Non-Linear Regimes of Fluid Flow in Rock Fractures," *International Journal of Rock Mechanics and Mining Sciences*, vol. 41, no. 3, pp. 163–169, 2004.

[19] Pronghorn Development and Analysis Group, "Pronghorn: A Coarse Mesh Thermal-Hydraulics Application Based on MOOSE for Advanced Reactor Concepts," in *NUC Workshop-Innovations in Advanced Reactor Design, Analysis, and Licensing*, Raleigh, NC, September 18, North Carolina State University, 2019.

[20] A. Novak, S. Schunert, R. Carlsen, P. Balestra, R. Slaybaugh, and R. Martineau, "Multiscale Thermal-Hydraulic Modeling of the Pebble Bed Fluoride-Salt-Cooled High-Temperature Reactor," *Annals of*

Nuclear Energy, vol. 154, p. 107968, 2021.

[21] A. Novak, J. Peterson, L. Zou, D. Andrš, R. Slaybaugh, and R. Martineau, "Validation of Pronghorn Friction-Dominated Porous Media Thermal-Hydraulics Model with the SANA Experiments," *Nuclear Engineering and Design*, vol. 350, pp. 182–194, 2019.

[22] E. Lemmon and R. Jacobsen, "Viscosity and Thermal Conductivity Equations for Nitrogen, Oxygen, Argon, and Air," *International Journal of Thermophysics*, vol. 25, no. 1, pp. 21–69, 2004.

[23] R. Span, E. Lemmon, R. Jacobsen, W. Wagner, and A. Yokozeki, "A Reference Equation of State for the Thermodynamic Properties of Nitrogen for Temperatures from 63.151 to 1000 K and Pressures to 2200 MPa," *Journal of Physical and Chemical Reference Data*, vol. 29, no. 6, pp. 1361–1433, 2000.

[24] L. Zou, A. Novak, R. Martineau, and H. Gougar, "Validation of Pronghorn with the SANA Experiments," Tech. Rep. INL/EXT-17-44085, Idaho National Laboratory, Idaho Falls, ID, 2017.

[25] A. Butland and R. Maddison, "The Specific Heat of Graphite: An Evaluation of Measurements," *Journal of Nuclear Materials*, vol. 49, no. 1, pp. 45–56, 1973.

[26] B. Stöcker and H. Niessen, "Data Sets of the SANA Experiment 1994-1996," Tech. Rep. Jül-3409, Institut für Sicherheitsforschung und Reaktortechnik, Jülich, Germany, 1997.

[27] E. Lemmon, R. Jacobsen, S. Penoncello, and D. Friend, "Thermodynamic Properties of Air and Mixtures of Nitrogen, Argon, and Oxygen from 60 to 2000 K at Pressures to 2000 MPa," *Journal of Physical and Chemical Reference Data*, vol. 29, no. 3, pp. 331–385, 2000.

[28] R. Montgomery, "Viscosity and Thermal Conductivity of Air and Diffusivity of Water Vapor in Air," *Journal of the Atmospheric Sciences*, vol. 4, no. 6, pp. 193–196, 1947.

[29] "Release on the IAPWS Formulation 2008 for the Viscosity of Ordinary Water Substance," Tech. Rep. IAPWS R12-08, International Association for the Properties of Water and Steam, Berlin, Germany, 2008.

[30] N. Amini and Y. A. Hassan, "An Investigation of Matched Index of Refraction Technique and Its Application in Optical Measurements of Fluid Flow," *Experiments in Fluids*, vol. 53, no. 6, pp. 2011–2020, 2012.

[31] H. Petersen, "The Properties of Helium: Density, Specific Heats, Viscosity, and Thermal Conductivity at Pressures from 1 to 100 bar and from Room Temperature to about 1800 K," Tech. Rep. Risø Report No. 224, Risø National Laboratory, Roskilde, Denmark, 1970.

[32] P. Chai, Y. Wu, and K. Okamoto, "Experimental Determination of the Emissivity of Nuclear Graphite at High Temperature Conditions," *Mechanical Engineering Letters*, vol. 6, pp. 20–00204, 2020.

[33] B. Guo, H. Wang, H. Xie, and P. Chen, "Elastic Constants Characterization on Graphite at 500°C by the Virtual Fields Method," *Theoretical and Applied Mechanics Letters*, vol. 4, no. 2, p. 021010, 2014.

[34] L. Young and J. Brandrup, *Polymer Handbook*. John Wiley and Sons, Inc., Hoboken, NJ, 1975.

[35] B. Bhushan and Z. Burton, "Adhesion and Friction Properties of Polymers in Microfluidic Devices," *Nanotechnology*, vol. 16, no. 4, p. 467, 2005.

[36] S. Fereres, C. Lautenberger, A. Fernandez-Pello, D. Urban, and G. Ruff, "Understanding Ambient Pressure Effects on Piloted Ignition through Numerical Modeling," *Combustion and Flame*, vol. 159, no. 12, pp. 3544–3553, 2012.

[37] G. Mueller, "Radial Void Fraction Distributions in Randomly Packed Fixed Beds of Uniformly Sized Spheres in Cylindrical Containers," *Powder Technology*, vol. 72, no. 3, pp. 269–275, 1992.

[38] Y. Sato, T. Hirose, F. Takahashi, and M. Toda, "Pressure Loss and Liquid Holdup in Packed Bed Reactor with Cocurrent Gas-Liquid Down Flow," *Journal of Chemical Engineering of Japan*, vol. 6, no. 2, pp. 147–152, 1973.

[39] D. Haughey and G. Beveridge, "Structural Properties of Packed Beds-A Review," *Canadian Journal of Chemical Engineering*, vol. 47, no. 2, pp. 130–140, 1969.

[40] A. Dixon, "Correlations for Wall and Particle Shape Effects on Fixed Bed Bulk Voidage," *Canadian Journal of Chemical Engineering*, vol. 66, no. 5, pp. 705–708, 1988.

[41] A. de Klerk, "Voidage Variation in Packed Beds at Small Column to Particle Diameter Ratio," *AIChE Journal*, vol. 49, no. 8, pp. 2022–2029, 2003.

[42] G. Beavers, E. Sparrow, and D. Rodenz, "Influence of Bed Size on the Flow Characteristics and Porosity of Randomly Packed Beds of Spheres," *Journal of Applied Mechanics*, vol. 40, no. 3, pp. 655–660, 1973.

[43] E. Foumeny, F. Benyahia, J. Castro, H. Moallemi, and S. Roshani, "Correlations of Pressure Drop in Packed Beds Taking into Account the Effect of Confining Wall," *International Journal of Heat and Mass Transfer*, vol. 36, no. 2, pp. 536–540, 1993.

[44] R. Fand and R. Thinakaran, "The Influence of the Wall on Flow through Pipes Packed with Spheres," *Journal of Fluids Engineering*, vol. 112, no. 1, pp. 84–88, 1990.

[45] R. Zou and A. Yu, "The Packing of Spheres in a Cylindrical Container: The Thickness Effect," *Chemical Engineering Science*, vol. 50, no. 9, pp. 1504–1507, 1995.

[46] R. Jeschar, "Druckverlust in Mehrkornschüttungen aus Kugeln," *Archiv für das Eisenhüttenwesen*, vol. 35, no. 2, pp. 91–108, 1964.

[47] F. Benyahia and K. O'Neill, "Enhanced Voidage Correlations for Packed Beds of Various Particle Shapes and Sizes," *Particulate Science and Technology*, vol. 23, no. 2, pp. 169–177, 2005.

[48] N. Cheng, "Wall Effect on Pressure Drop in Packed Beds," *Powder Technology*, vol. 210, no. 3, pp. 261–266, 2011.

[49] R. Fand, M. Sundaram, and M. Varahasamy, "Incompressible Fluid Flow through Pipes Packed with Spheres at Low Dimension Ratios," *Journal of Fluids Engineering*, vol. 115, no. 1, pp. 169–172, 1993.

[50] R. Raichura, "Pressure Drop and Heat Transfer in Packed Beds with Small Tube-to-Particle Diameter Ratio," *Experimental Heat Transfer*, vol. 12, no. 4, pp. 309–327, 1999.

[51] A. Montillet, E. Akkari, and J. Comiti, "About a Correlating Equation for Predicting Pressure Drops through Packed Beds of Spheres in a Large Range of Reynolds Numbers," *Chemical Engineering and Processing: Process Intensification*, vol. 46, no. 4, pp. 329–333, 2007.

[52] W. Reichelt, "Zur Berechnung des Druckverlustes einphasig durchströmter Kugel-und Zylinderschüttungen," *Chemie Ingenieur Technik*, vol. 44, no. 18, pp. 1068–1071, 1972.

[53] H. Calis, J. Nijenhuis, B. Paikert, F. Dautzenberg, and C. van den Bleek, "CFD Modelling and Experimental Validation of Pressure Drop and Flow Profile in a Novel Structured Catalytic Reactor Packing," *Chemical Engineering Science*, vol. 56, no. 4, pp. 1713–1720, 2001.

[54] N. Cheng, Z. Hao, and S. K. Tan, "Comparison of Quadratic and Power Law for Nonlinear Flow through Porous Media," *Experimental Thermal and Fluid Science*, vol. 32, no. 8, pp. 1538–1547, 2008.

[55] Y. Cohen and A. Metzner, "Wall Effects in Laminar Flow of Fluids through Packed Beds," *AIChE Journal*, vol. 27, no. 5, pp. 705–715, 1981.

[56] H. Martin, "Low Peclet Number Particle-to-Fluid Heat and Mass Transfer in Packed Beds," *Chemical Engineering Science*, vol. 33, no. 7, pp. 913–919, 1978.

[57] O. Bey and G. Eigenberger, "Fluid Flow through Catalyst Filled Tubes," *Chemical Engineering Science*, vol. 52, no. 8, pp. 1365–1376, 1997.

[58] C. du Toit, "Radial Variation in Porosity in Annular Packed Beds," *Nuclear Engineering and Design*, vol. 238, no. 11, pp. 3073–3079, 2008.

[59] D. Vortmeyer and J. Schuster, "Evaluation of Steady Flow Profiles in Rectangular and Circular Packed Beds by a Variational Method," *Chemical Engineering Science*, vol. 38, no. 10, pp. 1691–1699, 1983.

[60] R. Benenati and C. Brosilow, "Void Fraction Distribution in Beds of Spheres," *AIChE Journal*, vol. 8, no. 3, pp. 359–361, 1962.

[61] P. Cheng and C. Hsu, "Fully-Developed, Forced Convective Flow through an Annular Packed-Sphere Bed with Wall Effects," *International Journal of Heat and Mass Transfer*, vol. 29, no. 12, pp. 1843–1853, 1986.

[62] S. Yagi and D. Kunii, "Studies on Heat Transfer near Wall Surface in Packed Beds," *AIChE Journal*, vol. 6, no. 1, pp. 97–104, 1960.

[63] M. Hunt and C. Tien, "Non-Darcian Flow, Heat and Mass Transfer in Catalytic Packed-Bed Reactors," *Chemical Engineering Science*, vol. 45, no. 1, pp. 55–63, 1990.

[64] J. Valstar, P. van den Berg, and J. Oyserman, "Comparison between Two-Dimensional Fixed Bed Reactor Calculations and Measurements," *Chemical Engineering Science*, vol. 30, no. 7, pp. 723–728, 1975.

[65] S. White and C. Tien, "Analysis of Flow Channeling near the Wall in Packed Beds," *Wärme-und Stoffübertragung*, vol. 21, no. 5, pp. 291–296, 1987.

[66] L. Roblee, R. Baird, and J. Tierney, "Radial Porosity Variations in Packed Beds," *AIChE Journal*, vol. 4, no. 4, pp. 460–464, 1958.

[67] K. Ridgway and K. Tarbuck, "Radial Voidage Variation in Randomly-Packed Beds of Spheres of Different Sizes," *Journal of Pharmacy and Pharmacology*, vol. 18, no. S1, pp. 168S–175S, 1966.

[68] J. Goodling, R. Vachon, W. Stelpflug, S. Ying, and M. Khader, "Radial Porosity Distribution in Cylindrical Beds Packed with Spheres," *Powder Technology*, vol. 35, no. 1, pp. 23–29, 1983.

[69] S. Liu, A. Afacan, and J. Masliyah, "Steady Incompressible Laminar Flow in Porous Media," *Chemical Engineering Science*, vol. 49, no. 21, pp. 3565–3586, 1994.

[70] D. Jones and H. Krier, "Gas Flow Resistance Measurements through Packed Beds at High Reynolds Numbers," *Journal of Fluids Engineering*, vol. 105, no. 2, pp. 168–172, 1983.

[71] P. C. Carman, "Fluid Flow through Granular Beds," *Chemical Engineering Research and Design*, vol. 75, pp. S32–S48, 1997.

[72] J. Tallmadge, "Packed Bed Pressure Drop-An Extension to Higher Reynolds Numbers," *AIChE Journal*, vol. 16, no. 6, pp. 1092–1093, 1970.

[73] R. Hicks, "Pressure Drop in Packed Beds of Spheres," *Industrial & Engineering Chemistry Fundamentals*, vol. 9, no. 3, pp. 500–502, 1970.

[74] S. Ergun, "Fluid Flow through Packed Columns," *Chemical Engineering Progress*, vol. 48, pp. 89–94, 1952.

[75] A. Preller, *Numerical Modelling of Flow through Packed Beds of Uniform Spheres*. PhD Dissertation, North-West University, Potchefstroom, South Africa, 2011.

[76] A. van der Walt, *Pressure Drop through a Packed Bed*. PhD Dissertation, North-West University, Potchefstroom, South Africa, 2006.

[77] C. Zoltani, "Flow Resistance in Packed and Fluidized Beds: An Assessment of Current Practice," Tech. Rep. BRL-TR-3366, U.S. Army Ballistic Research Laboratory, Aberdeen Proving Ground, MD, 1992.

[78] P. Avontuur and D. Geldart, "A Quality Assessment of the Ergun Equation," *Chemical Engineering Journal*, pp. 994–996, 1996.

[79] D. Handley, "Momentum and Heat Transfer Mechanism in Regular Shaped Packing," *Transactions of the Institution of Chemical Engineers*, vol. 46, pp. T251–T264, 1968.

[80] E. Ozahi, M. Y. Gundogdu, and M. Carpinlioglu, "A Modification on Ergun's Correlation for Use in Cylindrical Packed Beds with Non-Spherical Particles," *Advanced Powder Technology*, vol. 19, no. 4, pp. 369–381, 2008.

[81] P. Foscolo, L. Gibilaro, and S. Waldram, "A Unified Model for Particulate Expansion of Fluidised Beds and Flow in Fixed Porous Media," *Chemical Engineering Science*, vol. 38, no. 8, pp. 1251–1260, 1983.

[82] J. Yu, M. Zhang, W. Fan, Y. Zhou, and G. Zhao, "Study on Performance of the Ball Packed-Bed Regenerator: Experiments and Simulation," *Applied Thermal Engineering*, vol. 22, no. 6, pp. 641–651, 2002.

[83] I. Macdonald, M. El-Sayed, K. Mow, and F. Dullien, "Flow through Porous Media-The Ergun Equation Revisited," *Industrial & Engineering Chemistry Fundamentals*, vol. 18, no. 3, pp. 199–208, 1979.

[84] H. Rumpf and A. Gupte, "Einflüsse der Porosität und Korngrößenverteilung im Widerstandsgesetz der Porenströmung," *Chemie Ingenieur Technik*, vol. 43, no. 6, pp. 367–375, 1971.

[85] C. Kyan, D. Wasan, and R. Kintner, "Flow of Single-Phase Fluids through Fibrous Beds," *Industrial & Engineering Chemistry Fundamentals*, vol. 9, no. 4, pp. 596–603, 1970.

[86] C. Dudgeon, "An Experimental Study of the Flow of Water through Coarse Granular Media," *La Houille Blanche*, no. 7, pp. 785–801, 1966.

[87] G. Fancher and J. Lewis, "Flow of Simple Fluids through Porous Materials," *Industrial & Engineering Chemistry*, vol. 25, no. 10, pp. 1139–1147, 1933.

[88] R. Hayes, A. Afacan, and B. Boulanger, "An Equation of Motion for an Incompressible Newtonian Fluid in a Packed Bed," *Transport in Porous Media*, vol. 18, no. 2, pp. 185–198, 1995.

[89] J. Wu, B. Yu, and M. Yun, "A Resistance Model for Flow through Porous Media," *Transport in Porous Media*, vol. 71, no. 3, pp. 331–343, 2008.

[90] Y. Bo-Ming and L. Jian-Hua, "A Geometry Model for Tortuosity of Flow Path in Porous Media," *Chinese Physics Letters*, vol. 21, no. 8, p. 1569, 2004.

[91] Z. Wang, Y. Ding, and M. Ghadiri, "Flow of a Gas-Solid Two-Phase Mixture through a Packed Bed," *Chemical Engineering Science*, vol. 59, no. 15, pp. 3071–3079, 2004.

[92] B. Eisfeld and K. Schnitzlein, "The Influence of Confining Walls on the Pressure Drop in Packed Beds," *Chemical Engineering Science*, vol. 56, no. 14, pp. 4321–4329, 2001.

[93] D. Mehta and M. C. Hawley, "Wall Effect in Packed Columns," *Industrial & Engineering Chemistry Process Design and Development*, vol. 8, no. 2, pp. 280–282, 1969.

[94] L. Harrison, K. Brunner, and W. Hecker, "A Combined Packed-Bed Friction Factor Equation: Extension to Higher Reynolds Number with Wall Effects," *AIChE Journal*, vol. 3, no. 59, pp. 703–706, 2013.

[95] R. Fand, B. Kim, A. Lam, and R. Phan, "Resistance to the Flow of Fluids through Simple and Complex Porous Media Whose Matrices Are Composed of Randomly Packed Spheres," *Journal of Fluids Engineering*, vol. 109, no. 3, pp. 268–273, 1987.

[96] Geschäftsstelle des Kerntechnischen Ausschusses, "Reactor Core Design of High-Temperature Gas-Cooled Reactors. Part 3: Loss of Pressure through Friction in Pebble Bed Cores," Tech. Rep. KTA 3102.3, Nuclear Safety Standards Commission, Berlin, Germany, 1981.

[97] M. Çarpinlioğlu and E. Özahi, "A Simplified Correlation for Fixed Bed Pressure Drop," *Powder Technology*, vol. 187, no. 1, pp. 94–101, 2008.

[98] C. Wentz Jr and G. Thodos, "Pressure Drops in the Flow of Gases through Packed and Distended Beds of Spherical Particles," *AIChE Journal*, vol. 9, no. 1, pp. 81–84, 1963.

[99] S. Wilcox and H. Krier, "Gas Flow Resistance Measurements through Packed Beds at High Reynolds Numbers," Tech. Rep. AAE 80-1, Illinois University at Urbana Dept of Aeronautical and Astronautical Engineering, Urbana, IL, 1980.

[100] R. Abdulmohsin and M. Al-Dahhan, "Pressure Drop and Fluid Flow Characteristics in a Packed Pebble Bed Reactor," *Nuclear Technology*, vol. 198, no. 1, pp. 17–25, 2017.

[101] M. A. Yildiz, G. Botha, H. Yuan, E. Merzari, R. C. Kurwitz, and Y. A. Hassan, "Direct Numerical Simulation of the Flow through a Randomly Packed Pebble Bed," *Journal of Fluids Engineering*, vol. 142, no. 4, p. 041405, 2020.

[102] J. Lee and K. Ogawa, "Pressure Drop through Packed Bed," *Journal of Chemical Engineering of Japan*, vol. 27, no. 5, pp. 691–693, 1994.

[103] S. Burke and W. Plummer, "Gas Flow through Packed Columns," *Industrial & Engineering Chemistry*, vol. 20, no. 11, pp. 1196–1200, 1928.

[104] M. Leva, M. Weintraub, M. Grummer, and M. Pollchik, "Fluidization of an Anthracite Coal," *Industrial & Engineering Chemistry*, vol. 41, no. 6, pp. 1206–1212, 1949.

[105] A. Montillet, "Flow through a Finite Packed Bed of Spheres: A Note on the Limit of Applicability of the Forchheimer-Type Equation," *Journal of Fluids Engineering*, vol. 126, no. 1, pp. 139–143, 2004.

[106] H. Rose, "On the Resistance Coefficient-Reynolds Number Relationship for Fluid Flow through a Bed of Granular Material," *Proceedings of the Institution of Mechanical Engineers*, vol. 153, no. 1, pp. 154–168, 1945.

[107] H. Rose and A. Rizk, "Further Researches in Fluid Flow through Beds of Granular Material," *Proceedings of the Institution of Mechanical Engineers*, vol. 160, no. 1, pp. 493–511, 1949.

[108] K. Andersson, *Pressure Drop in Packed Beds*. Elanders, Mölnlycke, Sweden, 1963.

[109] S. Ergun and A. Orning, "Fluid Flow through Randomly Packed Columns and Fluidized Beds," *Industrial & Engineering Chemistry*, vol. 41, no. 6, pp. 1179–1184, 1949.

[110] M. Leva, *Fluid Flow through Packed and Fluidized Systems*. U.S. Government Printing Office, Washington, DC, 1951.

[111] W. Schriever, "Law of Flow for the Passage of a Gas-Free Liquid through a Spherical-Grain Sand," *Transactions of the AIME*, vol. 86, no. 1, pp. 329–336, 1930.

[112] H. Green and G. Ampt, "Studies on Soil Physics: Part II-The Permeability of an Ideal Soil to Air and Water," *Journal of Agricultural Science*, vol. 5, no. 1, pp. 1–26, 1912.

[113] M. Muskat and H. Botset, "Flow of Gas through Porous Materials," *Journal of Applied Physics*, vol. 1, no. 1, pp. 27–47, 1931.

[114] J. Chalmers, D. Taliaferro Jr, and E. Rawlins, "Flow of Air and Gas through Porous Media," *Transactions of the AIME*, vol. 98, no. 1, pp. 375–400, 1932.

[115] C. Furnas, *Flow of Gases through Beds of Broken Solids*. U.S. Government Printing Office, Washington, DC, 1929.

[116] B. Bakhmeteff and N. Feodoroff, "Flow through Granular Media," *Journal of Applied Mechanics*, vol. 4, no. 3, pp. A97–A104, 1937.

[117] F. Mavis and E. Wilsey, "A Study of the Permeability of Sand," Tech. Rep. Bulletin 7, State University of Iowa, Iowa City, IA, 1936.

[118] R. Traxler and L. Baum, "Permeability of Compacted Powders Determination of Average Pore Size," *Journal of Applied Physics*, vol. 7, no. 1, pp. 9–14, 1936.

[119] T. Chilton and A. Colburn, "Pressure Drop in Packed Tubes," *Industrial & Engineering Chemistry*, vol. 23, no. 8, pp. 913–919, 1931.

[120] L. J. Petrovic and G. Thodos, "Mass Transfer in Flow of Gases through Packed Beds. Low Reynolds Number Region," *Industrial & Engineering Chemistry Fundamentals*, vol. 7, no. 2, pp. 274–280, 1968.

[121] Geschäftsstelle des Kerntechnischen Ausschusses, "Reactor Core Design of High-Temperature Gas-Cooled Reactors. Part 2: Heat Transfer in Spherical Fuel Elements," Tech. Rep. KTA 3102.2, Nuclear Safety Standards Commission, Berlin, Germany, 1983.

[122] D. Gunn, "Transfer of Heat or Mass to Particles in Fixed and Fluidised Beds," *International Journal of Heat and Mass Transfer*, vol. 21, no. 4, pp. 467–476, 1978.

[123] A. Amiri, K. Vafai, and T. Kuzay, "Effects of Boundary Conditions on Non-Darcian Heat Transfer through Porous Media and Experimental Comparisons," *Numerical Heat Transfer, Part A: Applications*, vol. 27, no. 6, pp. 651–664, 1995.

[124] Y. Li and W. Ji, "Thermal Analysis of Pebble-Bed Reactors Based on a Tightly Coupled Mechanical-Thermal Model," in *16th International Topical Meeting on Nuclear Reactor Thermal Hydraulics (NURETH16)*, Chicago, IL, August 30–September 4, American Nuclear Society, 2015.

[125] H. Suikkanen, V. Rintala, and R. Kyrki-Rajamäki, "Development of a Coupled Multi-Physics Code System for Pebble Bed Reactor Core Modeling," in *Proceedings of the High Temperature Reactor Technology (HTR2014)*, Weihai, China, October 27–31, Institute of Nuclear and New Energy Technology, 2014.

[126] H. Niessen and S. Ball, "Heat Transport and Afterheat Removal for Gas Cooled Reactors under Accident Conditions," Tech. Rep. IAEA-TECDOC-1163, IAEA, Vienna, Austria, 2000.

[127] C. Visser, *Modelling Heat and Mass Flow through Packed Pebble Beds: A Heterogeneous Volume-Averaged Approach*. PhD Dissertation, University of Pretoria, Pretoria, South Africa, 2008.

[128] G. Auwerda, Y. Zheng, D. Lathouwers, and J. Kloosterman, "Effect of Non-Uniform Porosity Distribution on Thermal Hydraulics in a Pebble Bed Reactor," in *14th International Topical Meeting on Nuclear Reactor Thermal Hydraulics (NURETH14)*, Toronto, Canada, September 25–30, Canadian Nuclear Society, 2011.

[129] V. Prasad, N. Kladias, A. Bandyopadhaya, and Q. Tian, "Evaluation of Correlations for Stagnant Thermal Conductivity of Liquid-Saturated Porous Beds of Spheres," *International Journal of Heat and Mass Transfer*, vol. 32, no. 9, pp. 1793–1796, 1989.

[130] M. Kandula, "On the Effective Thermal Conductivity of Porous Packed Beds with Uniform Spherical Particles," *Journal of Porous Media*, vol. 14, no. 10, pp. 919–926, 2011.

[131] E. You, X. Sun, F. Chen, L. Shi, and Z. Zhang, "An Improved Prediction Model for the Effective Thermal Conductivity of Compact Pebble Bed Reactors," *Nuclear Engineering and Design*, vol. 323, pp. 95–102, 2017.

[132] Siemens PLM Software, Inc., "STAR-CCM+ User Guide 2021.1," 2021.

[133] A. Nakayama and F. Kuwahara, "A Macroscopic Turbulence Model for Flow in a Porous Medium," *Journal of Fluids Engineering*, vol. 121, no. 2, pp. 427–433, 1999.

[134] T. H. Shih, W. W. Liou, A. Shabbir, Z. Yang, and J. Zhu, "A New $k - \varepsilon$ Eddy Viscosity Model for High Reynolds Number Turbulent Flows: Model Development and Validation," Tech. Rep. NASA-TM-106721, NASA Lewis Research Center, Cleveland, OH, 1995.

[135] M. Surendran, "Computational Fluid Dynamic Modeling of Natural Convection in Vertically Heated Rods," Master's Thesis, Utah State University, Logan, UT, 2016.

[136] D. Zhang, "Comparison of Various Turbulence Models for Unsteady Flow around a Finite Circular Cylinder at Re=20000," *Journal of Physics: Conference Series*, vol. 910, no. 1, p. 012027, 2017.

[137] A. Hadid, N. Mansour, and O. Zeman, "Single Point Modeling of Rotating Turbulent Flows," Tech. Rep. N95-21060, Center for Turbulence Research, Stanford University, Standford, CA, 1994.

[138] M. Wolfshtein, "The Velocity and Temperature Distribution in One-Dimensional Flow with Turbulence Augmentation and Pressure Gradient," *International Journal of Heat and Mass Transfer*, vol. 12, no. 3, pp. 301–318, 1969.

[139] H. Reichardt, "Vollständige Darstellung der Turbulenten Geschwindigkeitsverteilung in Glatten Leitungen," *Journal of Applied Mathematics and Mechanics*, vol. 31, no. 7, pp. 208–219, 1951.

[140] D. C. Wilcox, *Turbulence Modeling for CFD*, vol. 2. DCW Industries, Inc., La Canada, CA, 1998.

[141] F. R. Menter, "Two-Equation Eddy-Viscosity Turbulence Models for Engineering Applications," *AIAA Journal*, vol. 32, no. 8, pp. 1598–1605, 1994.

[142] C. Freitas, "The Issue of Numerical Uncertainty," *Applied Mathematical Modelling*, vol. 26, no. 2, pp. 237–248, 2002.

[143] R. Johnson, "Modeling Strategies for Unsteady Turbulent Flows in the Lower Plenum of the VHTR," *Nuclear Engineering and Design*, vol. 238, no. 3, pp. 482–491, 2008.

[144] W. Oberkampf and C. Roy, *Verification and Validation in Scientific Computing*. Cambridge University Press, Cambridge, England, 2010.

[145] A. Rakhimov, D. Visser, and E. Komen, "Uncertainty Quantification Method for CFD Applied to the Turbulent Mixing of Two Water Layers-II: Deterministic Sampling for Input Uncertainty," *Nuclear Engineering and Design*, vol. 348, pp. 146–158, 2019.

[146] L. Kwaśniewski, "Application of Grid Convergence Index in FE Computation," *Bulletin of the Polish Academy of Sciences: Technical Sciences*, vol. 61, no. 1, pp. 123–128, 2013.

[147] L. Schwer, "Is Your Mesh Refined Enough? Estimating Discretization Error Using GCI," *7th LS-DYNA Anwenderforum*, vol. 1, no. 1, pp. 45–54, 2008.

[148] I. Celik, U. Ghia, P. Roache, and C. Freitas, "Procedure for Estimation and Reporting of Uncertainty Due to Discretization in CFD Applications," *Journal of Fluids Engineering*, vol. 130, no. 7, p. 078001, 2008.

[149] I. Celik and O. Karatekin, "Numerical Experiments on Application of Richardson Extrapolation with Nonuniform Grids," *Journal of Fluids Engineering*, vol. 119, no. 3, pp. 584–590, 1997.

[150] B. R. Baliga and I. Y. Lokhmanets, "Generalized Richardson Extrapolation Procedures for Estimating Grid-Independent Numerical Solutions," *International Journal of Numerical Methods for Heat & Fluid Flow*, vol. 26, no. 3/4, pp. 1121–1144, 2016.

[151] A. Rakhimov, D. Visser, and E. Komen, "Uncertainty Quantification Method for CFD Applied to the Turbulent Mixing of Two Water Layers," *Nuclear Engineering and Design*, vol. 333, pp. 1–15, 2018.

[152] M. McHale, J. Friedman, and J. Karian, *Standard for Verification and Validation in Computational Fluid Dynamics and Heat Transfer*. American Society of Mechanical Engineers, New York, NY, 2009.

[153] D. Altman and J. Bland, "Standard Deviations and Standard Errors," *British Medical Journal*, vol. 331, no. 7521, p. 903, 2005.

[154] H. Coleman and F. Stern, "Uncertainties and CFD Code Validation," *Journal of Fluids Engineering*, vol. 119, no. 4, pp. 795–803, 1997.

[155] R. Abernethy, R. Benedict, and R. Dowdell, "ASME Measurement Uncertainty," *Journal of Fluids Engineering*, vol. 107, no. 2, pp. 161–164, 1985.

[156] K. Maupin, L. Swiler, and N. Porter, "Validation Metrics for Deterministic and Probabilistic Data," *Journal of Verification, Validation, and Uncertainty Quantification*, vol. 3, no. 3, p. 031002, 2018.

[157] T. Pujol, J. Puig-Bargués, G. Arbat, M. Duran-Ros, C. Solé-Torres, J. Pujol, and F. de Cartagena, "Effect of Wand-Type Underdrains on the Hydraulic Performance of Pressurised Sand Media Filters," *Biosystems Engineering*, vol. 192, pp. 176–187, 2020.

[158] M. Pilou, S. Tsangaris, P. Neofytou, C. Housiadas, and Y. Drossinos, "Inertial Particle Deposition in a 90^o Laminar Flow Bend: An Eulerian Fluid Particle Approach," *Aerosol Science and Technology*, vol. 45, no. 11, pp. 1376–1387, 2011.

[159] J. Lei, J. Zhang, and L. Zhang, "Numerical Simulation Study on Distribution of Bubble in Flow near Aerator Based on CFD-PBM Coupled Model in Tunnel," *Mathematical Problems in Engineering*, vol. 2021, p. 6635856, 2021.

[160] S. Hosseini, M. Rezaei, M. Bag-Mohammadi, M. Karami, M. Moradkhani, M. Panahi, and M. Olazar, "Estimation of the Minimum Spouting Velocity in Shallow Spouted Beds by Intelligent Approaches: Study of Fine and Coarse Particles," *Powder Technology*, vol. 354, pp. 456–465, 2019.

[161] L. Debnath and P. Mikusinski, *Introduction to Hilbert Spaces with Applications*. Academic Press, Cambridge, MA, 2005.

[162] J. Ghosh and R. Ramamoorthi, *Bayesian Nonparametrics*. Springer Science & Business Media, Berlin/Heidelberg, Germany, 2003.

[163] D. Darling, "The Kolmogorov-Smirnov, Cramer-von Mises Tests," *Annals of Mathematical Statistics*, vol. 28, no. 4, pp. 823–838, 1957.

[164] S. Ferson, W. Oberkampf, and L. Ginzburg, "Model Validation and Predictive Capability for the Thermal Challenge Problem," *Computer Methods in Applied Mechanics and Engineering*, vol. 197, no. 29–32, pp. 2408–2430, 2008.

[165] D. Lin, F. Liu, X. Chen, R. Yan, M. Mei, J. Zhang, and Y. Zou, "A 3D-Reconstruction Research on the Visual Liquid-Pebble Bed," *Nuclear Techniques*, vol. 40, no. 10, p. 8, 2017.

[166] R. Pieritz, J. Reimann, and C. Ferrero, "3D Tomography Analysis of the Inner Structure of Pebbles and Pebble Beds," *Advanced Engineering Materials*, vol. 13, no. 3, pp. 145–155, 2011.

[167] J. Dijksman, N. Brodu, and R. Behringer, "Refractive Index Matched Scanning and Detection of Soft Particles," *Review of Scientific Instruments*, vol. 88, no. 5, p. 051807, 2017.

[168] B. Hilliard, W. J. Reeder, R. S. Skifton, R. Budwig, W. Basham, and D. Tonina, "A Biologically Friendly, Low-Cost, and Scalable Method to Map Permeable Media Architecture and Interstitial Flow," *Geophysical Research Letters*, vol. 48, no. 3, p. e2020GL090462, 2021.

[169] D. Nield and A. Bejan, *Convection in Porous Media*, vol. 3. Springer Publishing Company, Inc., New York, NY, 2006.

[170] C. Hsu and P. Cheng, "Thermal Dispersion in a Porous Medium," *International Journal of Heat and Mass Transfer*, vol. 33, no. 8, pp. 1587–1597, 1990.

[171] B. Nelson, "Scaling Analysis for the Pebble Bed of the Very High Temperature Gas-Cooled Reactor Thermal Hydraulic Test Facility," Master's Thesis, Oregan State University, Corvallis, OR, 2009.

[172] S. Yang, E. Kappes, T. Nguyen, R. Vaghetto, and Y. Hassan, "Experimental Study on 1/28 Scaled NGNP HTGR Reactor Building Test Facility Response to Depressurization Event," *Annals of Nuclear Energy*, vol. 114, pp. 154–164, 2018.

[173] R. Vaghetto and Y. Hassan, "Experimental Investigation of a Scaled Water-Cooled Reactor Cavity Cooling System," *Nuclear Technology*, vol. 187, no. 3, pp. 282–293, 2014.

[174] C. Tzanos and M. Farmer, "Feasibility Study for Use of the Natural Convection Shutdown Heat Removal Test Facility (NSTF) for VHTR Water-Cooled RCCS Shutdown," Tech. Rep. ANL-GENIV-079, Argonne National Laboratory, Lemont, IL, 2007.

[175] J. Reyes Jr, J. Groome, B. Woods, B. Jackson, and T. Marshall, "Scaling Analysis for the High Temperature Gas Reactor Test Section (GRTS)," *Nuclear Engineering and Design*, vol. 240, no. 2, pp. 397–404, 2010.

[176] D. Lisowski, R. Scherrer, T. Haskin, M. Anderson, M. Corradini, and S. Albiston, "Experimental Studies of NGNP Reactor Cavity Cooling System with Water," in *Proceedings of ICAPP*, Nice, France, May 2–5, Societe Francaise d'Energie Nucleaire, 2011.

[177] D. Lisowski, T. Haskin, A. Tokuhiro, M. Anderson, and M. Corradini, "Study on the Behavior of an Asymmetrically Heated Reactor Cavity Cooling System with Water in Single Phase," *Nuclear Technology*, vol. 183, no. 1, pp. 75–87, 2013.

[178] Q. Lv, X. Wang, I. Kim, X. Sun, R. Christensen, T. Blue, G. Yoder, D. Wilson, and P. Sabharwall, "Scaling Analysis for the Direct Reactor Auxiliary Cooling System for FHRs," *Nuclear Engineering and Design*, vol. 285, pp. 197–206, 2015.

[179] S. King, E. Kappes, M. Marciniak, D. Nguyen, Y. Hassan, and V. Ugaz, "Pressure Drop Measurements in a Versatile Experimental Facility of Packed Spheres," in *Transactions of the American Nuclear Society*, Washington, DC, November 30–December 3, American Nuclear Society, 2017.

[180] R. Muyshondt, B. Maher, N. Anand, K. Ngo, T. Nguyen, and Y. Hassan, "Pressure Drop and Time-Resolved PIV Measurements of Near-Wall Flows in a Test Facility with Randomly Packed Spheres," in *19th International Topical Meeting on Nuclear Reactor Thermal Hydraulics (NURETH19)*, Virtual Conference, March 6–11, American Nuclear Society, 2022.

[181] G. Cumming, F. Fidler, and D. L. Vaux, "Error Bars in Experimental Biology," *Journal of Cell Biology*, vol. 177, no. 1, pp. 7–11, 2007.

[182] G. Cumming, "Inference by Eye: Reading the Overlap of Independent Confidence Intervals," *Statistics in Medicine*, vol. 28, no. 2, pp. 205–220, 2009.

[183] D. M. Lane, D. Scott, M. Hebl, R. Guerra, D. Osherson, and H. Zimmer, *Introduction to Statistics*. Rice University, University of Houston Clear Lake, and Tufts University, Houston, TX, 2017.

[184] T. Xing and F. Stern, "Factors of Safety for Richardson Extrapolation," *Journal of Fluids Engineering*, vol. 132, no. 6, p. 061403, 2010.

[185] D. Reger, E. Merzari, P. Balestra, S. Schunert, Y. Hassan, and H. Yuan, "Investigation of the Pressure Drop in Packed Beds between Large Eddy Simulation and Multiple Correlations," in *19th International Topical Meeting on Nuclear Reactor Thermal Hydraulics (NURETH19)*, Virtual Conference, March 6–11, American Nuclear Society, 2022.

[186] J. Reyes Jr and J. Groome, "Developing Core Flow Analysis Methods for the VHTR and GFR Designs," Tech. Rep., Oregon State University, Corvallis, OR.

[187] A. George, "Introduction to the Pebble Bed Modular Reactor (PBMR)," Tech. Rep. 009949-185, Exelon Generation, Kennett Square, PA, 2001.

[188] M. Methnani and B. Tyobeka, "Evaluation of High Temperature Gas Cooled Reactor Performance: Benchmark Analysis Related to the PBMR-400, PBMM, GT-MHR, HTR-10 and the ASTRA Critical Facility," Tech. Rep. IAEA-TECDOC-1694, IAEA, Vienna, Austria, 2013.

[189] A. Kadak, "MIT Pebble Bed Reactor Project," *Nuclear Engineering and Technology*, vol. 39, no. 2, pp. 95–102, 2007.

[190] A. Kadak, "A Future for Nuclear Energy: Pebble Bed Reactors," *International Journal of Critical Infrastructures*, vol. 1, no. 4, pp. 330–345, 2005.

[191] M. Berte, "Modularity in Design of the MIT Pebble Bed Reactor," Master's Thesis, Massachusetts Institute of Technology, Cambridge, MA, 2004.

[192] "High Temperature Gas Cooled Reactor - Pebble-Bed Module (HTR-PM)," Tech. Rep. Status Report 96, Tsinghua University, Beijing, China, 2011.

[193] M. Barrachin, V. Basini, U. Basak, Ü. Colak, R. Dubourg, *et al.*, "High Temperature Gas Cooled Reactor: Fuels and Materials," Tech. Rep. IAEA-TECDOC-1645, IAEA, Vienna, Austria, 2010.

[194] X. Li, X. Li, L. Shi, Z. Zhang, and S. He, "Safety Analysis for Hot Gas Duct Vessel in HTR-PM," *Nuclear Technology*, vol. 174, no. 1, pp. 29–40, 2011.

[195] Z. Zhang, Y. Dong, F. Li, Z. Zhang, H. Wang, X. Huang, H. Li, B. Liu, X. Wu, H. Wang, *et al.*, "The Shandong Shidao Bay 200 MWe High-Temperature Gas-Cooled Reactor Pebble-Bed Module (HTR-PM) Demonstration Power Plant: An Engineering and Technological Innovation," *Engineering*, vol. 2, no. 1, pp. 112–118, 2016.

[196] E. Ziermann and G. Ivens, "Final Report on the Power Operation of the AVR Experimental Nuclear Power Plant," Tech. Rep. JÜL-3448, Forschungszentrum Jülich, Jülich, Germany, 1997.

[197] K. Röllig, "The THTR-300 Coolant Gas Activity, an Indicator of Fuel Performance," Tech. Rep. No. IWGGCR-25, Hochtemperatur-Reaktorbau GmbH, Mannheim, Germany, 1991.

[198] H. Oehme and J. Schoening, “Design, Features, and Engineering Status of the THTR 300 MWe Prototype Power Station,” Tech. Rep. CONF-700401, Brown Boveri/Krupp Reaktorbau GmbH, Mannheim, Germany, 1970.